AMPHIPHILIC HYPERBRANCHED FLUOROPOLYMER NETWORKS AS PASSIVE AND ACTIVE ANTI-BIOFOULING COATINGS: FROM FUNDAMENTAL CHEMICAL DEVELOPMENT TO PERFORMANCE EVALUATION

A Dissertation

by

PHILIP MATTHEW IMBESI

Submitted to the Office of Graduate Studies of
Texas A&M University
in partial fulfillment of the requirements for the degree of

DOCTOR OF PHILOSOPHY

August 2012

Major Subject: Chemistry

Amphiphilic Hyperbranched Fluoropolymer Networks as Passive and Active Anti-biofouling Coatings: from Fundamental Chemical Development to Performance Evaluation

AMPHIPHILIC HYPERBRANCHED FLUOROPOLYMER NETWORKS AS PASSIVE AND ACTIVE ANTI-BIOFOULING COATINGS: FROM FUNDAMENTAL CHEMICAL DEVELOPMENT TO PERFORMANCE EVALUATION

A Dissertation

by

PHILIP MATTHEW IMBESI

Submitted to the Office of Graduate Studies of
Texas A&M University
in partial fulfillment of the requirements for the degree of

DOCTOR OF PHILOSOPHY

Approved by:

Chair of Committee,	Karen L. Wooley
Committee Members,	James D. Batteas
	Paul S. Cremer
	Melissa A. Grunlan
Head of Department,	David H. Russell

August 2012

Major Subject: Chemistry

ABSTRACT

Amphiphilic Hyperbranched Fluoropolymer Networks as Passive and Active Anti-biofouling Coatings: from Fundamental Chemical Development to Performance Evaluation. (August 2012)

Philip Matthew Imbesi, B.S., Case Western Reserve University;

B.A., Case Western Reserve University;

M.A., Washington University in St. Louis

Chair of Advisory Committee: Dr. Karen L. Wooley

The overall emphasis of this doctoral dissertation is on the design, synthesis, detailed characterization and application of amphiphilic hyperbranched fluoropolymers (HBFPs) crosslinked with poly(ethylene glycols) (PEGs) in complex polymer coatings as anti-biofouling surfaces. This dissertation bridges synthetic polymer chemistry, materials science and biology to produce functional coatings capable of fouling prevention, demonstrating thermo-controlled healing and acting as a benchmark surface to understand component:property relationships prior to increasing formulation complexities.

A two-dimensional array of HBFP-PEG coatings was produced by the co-deposition of uniquely composed HBFPs with varying weight percentages of PEG. Bulk and surface properties were evaluated and assigned to formulation trends. Based on

these findings, the most viable candidates were replicated and their fouling responses were assessed against three marine fouling organisms.

An active mode of biofouling resistance was covalently grafted onto the surface of HBFP-PEG. The presentation of the settlement-deterrent molecule noradrenaline (NA) works in tandem with the highly-complex surface, to act as a dual-mode, anti-biofouling coating NA-HBFP-PEG. Secondary ion mass spectrometry (SIMS) was employed to quantify the extent of NA substitution. Biological assays against oyster hemocytes confirmed the activity of the grafted NA and cyprid settlement assays supported that the overall anti-biofouling ability of NA-HBFP-PEG was increased by 75%.

Thermally-reversible crosslinks were installed as healable units throughout the framework of the networks, with the goal of generating coatings that could possess a greater resistance to mechanical failure. Small molecule and linear polymer models were probed by nuclear magnetic resonance (NMR) spectroscopy and gel permeation chromatography (GPC) to demonstrate the controlled reversibility of the crosslinks. Optical microscopy was employed to visualize surface scratch healing and fluorescence microscopy was used to identify the adsorption behavior of fluorescently-labeled proteins.

A benchmark, anti-biofouling surface was generated through thiol-ene crosslinking of a linear fluoropolymer with pendant alkenes (LFPene) with pentaerythritol *tetrakis*(3-mercaptopropionate) (PETMP). Core constituents were evaluated spectroscopically and surfaces of LFPene-PETMP, along with two model

surfaces that largely expressed a single component, were analyzed to understand how individual elements and blending contributed to the physical, mechanical and anti-biofouling properties to generate a performance baseline to compare against future generations.

DEDICATION

This work is dedicated to the three most important people in my life.

Thank you so much Mom, Dad and Jennifer for all of your love and support. I could not have done this without you.

ACKNOWLEDGEMENTS

This work would not have been possible without the mentorship of my advisor, Prof. Karen L. Wooley. I thank her for the masterful guidance, motivation and numerous insightful discussions, and never allowing me to be satisfied with "just enough". Throughout my career, I will carry the work ethic and standards that were instilled in me during my tenure as a graduate researcher in her lab.

I would like to thank my dissertation committee, Dr. James Batteas, Dr. Paul Cremer and Dr. Melissa Grunlan, for their comments, suggestions and challenges that helped drive me to make advances in my research. I would also like to thank the staff at Texas A&M for providing the facilities and business logistics that helped make conducting research and graduating possible, including: David H. Russell (Department Chair), Steve Silber, Vladimir Bakhmoutov and K. P. Sarathy (NMR Facility), Yohannes Rezenom and Vanessa Santiago (Laboratory for Biological Mass Spectrometry), Philip Wymola and Melvin Williams (Stockroom), Bill Merka (Glass Shop), Derek Pitts and Mike Green (IT and Computing), Sanding Manning (Graduate Advising) and everyone from the business office.

I had the unique opportunity to conduct a multi-disciplinary research project that spanned synthetic, analytical and physical chemistry, materials science and biology. I would like to acknowledge many collaborators outside of my laboratory that helped contribute to the vision and execution of this project: Andy Mount and Neeraj Gohad (Clemson U.), for our work on dual-mode anti-biofouling surfaces as well as a for great

friendship that spanned my entire graduate career. Nick Aldred and Tony Clare (Newcastle U.), John Finlay and Maureen and Jim Callow (U. Birmingham), for our work on the HBFP-PEG array as well as for the tireless testing of many coatings over the years. Mike Eller and Emile Schweikert (Texas A&M U.), for SIMS analysis that was included in two publications. Michael Mackay (U. Delaware), for allowing access to instrumentation that contributed to a publication. Dan Rittschof (Duke U.), for providing the brood stock for barnacles that were used in all of the collaborative bioassays.

I was privileged to work alongside many talented graduate students and post-doctoral associates that helped shape my skills and challenged me to advance my research: Jeremy Bartels, who was my graduate student mentor when I began in the lab and passed on immeasurable amounts of knowledge and enthusiasm to me as I continued the anti-biofouling coatings work. Chris Fidge (especially for starting the healable crosslinks investigations), Solenè Cauët and Jen Sorrels, three post docs that were great teachers and mentors and even better friends. Jeff Raymond, a great friend, a co-author on the benchmark coatings publication, and the "closer" on two additional manuscripts. Simcha Felder and Bryan Tucker, two extremely talented summer REU students that I had the pleasure of mentoring. Ang Lee, Lily Lin and Ritu Shrestha, members of my class when I joined the group and with whom I have worked for the past five years. Former Wooley Lab members, especially Brook Van Horn, Kenya Powell, Ke Zhang (who provided the lovely 3D images that appear throughout my publications, presentations and dissertation), Jun Ma, Rhiannon Iha, Celine Besset and Nam Lee, and all of the current Wooley Lab members, particularly Guorong Sun, Jiong Zou, Mahmoud

El Sabahy and Danielle Policarpio, for everything from answering a quick question to taking time out of the day for a bigger task, or maybe just for a casual chat, all of which helped make my day-to-day experience in this lab memorable. I would also like to specially thank our laboratory administrative assistant, Judy Taylor, for handling many of the logistical and business tasks that help this lab run smoothly.

My graduate career was unique in that I was lucky enough to study and research at two universities, as I moved with my advisor halfway through my tenure. The faculty, staff and students at Washington University in St. Louis supported me as I began my graduate career, and I thank all of them for two wonderful years, especially my former dissertation committee members Dr. Kevin Moeller, Dr. Josh Mauer and Dr. Don Elbert, and my friends Dr. Rich Loomis, Matt Strulson, Matt Hynes, Alison Redden, Jill Smith and Natalie Lafranzo.

I want to thank my incredible family for their continuing love and support. My parents, Maria and Phil, always put my education and well being before all else. I would not have been able to go on an academic tour that spanned Cleveland, St. Louis and College Station without their unwavering encouragement and sacrifices throughout my life. I want to thank my sisters Joanna and Michela, and my new brother-in-law Al, my grandparents, aunts, uncles and cousins for all of their love. I am very lucky to have a great family that has taught me good values and shaped me into the man that I am today.

Finally, thank you to my fiancée and future wife Jennifer Streff for going on this incredible journey with me in the past 21 months; I am excited for it to continue for the next 50+ years. We‟ve been on trips, visited families, worked alongside each other and

recently got engaged. You have kept me sane with unwavering love and a bottomless supply of homemade desserts while I was surrounded by my work. I cannot wait to continue our journey in Pennsylvania and see where life takes us next.

(individual funding acknowledgements are included at the end of each chapter)

NOMENCLATURE

AFM	Atomic Force Microscopy
ANOVA	Analysis of Variance
ASW	Artificial Seawater
ATR-FTIR	Attenuated Total Reflectance Fourier-Transform Infrared Spectroscopy
ATR-SCVCP	Atom Transfer Radical Self-Condensing Vinyl Copolymerization
BSA	Bovine Serum Albumin
cAMP	Cyclic Adenosine Monophosphate
CCD	Charge-Coupled Device
$CDCl_3$	Deuterated Chloroform
CuBr	Copper(I) Bromide
DA	Diels-Alder
DA-HBFP-PEG	Diels-Alder-Hyperbranched Fluoropolymer-Poly(ethylene glycol)
DA-PEG	Diamine-Terminated Poly(ethylene glycol)
DAPI	4',6-Diamidino-2-Phenylindole
DCC	Dicyclohexylcarbodiimide
DCM	Dichloromethane
DIPEA	Diisopropylethylamine
DLS	Dynamic Light Scattering
DMAP	4-Dimethylaminopyridine

DMF	Dimethylformamide
DSC	Differential Scanning Calorimetry
ET	Energy Transfer
FITC	5,6-Fluorescein Isothiocyanate
FSW	Filtered Seawater
GPC	Gel Permeation Chromatography
GPCR	G-Protein Coupled Receptor
GRK2	G-Protein Coupled Receptor Kinase-2
HBFP	Hyperbranched Fluoropolymer
HBFP-PEG	Hyperbranched Fluoropolymer-Poly(ethylene glycol)
HDA	Hetero-Diels-Alder
HPLC	High Pressure Liquid Chromatography
HRMS	High-Resolution Mass Spectrometry
IBMX	3-Isobutyl-1-Methylxanthine
IPA	Isopropyl Alcohol
IMO	International Maritime Organization
IR	Infrared
LFPene	Linear, Amphiphilic Fluoropolymer With Pendant Alkene Functionality
MeOH	Methanol
MOMCl	Methoxymethyl Chloride
MWCO	Molecular Weight Cutoff

NA	Noradrenaline
NA-HBFP-PEG	Noradrenaline-Hyperbranched Fluoropolymer-Poly(ethylene glycol)
NMR	Nuclear Magnetic Resonance
PBS	Phosphate Buffered Saline
PDMSe	Poly(dimethyl siloxane) Elastomer
PEG	Poly(ethylene glycol)
PETMP	Pentaerythritol Tetrakis(3-mercaptopropionate)
PDI	Polydispersity Index
PFS	Pentafluorostyrene
PHEMA	Poly(2-hydroxyethyl methacrylate)
PMAA	Poly(methacrylic acid)
PMDETA	N,N,N‟,N”,N”-Pentamethyldiethylenetriamine
RFU	Relative Fluorescence Units
RMS	Root Mean Squared
RPM	Revolutions Per Minute
SEC	Size Exclusion Chromatography
SIMS	Secondary Ion Mass Spectrometry
TBT	Tributyltin
TFS	Tetrafluorostyrene
TGA	Thermogravimetric Analysis
THF	Tetrahydrofuran

ToF	Time Of Flight
TrEG	Tri(ethylene glycol)
TRITC	Tetramethylrhodamine Isothiocyanate
UV	Ultraviolet
Vis	Visible
VOC	Volatile Organic Compound

TABLE OF CONTENTS

Page

LIST OF EQUATIONS

Page

LIST OF FIGURES

Page

LIST OF SCHEMES

Page

LIST OF TABLES

Page

CHAPTER I

INTRODUCTION

1.1 Background and Motivation

The United States Office of Naval Research (ONR) desires environmentally-benign ship hull coatings for their fleet to replace underperforming or soon-to-be banned formulations that are currently in use.[1] Unfortunately, marine biofouling had been controlled in the past by the use of anti-biofouling paints that relied on the release of toxic agents.[2] Action had been taken by the International Maritime Organization (IMO) to ban tributyltin (TBT) paints in 1998, effective 2008,[1-3] because of the irreversible accumulation of the leachates in the sediment resulting in unwanted environmental effects.[3] Accumulation of copper is occurring in seawater, at an estimated rate of 15×10^6 kg/yr world-wide. One example is that a single aircraft carrier can leach up to three pounds of copper per day.[4] Therefore, focus has been placed on replacing the current copper biocide formulations used by the US Navy because of the anticipation of legislation similar to that enacted for TBT-based paints.[5-7] While environmental concerns are a motivation for ONR, a stronger driving force for technical change is the desire to become more economically efficient. Fouling on ship hulls can result in up to 70% increased fuel consumption and added operational costs from cleaning and dry

---

This Dissertation follows the style of the *Journal of the American Chemical Society*.

docking.[4,8] Therefore, it is the ONR‟s goal to employ coatings that meet some of the following criteria: hull cleaning reduced to a 12 year cycle, fuel economy increased by at least 6% and speed loss of no more than 2%.[1]

Recent efforts toward the generation of non-toxic, anti-biofouling coatings have explored many different strategies for the prevention of biological settlement. Some of the chemistries evaluated are fluoropolymers,[9-14] PEGylated polymers,[15-17] zwitterionic polymers,[18] silicone elastomers,[19] xerogels,[20,21] quaternary ammonium salts[22] and even more complex fluoropolymer/PDMS/PEG ternary blends.[23,24] The surface and bulk properties of anti-fouling coatings, including the surface free energy, [25] surface modulus,[26] wettability,[27] and roughness,[27-29] impact the ability of marine organisms to detect a favorable surface on which to settle and make a strong anchorage to the substrate. It is anticipated that a combination of these surface characteristics, giving the polymer coating a high degree of complexity, are needed to combat the various mechanisms that are used by fouling organisms for settlement, adhesion and proliferation on substrates.

The Wooley laboratory has a long-standing interest in developing environmentally-benign materials that prevent fouling of marine organisms on ship hulls by generating surfaces with chemical and topographical complexity.[14] The hypothesis for this form of biofouling inhibition involves the design of a surface that presents these complexities on both microscopic and the nanoscopic scales. Because the surface features are on the size order as the whole organism (microscale) and its secreted adhesin proteins (nanoscale) there is not a significantly sized region appropriate for

strong adhesion. This surface complexity is achieved though the *in situ* covalent crosslinking of polymer materials while they undergo phase segregation and phase gradation. The polymer components in these systems consist of a low surface energy hyperbranched fluoropolymer (HBFP) and a water soluble poly(ethylene glycol) (PEG),[14] among other formulations.[30-32] When HBFP and PEG are deposited and crosslinked, kinetic trapping of the two physically-incompatible and chemically-reactive polymers gives rise to a network of HBFP-PEG that possesses the ability to inhibit the adhesion of microorganisms.

1.2 Evolution of Hyperbranched Fluoropolymers

Investigations of networks of the first generation of HBFP ($HBFP^{(I)}$) crosslinked with a diamine-termined PEG ($HBFP^{(I)}$-PEG) confirmed the hypothesis that nanoscopic surface complexities could resist protein adsorption and marine microorganism settlement and proliferation. The $HBFP^{(I)}$-PEG coating was obtained from reaction of linear PEG and $HBFP^{(I)}$ (Figure 1-1). $HBFP^{(I)}$ was synthesized from the polycondensation reaction of 3,5-*bis*[(pentafluorobenzyl)oxy]benzyl alcohol.[33] Although these materials demonstrated exceptional anti-biofouling properties,[34-36] they were synthesized from expensive reagents, under harsh conditions and required long reaction times. It was desired to advance the synthetic methodology used to afford the HBFP component while duplicating the anti-biofouling character and unique mechanical properties[37,38] of $HBFP^{(I)}$-PEG. As an aside, $HBFP^{(I)}$ will be revisited in this

dissertation, modified to bear thermally-reversible crosslinks as a healable component in the crosslinked network.

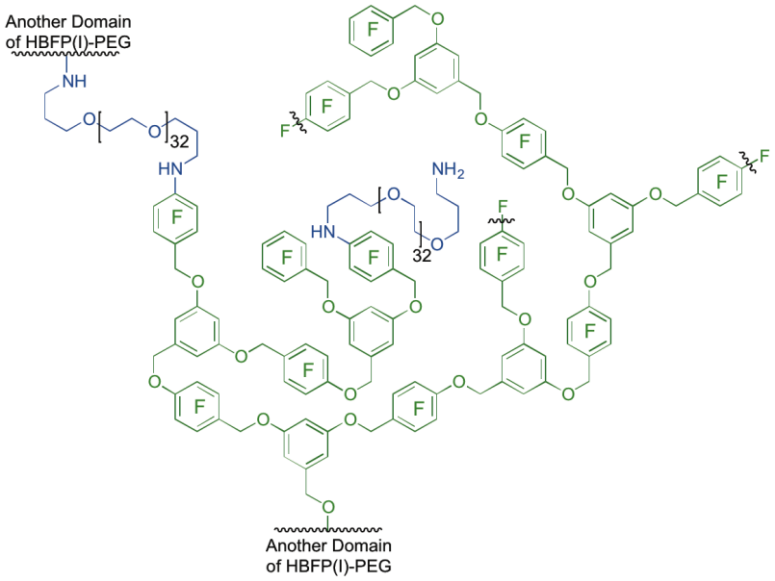

Figure 1-1. Graphical representation of amphiphilic HBFP$^{(I)}$-PEG crosslinked networks.

The second generation of HBFP (HBFP$^{(II)}$) was synthesized to address the shortcomings of HBFP$^{(I)}$ by improving the methodology for generating a low surface energy, crosslinkable component. Controlled radical polymerization, specifically atom transfer radical self-condensing vinyl copolymerization (ATR-SCVCP), was used to synthesize the HBFP by reacting two commercially-available reagents

pentafluorostyrene (PFS) and *para*-(chloromethyl)styrene.[39] Although HBFP$^{(II)}$ was prepared *via* a robust synthetic method, coatings of HBFP$^{(II)}$-PEG exhibited brittle behavior despite interesting surface topography and chemical heterogeneity (Figure 1-2).[40] An attempt was made to address these issues by incorporating a co-crosslinker in the formulation, the plasticizer Dytek® A. However, this method was unsuccessful. It is thought that HBFP$^{(II)}$ is too incompatible with PEG to allow for network integration to result in favorable mechanical properties. This led to the decision that improving the chemical structure of the HBFP, while still using ATR-SCVCP, should be the next course of action in attempts to generate more complex and mechanically-robust coatings.

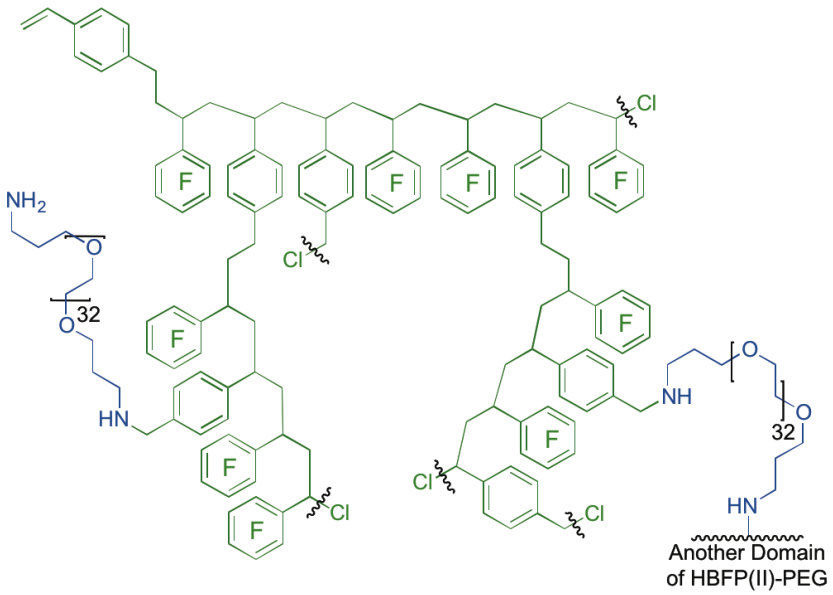

Figure 1-2. Graphical representation of amphiphilic HBFP$^{(II)}$-PEG crosslinked networks.

The third generation of HBFP ($HBFP^{(III)}$) built on $HBFP^{(II)}$ by installing hydrophilic linkages throughout the framework of the overall hydrophobic HBFP (Figure 1-3).[14] A tri(ethylene glycol) spacer was installed into the inimer (*ini*tiating mono*mer*) unit between the polymerizable fluorostyrene head group and the ATRP initiating tail. This was done improve miscibility between the incompatible HBFP and PEG (*versus* $HBFP^{(II)}$) and achieve an all-aqueous formulation deposited from water instead of organic solvent. *Implementation, reformulation and characterization of $HBFP^{(III)}$ and $HBFP^{(III)}$-based networks are to be the capstone of this body of work.* Specifically, $HBFP^{(III)}$ was investigated for the tunability of molecular and network properties by altering the molar ratio of comonomers in $HBFP^{(III)}$. ATR-SCVCP was used to synthesize an array of HBFPs by systematically varying the hydrophilic/hydrophobic balance of the afforded polymers. These polymers are then incorporated into a variety of networks and assessed to determine their surface character, bulk properties and anti-biofouling performance.

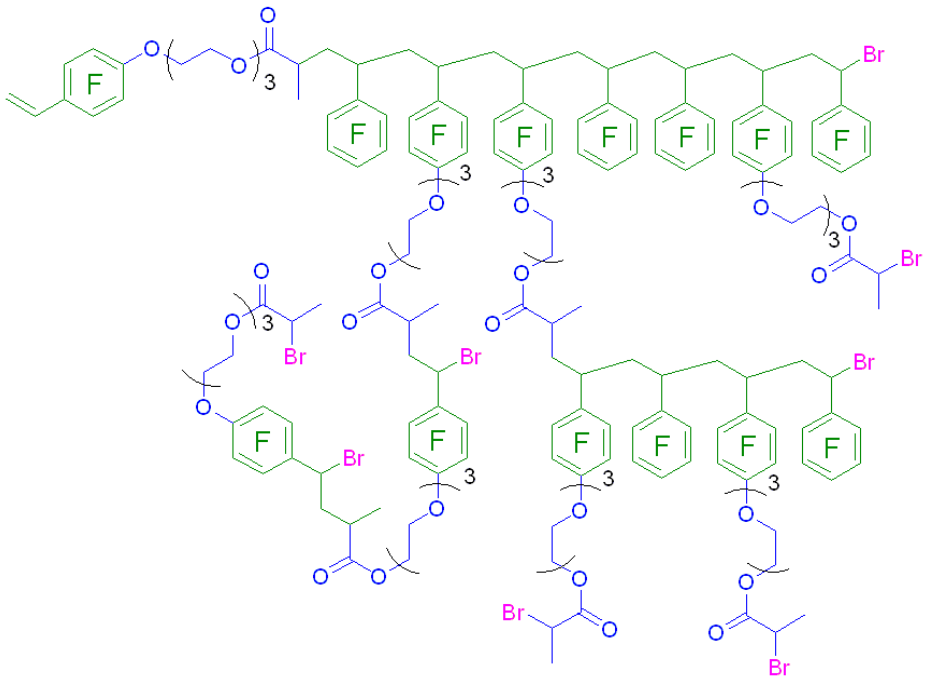

Figure 1-3. Graphical representation of amphiphilic HBFP$^{(III)}$.

The primary goals of the research in this body of work were:

1) to advance HBFP-PEG coatings and improve on previous anti-biofouling successes;

2) to explore surface modification strategies to introduce parallel modes of anti-biofouling action;

3) to install thermally-reversible crosslinks throughout the framework of the coatings to act as healable moieties;

4) to utilize rapid crosslinking methods, specifically incorporation of thiol-ene chemistry, as means to generate HBFP-PEG coatings more efficiently.

In **Chapter II**, a two-dimensional array of HBFP-PEG coatings was generated by crosslinking chemically-unique HBFP$^{(III)}$s (with varied comonomer feed ratios) and varying weight fractions of PEG. The HBFP component was synthesized by ATR-SCVCP to control the molecular weight distribution of the polymer as well as to establish functional chain ends that could be utilized later for crosslinking. The thermomechanical attributes of the networks were analyzed, showing a decrease in overall thermal stability with an increased PEG weight fraction. Trends in the Young‟s moduli of free-standing, water-swollen films revealed a mechanical property dependence on water uptake. Analysis revealed that networks with increased PEG weight content had greater water uptake, resulted in softening of the partially crystalline PEG-rich regions, and lower Young‟s moduli. Nanoscopic surface topography was determine by atomic force microscopy (AFM) on all of the surfaces studied. An interesting surface rearrangement process was discovered when comparing the static water contact angles of dry *versus* water-swollen coatings; the coatings that were swollen in water overnight exhibited surfaces with a higher water contact angle (*e.g.* greater surface hydrophobicity). Migration of HBFP$^{(III)}$ to the network surface after swelling and was confirmed by secondary ion mass spectrometry (SIMS), which detected a larger amount of fluorinated species in the water-swollen state. A series of coatings was replicated, and found to have variable performance against three marine fouling organisms. The HBFP-PEG surfaces almost entirely resisted the settlement of barnacle cyprids (*Balanus*

Amphitrite). Three times as many diatom cells (*Navicula Incerta*) were removed at a constant pressure when compared to a known fouling-release standard. However, green algae spores (*Ulva Linza*) easily colonized on the surface and were also difficult to remove, demonstrating how difficult it is to generate one surface that resists a large spectrum of marine life settlement.

In **Chapter III**, the overall anti-biofouling response of the HBFP$^{(III)}$-PEG surface was improved through the incorporation of an additional mode of settlement-prevention. Noradrenaline (NA), an active settlement-deterrent to barnacle cyprids, was grafted onto the surface of HBFP$^{(III)}$-PEG. This yielded a surface with highly-complex features that passively resisted settlement and was decorated with an active settlement deterrent that worked in tandem with each other. Confirming the covalent attachment of the NA moiety was a critical component of the study as physical entrapment of NA could lead to it eventually washing away. SIMS was employed to probe the relative increase in nitrogen-containing compounds as well as a decrease in functional sites after the grafting-onto reaction at the surface. Analysis of both results supported the covalent attachment of NA to HBFP$^{(III)}$-PEG. The activity of NA post-functionalization was confirmed by incubating oyster hemocytes (which undergo cellular apoptosis upon exposure to unbound NA) on the modified surfaces and imaging the effects NA had on the cells. This was achieved using both wide field fluorescence microscopy to determine degree of hemocyte settlement and higher resolution laser fluorescence confocal microscopy was used to determine the degree of hemocyte apoptosis. Barnacle cyprid

settlement assays, comparing unmodified and NA-modified HBFP$^{(III)}$-PEG surfaces revealed a lower percentage of organisms interacting with the modified surfaces.

In **Chapter IV**, focus was shifted from the optimization of the anti-biofouling properties towards installing healable units in the coating. A Diels-Alder pair was installed onto the chain ends of HBFP$^{(I)}$ and PEG as a thermally-reversible crosslinking unit. HBFP$^{(I)}$ was chosen for these studies as this work focuses on the crosslinking chemistry. At the time this study began, HBFP$^{(I)}$-PEG was the best performing surface and therefore was selected. To understand how the crosslinks would behave in the solid-state, solution-state model reactions on small molecule and linear polymer analogs were studied to evaluate the reaction conditions necessary to control reformation of broken crosslinks. Coatings were cast from solutions containing the Diels-Alder modified HBFP$^{(I)}$ and PEG (DA-HBFP-PEG) and studied for their surface properties in both the dry and water-swollen state. The surface was found to behave similarly to the covalent counterpart (HBFP$^{(I)}$-PEG), which suggested that changing the crosslinking chemistry may not drastically alter the desired anti-biofouling performance. To confirm the fouling deterrence, the surfaces were incubated with a PBS solution containing fluorescently-labeled bovine serum albumin (BSA). Fluorescence microscopy was used to capture images of the DA-HBFP-PEG surface before and after incubation and was run in parallel to the HBFP$^{(I)}$-PEG counterpart. It was found that both surfaces had a low degree of BSA adsorption, confirming the anti-biofouling ability of DA-HBFP-PEG. Lastly, the surfaces were subjected to light abrasions and deep cuts to determine the ability to repair itself upon heating. It was determined that light abrasions could be

efficiently repaired in *ca.* 30 min. However, deeper cuts only partially healed, even after 3 h, due to the lack of bulk flow of the material into the cavities.

In **Chapter V**, investigations into a rapid, UV-promoted thiol-ene crosslinking reaction was conducted. This was done in order to advance this class of amphiphilic coating as a material that can be efficiently produced with high mechanical integrity while still possessing the anti-biofouling abilities of the previous generations of HBFP-PEG. This study was also critical to generating a standard baseline of properties and performance, as well as define a set of metrics, that will be used in the evaluation of future generations of coatings. Additionally, the fluoropolymer synthesized was a linear analogue of HBFP$^{(III)}$. The intent was to establish a benchmark material of the simplest variety, prior to the introduction of complexities. 2D stead state fluorescence spectroscopy was employed on serial dilutions of the core constituents to understand their interaction properties in the solution state and extrapolate relative fluorescence intensities in the solid state. In turn, this provided a metric for observing the networks *via* fluorescence microscopy to determine the composition of network microstructure. This finding was then used in conjunction with protein adsorption assays to understand which microstructures foul more readily. Understanding the microscale chemical features will drive future formulations to target blend ratio that inhibit fouling. Three coatings were cast; one mixing a linear fluoropolymer with pendant alkenes (LFPene) with a crosslinker pentaerythritol *tetrakis*(3-mercaptopropionate) (PETMP), one crosslinking LFPene with hexane dithiol and one crosslinking PETMP with 1,5-hexadiene. The three coatings were compared to determine the effects the individual

core constituents and mixing of the core constituents have on bulk and surface properties. The LFPene-PETMP coating was found to resist protein adsorption more efficiently than either of the test surfaces obtained from a single component, despite the fact it did not have the lowest surface energy. AFM revealed a complex surface topography in the LFPene-PETMP, as well as surface modulus of approximately 0.5 GPa with over 50 times the variance in modulus when compared to the two test films. Interestingly, differential scanning calorimetry (DSC) experiments revealed a greater enthalpy of heating during the first heating curve from 50 to 150 °C. This is attributed to the vulcanization of unreacted thiols in the bulk, and was not observed on the subsequent heating cycles. Further evidence of disulfide bond formation was observed as an increase in thermal stability during thermogravimetric analysis (TGA) experiments where materials with residual thiol groups were found to have higher onset temperatures of thermal degradation. A post-cure bake is proposed to react unused thiols to increase the overall mechanical strength and potentially decrease the propensity for proteins to bind at thiol functionalities expressed on the surface.

CHAPTER II

TARGETED SURFACE NANOCOMPLEXITY: TWO-DIMENSIONAL CONTROL OVER THE COMPOSITION, PHYSICAL PROPERTIES AND ANTI-BIOFOULING PERFORMANCE OF HYPERBRANCHED FLUOROPOLYMER – POLY(ETHYLENE GLYCOL) AMPHIPHILIC CROSSLINKED NETWORKS*

2.1 Original Publication Information

This chapter was originally submitted on May 7, 2012 as an article in *Polymer Chemistry*, an invited contribution to the **Themed Issue on Supramolecular and Dynamic Covalent Polymers**.

Collaborative contributions: J. Finlay, M. Callow and J. Callow conducted biological assays on diatom cells and green algae spores and sporelings; N. Aldred and A. Clare conducted biological assays on barnacle cyprids; M. Eller and E. Schweikert performed SIMS; S. Felder helped synthesize monomers, polymers and coatings; K. Pollack and A Lonnecker assisted with mechanical property measurements on equipment provided by the laboratory of M. Mackay; J. Raymond assisted in thermal

---

*Reprinted with permission from "Targeted Surface Nanocomplexity: Two-dimensional control over the composition, physical properties and anti-biofouling performance of hyperbranched fluoropolymer – poly(ethylene glycol) amphiphilic crosslinked networks", by Philip M. Imbesi, John A. Finlay, Nick Aldred, Michael J. Eller, Simcha E. Felder, Kevin A. Pollack, Alexander T. Lonnecker, Jeffery E. Raymond, Michael E. Mackay, Emile A. Schweikert, Anthony S. Clare, James A. Callow, Maureen E. Callow and Karen L. Wooley, **2012**, *Polymer Chemistry*, Advance Article DOI: 10.1039/C2PY20317K, Copyright 2012 by The Royal Society of Chemistry. http://pubs.rsc.org/en/content/articlelanding/2012/py/c2py20317k

experiment analyses.

Modifications to the original document are cosmetic and used only to conform the format of this document or provide uniformity of enumeration.

2.2 Overview

A two-dimensional array of amphiphilic crosslinked networks was prepared by systematic alteration of both the composition of hyperbranched fluoropolymers (HBFPs) and the relative stoichiometries upon crosslinking with poly(ethylene glycol) (PEG). Results of physicochemical, mechanical, surface and biofouling assessment are described in full. The materials were designed to present complex surface topographies, morphologies, and chemical features over nano- and microscopic dimensions to explicitly inhibit microorganism settlement and adhesion. A multi-dimensional, tunable matrix was generated to understand and optimize the composition-structure-property relationships. The thermal properties of the crosslinked networks were analyzed by thermogravimetric analysis (TGA) and differential scanning calorimetry (DSC), where the onset of thermal degradation, overall thermal stability and phase transition temperatures could be controlled based on the formulation. Investigation of the mechanical properties of the coatings in the water-swollen state found that the Young‟s modulus, ranging between 10.0 and 121 MPa, was dependent on both the wt% of PEG crosslinker and chemical composition of the HBFP. This result, on average, gives Young‟s moduli an order of magnitude larger than that previously reported for HBFP-

PEG networks. Use of atomic force microscopy (AFM) provided insight into the nanoscale topography of the networks. Interestingly, it was observed that for all networks, surface roughness increased with water swelling going from an average of 115 ± 49 nm (dry) to 214 ± 106 nm (swelled) RMS roughness. Probing the surface chemistry by optical tensiometry revealed an increase in the static water contact angle by as much as 40° after water swelling. These two findings display a counter-intuitive increase of the surface hydrophobicity. Secondary ion mass spectrometry (SIMS) confirmed migration of hydrophobic fluorocarbon units to the surface by quantifying a 24% increase in fluorine species ejected from a dry *versus* water-swollen surface. Selected formulations of HBFP-PEG that demonstrated complex surface features and an overall high mechanical strength were tested in biological assays and all surfaces (3 formulations × 12 replicates) completely resisted the settlement of barnacle cyprids (*Balanus amphitrite*). Diatoms (*Navicula incerta*) were two- to three-times more easily removed from the HBFP-PEG surfaces compared to a homogeneous polydimethylsiloxane elastomer (PDMSe) standard surface. In contrast, algal spores (*Ulva linza*) were able to colonize the surfaces and were more difficult to remove in comparison to the PDMSe standard, pointing to the challenges associated with the development of a single material that is capable of broad anti-biofouling performance.

2.3 Introduction

Our laboratory has spent considerable effort investigating non-toxic anti-biofouling systems for the explicit purpose of generating surfaces that are highly complex in a static state and also capable of dynamic reorganization, as multi-approach mechanism to establish broad-based anti-fouling performance. Globally, efforts towards the commercial implementation of an environmentally-benign ship hull coating have progressively increased since the International Maritime Organization (IMO) ban of tributyltin (TBT) paints in 2008.[1,2] Associated costs may accrue an annual fouling penalty of $22-44 million, both from having to clean 12 million sq. ft. of surfaces and from a 10% increase in fuel consumption due largely to drag.[2,4] The majority of ship hull treatments utilize biocide formulations,[7] where the biocide of choice is predominantly a copper oxide. However, recent investigations into the environmental effects of copper-based paints have yielded negative evidence reminiscent of TBT.[6] A single aircraft carrier leaches three pounds of copper per day,[4] and this irreversible accumulation of metal-based particulates in the marine sediment is harmful to marine life.[2] An anticipated consequence is a worldwide ban, for both recreational and industrial sea craft, of copper oxide marine paints in coming decades.[6] One approach to achieve a pristine surface is through a fouling-release mechanism.[41] However, coatings that function solely through the principle of fouling release are generally less effective in protecting slow moving or static immersion equipment because the materials do not prevent settlement of fouling organisms and fouling release typically does not occur

until speeds of around 15 knots.[10,23,24,42,43] As our interests are in the development of novel, non-toxic anti-biofouling coatings, we chose to avoid an approach that requires the use of biocidal agents as well as one that only relies on a fouling-release mechanism and instead designed a highly-complex polymer surface that passively resists the settlement of biological organisms and can be easily cleaned.

Direct prevention of marine organism settlement is achieved by presenting nanoscopically-complex topographical, morphological and chemical features, where it was hypothesized that a variation in surface chemistry,[13] energy,[25] modulus,[26] and roughness[27-29] would influence the ability of organisms to sense, settle and attach to a surface. A commercial transition is in progress from biocidal or ablative coatings towards benign paints that are comprised of low surface energy polymer components, *e.g.*, silicones (Intersleek®700, SeaGuard®, *etc.*) and/or fluoropolymers (Intersleek®900, *etc.*).[44] Recent examples in the literature have also investigated the combinations of fluoropolymers and PEGs, into amphiphilic materials, with promising results.[13,24,45-47]

Recent investigations by our laboratory have been conducted in the design of materials that utilize supramolecular assembly for their production and exhibit dynamic reorganization as a potential contributor to their anti-biofouling characteristics. Specifically, we have focused on highly complex coatings composed of hyperbranched fluoropolymers crosslinked with poly(ethylene glycol) (HBFP-PEG),[14] with special attention given to the synthetic methodologies for the HBFP component, as well as variations in composition and, in turn, the physical properties. Formulating coatings

with HBFP and PEG has demonstrated unique anti-fouling properties,[35,36] and uncommon mechanical behavior.[37,38] The HBFP-PEG mode of action for biofouling prevention is believed to be derived from a combination of complex surface topographies, morphologies, compositional variation over nano- and microscopic dimensions, and the ability to dynamically reorder on water submersion. In selecting the appropriate chemistry to synthesize the HBFP component, several iterations of HBFP have been evaluated.[14] The first HBFP-PEG coating[34] was from the reaction of linear PEG and a HBFP synthesized from a polycondensation reaction that required expensive reagents, harsh conditions and long reaction times.[33] The experimental conditions were later improved to afford an HBFP from atom transfer radical self-condensing vinyl copolymerization (ATR-SCVCP) of commercially-available starting materials.[39] Although the HBFP component was prepared *via* a robust synthetic method, coatings obtained from this second generation of HBFP exhibited brittle behavior.[40] In order to improve the mechanical properties while incorporating amphiphilicity within the HBFP framework, which was expected to interface well with a PEG crosslinker, a third-generation HBFP-PEG was designed.[14] This material was later advanced into a dual-mode, passive and active, anti-biofouling coating.[48] However, further tuning of the HBFP-PEG anti-biofouling system to optimize the physical and anti-biofouling properties was desired.

In this study, a two-dimensional array of HBFP-PEG coating compositions was evaluated for trends in the thermal, mechanical, surface and anti-biofouling properties, with compositional variations in the HBFP structure and PEG crosslinker weight

fractions. These highly-complex coatings were produced from the third generation of HBFP, containing hydrophilic ethylene glycol units distributed throughout the hydrophobic framework,[14] crosslinked with a *bis*-amino functionalized PEG. Following deposition of solutions containing different stoichiometries of HBFP and PEG onto substrates, the solvent was evaporated to effect phase segregation while performing kinetic trapping of intermediate phase-segregated morphologies by covalent crosslinking, affording coatings that have nanoscopically-resolved complex surface topographies and chemical heterogeneities. Thermal properties were studied by differential scanning calorimetry (DSC) and thermogravimetric analysis (TGA) to elucidate the effects of composition on phase transitions, PEG reordering, and thermal stability. Elongation tensile testing on free-standing, water-swollen films revealed Young‟s moduli were dependent on water uptake. Surface properties were probed by atomic force microscopy (AFM) and static water contact angle. A counter-intuitive effect was observed for the surface upon swelling in water due to a dynamic reorganization event between the surface and bulk polymer components, confirmed *via* secondary ion mass spectrometry (SIMS).[49-52] Understanding the unique bulk and surface properties of each coating allowed for selection of the best overall series of HBFP-PEG coating formulations for replication and comprehensive anti-biofouling/fouling-release studies against barnacle cyprids, diatoms and algal spores and sporelings (young plants).

2.4 Experimental

2.4.1 Materials

Reagents were purchased from Sigma Aldrich and used as received unless otherwise noted. 2,3,4,5,6-Pentafluorostyrene (PFS) was purchased from Apollo Scientific (UK) and filtered through a plug of neutral alumina prior to use. Adult barnacle (*Balanus amphitrite*) brood-stock was supplied by D. Rittschof, Duke University Marine Laboratory, North Carolina, U. S. A. Nexterion clean room glass and T2 Silastic (PDMSe) were supplied by A. B. Brennan, University of Florida, U. S. A.

2.4.2 Characterization

Monomers and polymers were characterized by ^{1}H, ^{13}C and ^{19}F nuclear magnetic resonance (NMR) spectroscopies using a Varian Inova 300 MHz spectrometer. ^{1}H and ^{13}C NMR spectra were analyzed using the solvent signal as an internal reference and ^{19}F NMR spectra were analyzed with CF_3COOH as an external standard. IR spectra were obtained on a Shimadzu IR Prestige attenuated total reflectance Fourier-transform infrared spectrometer (ATR-FTIR). Spectra were analyzed using IRsolution software package (Shimadzu). High-resolution mass spectrometry (HRMS) was conducted on an Applied Biosystems PE SCIEX QSTAR. Gel permeation chromatography was performed on a Waters Chromatography, Inc. (Milford, MA), 1515 isocratic HPLC

pump equipped with an inline degasser, a model PD2020 dual-angle (15° and 90°) light scattering detector (Precision Detectors, Inc.), a model 2414 differential refractometer (Waters, Inc.), and four PL_{gel} polystyrene-*co*-divinylbenzene gel columns (Polymer Laboratories, Inc.) connected in series: 5 μm Guard (50 × 7.5 mm), 5 μm Mixed C (300 × 7.5 mm), 5 μm 10^4 (300 × 7.5 mm), and 5 μm 500 Å (300 × 7.5 mm) using the Breeze (version 3.30, Waters, Inc.) software. The instrument was operated at 35 °C with THF as the eluent (flow rate set to 1.00 mL/min). Polymer solutions were prepared at a known concentration (*ca*. 3 mg/mL) and an injection volume of 200 μL was used. Data collection was performed with Precision Acquire 32 Acquisition program (Precision Detectors, Inc.) and analyses were carried out using Discovery32 software (Precision Detectors, Inc.) with a system calibration curve generated from plotting molecular weight as a function of retention time for a series of broad polydispersity poly(styrene) standards. Differential scanning calorimetric (DSC) studies were performed on a Mettler-Toledo DSC822^e (Mettler-Toledo, Inc., Columbus, OH), with a heating rate of 10 ºC/min. The T_g was taken as the midpoint of the inflection tangent, upon the third heating scan. Thermogravimetric analysis was performed under Ar atmosphere using a Mettler-Toledo model TGA/DSC 1 Star^e system, with a heating rate of 10 ºC/min. Measurements were analyzed using Mettler-Toledo Star software version 10.00c. Atomic force microscopy was performed under ambient conditions in air. The AFM instrumentation consisted of a MFP-3D-BIO AFM (Asylum Research; Santa Barbara, CA) and standard silicon tips (type, OTESPA-70; L, 160 μm; normal spring constant, 50 N/m; resonance frequency, 246-282 kHz). Contact angles were measured as static

contact angles using the sessile drop technique[53] with an Attension Theta optical tensiometer (Biolin Scientific). Drops were fitted with a Young-Laplace formula to calculate the static contact angle in the Theta software (Biolin Scientific). Secondary ion mass spectrometry was conducted on a custom built instrument equipped with a custom built C_{60} source capable of producing C_{60}^{+2} at 43keV total impact energy.[54-57] The instrument is equipped with a 1 m linear time of flight (ToF) and an electron emission microscope. All samples were analyzed in negative ion mode using the emitted electrons as the start for the ToF measurement. Tensile tests were performed on the HBFP-PEG series based upon a method adapted from ASTM D882-95a and conducted using a Rheometrics Solids Analyzer, RSA III (TA Instruments, New Castle, DE).

2.4.3 Synthesis

4-[Oxy(tri(ethylene glycol))]-2,3,5,6-tetrafluorostyrene (1). To a stirring solution of sodium hydride (60 wt% dispersion in mineral oil, 4.95 g, 124 mmol) in THF (400 mL) in a 1 L two-neck round-bottomed flask suspended in an ice bath, was added tri(ethylene glycol) (TrEG) (41.3 mL, 309 mmol), followed by the addition of PFS (14.2 mL, 20.0 g, 103 mmol). The solution was allowed to warm to room temperature with stirring under N_2 for 14 h. The reaction mixture was then concentrated *in vacuo*, dissolved in deionized water (300 mL) and extracted with ethyl acetate (4 x 300 mL). The organic fractions were combined, dried over anhydrous $MgSO_4$, filtered and concentrated *in vacuo* to afford a clear, pale yellow oil. Further purification by silica gel

flash chromatography using 10% MeOH in CH_2Cl_2 as the eluent afforded **1** as a clear, colorless oil in 62% yield (20.6 g). T_{decomp}: 362 °C, 74% mass loss @ 500 °C. ^{1}H NMR (acetone-d_6, ppm): δ 6.60 (dd, *J* = 12 Hz and 18 Hz, 1H, H_2C=C***H***-R), 5.96 (d, *J* = 18 Hz, 1H, ***H***(H)C=CH-R (*trans*)), 5.65 (d, *J* = 12 Hz, 1H, H(***H***)C=CH-R (*cis*)), 4.38 (t, *J* = 5 Hz, 2H, TFS-O-C***H***$_2$-CH_2-OR), 3.78 (t, *J* = 5 Hz, 2H, TFS-O-CH_2-C***H***$_2$-OR‟) and 3.40-3.70 (m, 8H, R-O-(C***H***$_2$-C***H***$_2$-O-C***H***$_2$-C***H***$_2$-OH). ^{13}C NMR (acetone-d_6, ppm): δ 147.2, 143.7, 143.0, 140.2, 137.3, 122.5, 122.4, 122.3, 122.2, 111.0, 74.8, 73.2, 71.1, 70.8, 70.5 and 61.6. ^{19}F NMR (acetone-d_6, ppm): δ -147 (m, 2F, *ortho*-***F*** to -CH=CH_2) and -159 (m, *meta*-***F*** to -CH=CH_2). IR (ν, cm^{-1}): 3600-3200, 3050-2800, 1643, 1489, 1358, 1288, 1250, 1080 and 941. HRMS m/z calculated for $C_{14}H_{16}F_4O_4$ $[M + H]^+$ 325.10 Da, found 325.1063 Da.

4-[Oxy(tri(ethylene glycol))bromoisopropionyl]-2,3,5,6-tetrafluorostyrene (2). To a stirring solution of triethylamine (7.70 mL, 55.5 mmol) in THF (250 mL) in a 500 mL two-neck round bottom flask was added **1** (5.00 g, 15.4 mmol). The solution was cooled to 0 °C and 2-bromoisopropionyl bromide (3.99 g, 18.5 mmol) was added dropwise. The solution was allowed to warm to room temperature with stirring under N_2 for 16 h. The reaction mixture was filtered, the filtrate was then concentrated *in vacuo*, dissolved in dichloromethane (500 mL) and was then washed with deionized water (4 x 500 mL). The organic fraction was dried over anhydrous $MgSO_4$, filtered and concentrated *in vacuo* to afford a clear, pale yellow oil. Further purification by silica gel flash chromatography using 30% ethyl acetate in hexanes as the eluent afforded **2** as a clear, colorless oil in 82% yield (5.81 g) which was stored at 4 °C. T_{decomp}: 297 °C, 70%

mass loss @ 500 °C. ^{1}H NMR (acetone-d_6, ppm): δ 6.60 (dd, *J* = 12 Hz and 18 Hz, 1H, H_2C=C***H***-R), 5.96 (d, *J* = 18 Hz, 1H, ***H***(H)C=CH-R (*trans*)), 5.65 (d, *J* = 12 Hz, 1H, H(***H***)C=CH-R (*cis*)), 4.6 (q, *J* = 5 Hz, 1H, R-C(***H***)(Br)CH_3), 4.5 (t, *J* = 5 Hz, 2H, TFS-O-C***H***$_2$-CH_2-OR), 4.3 (t, *J* = 5 Hz, 2H, R-CH_2-C***H***$_2$-O(O)C-R‟‟), 3.9 (t, *J* = 5 Hz, 2H, TFS-O-CH_2-C***H***$_2$-OR), 3.8-3.6 (m, 6H, R-O-C***H***$_2$-C***H***$_2$-O-C***H***$_2$-CH_2-O(O)C-R‟‟), 1.8 (d, *J* = 5 Hz, 3H, R-C(H)(Br)C***H***$_3$) ppm. ^{13}C NMR ($CDCl_3$, ppm): δ 171.3, 145.7, 144.0, 141.8, 140.2, 136.4, 122.0, 121.8, 110.6, 74.1, 70.6, 70.1, 64.9, 55.6 and 30.5 ppm. ^{19}F NMR (Acetone-d_6, ppm): δ -147 (m, *ortho*-***F*** to -C=CH_2), -159 (m, *meta*-***F*** to -C=CH_2) ppm. IR (ν, cm^{-1}): 3050-2800, 2874, 2747, 1738, 1647, 1485, 1451, 1429, 1406, 1377, 1354, 1335, 1223, 1153, 1119, 1078, 1030, 968, 937, 858, 762, 677 and 648. HRMS m/z calculated for $C_{17}H_{19}BrF_4O_5$ $[M + H]^+$ 459.04 Da, found 459.0439 Da.

Hyperbranched Fluoropolymer (HBFP, w/50 mol% PFS) (3). To a dry 100 mL round bottom Schlenk flask equipped with a stir bar was added **2** (4.01 g, 8.72 mmol, 1 equiv.), PFS (1.69 g, 8.71 mmol, 1 equiv.), PMDETA (3.08 g, 17.8 mmol, 2 equiv. /Br), CuBr (1.25 g, 8.73 mmol, 1 equiv. /Br) and anisole (40 mL). The solution was deoxygenated *via* freeze-pump-thaw (x3), the vessel was backfilled with N_2 and then lowered into an oil bath set at 65 °C and the reaction was allowed to proceed for 20 h. The polymerization was quenched by opening the flask to air and submerging the flask in liquid nitrogen. Once thawed, the contents were dissolved in dichloromethane (450 mL), eluted through a plug of alumina to remove the catalyst, concentrated *in vacuo*, and the product was isolated by precipitation into cold hexanes (3 x 1.2 L) to afford a white powder of **3** in 55% yield (3.14 g). M_w^{GPC} = 11800 Da, M_n^{GPC} = 7000 Da,

M_w/M_n = 1.69. T_g = 53 °C. T_{decomp}: 244 °C, 78% mass loss @ 600 °C. ^{1}H NMR ($CDCl_3$, ppm): 4.6-4.0 (br, m, TFS-O-C***H***$_2$-CH_2-OR and R-CH_2-C***H***$_2$-O(O)C-R‟), 4.0-3.4 (br, m, R-O-C***H***$_2$-C***H***$_2$-OR‟), 3.1-1.5 (3 br m, C***H***$_2$-C***H***(R)- backbone), *δ* 1.5-0.7 (br, m, C-C***H***$_3$) ppm. ^{13}C-NMR ($CDCl_3$, ppm): δ 176.6, 144.7, 140.7, 137.6, 122.2, 114.7, 74.3, 70.8-70.0, 68.8, 63.6, 41.7-32.1, 30.7-29.7, 24.7 ppm. ^{19}F NMR ($CDCl_3$, ppm): δ -143 (br, m, *ortho-**F*** (PFS) and *ortho-**F*** (TFS)), -157 (br, m, *para-**F*** (PFS) and *meta-**F*** (TFS)), -162 (br, m, *meta-**F*** (PFS)) ppm. IR (ν, cm^{-1}): 2950-2850, 2361, 1744, 1651, 1540-1410, 1296, 956, 864 and 760.

Hyperbranched Fluoropolymer (HBFP, w/67 mol% PFS) (4). A procedure similar to **3** was followed using **2** (4.01 g, 8.72 mmol, 1 equiv.), PFS (3.40 g, 17.5 mmol, 2 equiv.), PMDETA (3.10 g, 17.9 mmol, 2 equiv. /Br), CuBr (1.27 g, 8.85 mmol, 1 equiv. /Br) and anisole (40 mL) to afford a white powder of **4** in 48% yield (3.57 g). M_w^{GPC} = 16700 Da, M_n^{GPC} = 9500 Da, M_w/M_n = 1.76. T_g = 67 °C. T_{decomp}: 248 °C, 81% mass loss @ 600 °C. ^{1}H NMR ($CDCl_3$, ppm): 4.6-4.0 (br, m, TFS-O-C***H***$_2$-CH_2-OR and R-CH_2-C***H***$_2$-O(O)C-R‟), 4.0-3.4 (br, m, R-O-C***H***$_2$-C***H***$_2$-OR‟), 3.1-1.5 (br, m, C***H***$_2$-C***H***(R)- backbone), *δ* 1.5-0.7 (br m, C-C***H***$_3$) ppm. ^{13}C-NMR ($CDCl_3$, ppm): δ 176.6, 144.7, 140.7, 137.6, 122.2, 114.7, 74.3, 70.8-70.0, 68.8, 63.6, 41.7-32.1, 30.7-29.7, 24.7 ppm. ^{19}F NMR ($CDCl_3$, ppm): δ -143 (br, m, *ortho-**F*** (PFS) and *ortho-**F*** (TFS)), -157 (br, m, *para-**F*** (PFS) and *meta-**F*** (TFS)), -162 (br, m, *meta-**F*** (PFS)) ppm. IR (ν, cm^{-1}): 2950-2850, 2361, 1744, 1651, 1540-1410, 1296, 956, 864 and 760.

Hyperbranched Fluoropolymer (HBFP, w/75 mol% PFS) (5). A procedure similar to **3** was followed using **2** (5.00 g, 10.9 mmol, 1 equiv.), PFS (6.34 g, 32.7 mmol,

3 equiv.), PMDETA (3.33 g, 19.2 mmol, 2 equiv./Br), CuBr (1.57 g, 10.9 mmol, 1 equiv./Br) and anisole (100 mL) to afford a white powder of **5** in 62% yield (7.03 g). M_w^{GPC} = 17400 Da, M_n^{GPC} = 8600 Da, M_w/M_n = 1.72. T_g = 73 °C. T_{decomp}: 310 °C, 85% mass loss @ 500 °C. ^{1}H NMR ($CDCl_3$, ppm): 4.6-4.0 (br, m, TFS-O-C***H***$_2$-CH_2-OR and R-CH_2-C***H***$_2$-O(O)C-R‟), 4.0-3.4 (br, m, R-O-C***H***$_2$-C***H***$_2$-OR‟), 3.1-1.5 (br, m, C***H***$_2$-C***H***(R)- backbone), δ 1.5-0.7 (br m, C-C***H***$_3$) ppm. ^{13}C-NMR ($CDCl_3$, ppm): δ 176.6, 144.7, 140.7, 137.6, 122.2, 114.7, 74.3, 70.8-70.0, 68.8, 63.6, 41.7-32.1, 30.7-29.7, 24.7 ppm. ^{19}F NMR ($CDCl_3$, ppm): δ -143 (br, m, *ortho-**F*** (PFS) and *ortho-**F*** (TFS)), -157 (br, m, *para-**F*** (PFS) and *meta-**F*** (TFS)), -162 (br, m, *meta-**F*** (PFS)) ppm. IR (ν, cm^{-1}): 2950-2850, 2361, 1744, 1651, 1540-1410, 1296, 956, 864 and 760.

Design of The Hyperbranched Fluoropolymer – Polyethylene Glycol Crosslinked Network (HBFP-PEG) Two-dimensional Array. An array of HBFP-PEG networks was prepared with unique chemical compositions of HBFP (**3**, **4** or **5**) and at increasing wt% PEG (33 wt%, **a**, 50 wt%, **b**, or 60 wt%, **c**, calculated as w/w% of the total mass) to afford the series of crosslinked networks **6a-c**, **7a-c**, **8a-c**, respectively, with detailed studies conducted to understand how the polymer composition and extent of crosslinking affected the physicochemical, thermal, mechanical and anti-biofouling properties.

General Procedure for the Preparation of HBFP-PEG Crosslinked Networks. To a scintillation vial was added 700 mg of a selected HBFP (**3**, **4**, or **5**), 350 mg, 700 mg or 1050 mg of 1500 Da DA-PEG (33, 50 or 60 wt%, respectively), THF (8 mL), and diisopropylethylamine (DIPEA) (100 μL), and the mixture was vortexed until

homogeneous. The solution was drop cast (1 mL per slide) onto pre-cleaned glass microscope slides. A period of *ca*. 30 min allowed for the solvent to evaporate and afford a thick pre-gel that was cured at 110 °C for 45 min under N_2 atmosphere, followed by submersion in a water bath overnight to leach any residual organic compounds and also release the free-standing films from the substrate. Samples for mechanical testing were deposited onto precut (1 cm x 2 cm) glass slides. Coatings used in biological assays were reaffixed to the glass substrates using a silicone adhesive (DAP household adhesive sealant, 100% silicone) by spreading a thin layer of silicone on the glass and uniformly pressing the partially dried, released film onto the glass slide.

2.4.4 Barnacle Cyprid Settlement and Removal

Culture of cyprids: Adult barnacles were allowed to spawn naturally in the laboratory and approximately 10,000 stage 1 nauplii were collected over a period of 2 to 3 h. The nauplii were attracted to a cold light source, according to the protocol of Elbourne *et al.*[58] and transferred at intervals to a dilute solution of the alga *Tetraselmis suicica* for temporary storage. When sufficient numbers of nauplii had been collected, all nauplii were transferred to a clean plastic bucket containing 10 L of 0.7 μm-filtered seawater with 36.5 mgL^{-1} streptomycin sulphate and 21.9 mgL^{-1} penicillin G sodium salt. The larvae were fed excess *Tetraselmis suecica* for 5 d until metamorphosis to the cyprid stage. Cyprids were then filtered from the culture, transferred to 0.22 μm

nitrocellulose-filtered natural seawater (FSW) and used for settlement tests after 3 or 5 d of storage at 6 ºC.

Settlement assays: Settlement assays were of the drop-type previously employed.[59] 1 mL of FSW was deposited onto each microscope slide sample (twelve replicates per formulation), into which 20 cyprids were added. The first experiment used 3-day-old cyprids and the subsequent experiment used 5-day-old cyprids; the latter chosen for their increased propensity to settle. Assays were incubated at 28 ºC, in the dark, for up to 72 h and observed for settlement every 24 h. On the occasion of each settlement assay, a laboratory standard assay was performed to determine the viability of the larvae. 10 cyprids per 2 mL were added to each of 12 wells of a 24-well polystyrene Iwaki (Iwaki corp., Japan) microplate, and settlement was observed after 24 h. In all cases, settlement of cyprids was as expected in this standard assay (between 20-30% after 24 h), giving confidence in the experimental data.

Removal assays: For removal assays, approximately 100 day-5 cyprids were introduced into the same 1 mL drop on each sample surface in a 1 x 10^{-5} M solution of 3-isobutyl-1-methylxanthine (IBMX) following Clare *et al.*[60] IBMX is an artificial settlement inducer for cyprids that has been shown to almost double the rate of settlement of these organisms in static water assays. The water-jetting method used for removal of newly metamorphosed barnacles is described in detail elsewhere,[59] but briefly involved application of a raster-scanned jet of water, calibrated to 62 kPa impact pressure, across an array of 12 coated microscope slides. Numbers of organisms

attached before and after jetting were enumerated and only those removed „cleanly" were counted in the analysis.

2.4.5 Diatom Settlement and Removal

Leaching: Coatings (6 replicates per test surface) were equilibrated in de-ionized water for 48 h. Following this, all coatings were immersed in filtered (0.22 μm) artificial seawater (ASW) for 2 h before the start of the experiment.

Initial attachment (density of cells attached after gentle washing): Detailed methods are described elsewhere.[20] In brief, cells of *Navicula incerta* were cultured in F/2 medium contained in 250 mL conical flasks. Log phase cells were washed 3 times in fresh medium and diluted to give a suspension with a chlorophyll *a* content of approximately 0.25 μg mL^{-1}. Cells (10 mL) were pipetted into individual compartments of Quadriperm dishes each containing a test slide. After 2 h on the laboratory benchtop (ca. 20 °C), the slides were exposed to a submerged wash in ASW to remove cells that had not attached. Three replicate samples were fixed in 2.5% glutaraldehyde, washed and air-dried. Due to surface roughness and autofluorescence, the density of cells attached to the surface was counted on each slide by eye from a computer screen attached to a fluorescence microscope. Counts were made for 10 fields of view on each slide.

Strength of attachment: Three other replicate slides with attached cells of *N. incerta* were exposed to a shear stress of 52 Pa in a water channel. Samples were fixed

and the number of cells remaining attached was counted as described above. Percentage removal was calculated from the cell counts before and after exposure to shear stress.

2.4.6 Settlement of Spores and Removal of Sporelings of Ulva linza

Leaching: Coatings were prepared as described for *N. incerta*.

Settlement of spores: Zoospores were obtained from mature plants of *Ulva linza* and a suspension was prepared for the assay as described previously.[61,62] In brief, 10 mL of a suspension of zoospores (1.0×10^6 mL^{-1}) were added to individual compartments (6 replicates per test surface) of Quadriperm dishes each containing a test slide. After 45 min in the dark at ca. 20 °C, the slides were washed in ASW to remove unsettled, *i. e.* swimming zoospores.

Growth and attachment strength of sporelings: The slides with attached spores were cultured in enriched seawater medium[63] for 7 d to the stage of sporelings (young plants). Sporeling biomass was determined *in situ* by measuring the fluorescence of the chlorophyll contained within the cells in a fluorescence plate reader (Tecan Genios). The biomass was quantified in terms of relative fluorescence units (RFU) using 70 point fluorescence readings. A water jet was used to measure strength of attachment of the sporelings.[64] One of each of the six replicate slides was subjected to a single impact pressure by the water jet. A series of water pressures was used and the proportion of biomass in the area exposed to the water jet was remeasured. Percentage

removal at each impact pressure was calculated from the before and after mean RFU values.

2.5 Results and Discussion

2.5.1 HBFP Polymer Synthesis and HBFP-PEG Crosslinked Networks

A series of HBFPs was synthesized with unique chemical compositions, varying in the amount of branching and ethylene glycol units, in order to tune the properties of the polymers. The particular HBFPs used in this study, **3-5**, were of a unique chemical composition and structure,[14] by linking hydrophobic and hydrophilic characteristics on a molecular level throughout the hyperbranched polymer framework. The amphiphilic framework was designed with the intention to both increase the overall complexity of the core constituents, but also to bear short hydrophilic groups that would interface with the PEG crosslinker. The HBFPs were synthesized *via* ATR-SCVCP to control the molecular weight of the polymer and yield reactive chain ends to be later utilized to establish a series of crosslinked networks (Scheme 2-1). The preparation of **3-5**, therefore, began from the nucleophilic aromatic substitution of the *para*-fluorine of PFS with an excess of tri(ethylene glycol) (TrEG) to prevent against *bis*-arylation and yield **1**. Esterification of **1** with 2-bromoisopropionyl bromide gave the amphiphilic initiating monomer (inimer) **2**. Copolymerization of **2** in the presence of one, two or three molar equivalents of PFS yielded HBFP comprised of either 50, 67 or 75 mol% PFS, **3-5**,

respectively. Polymerizations were monitored by ^{1}H-NMR spectroscopy and size exclusion chromatography (SEC) to determine when to quench the reactions and afford polymers having weight-average molecular weights of approximately 12-18 kDa. It was determined by ^{19}F NMR that the molar repeat unit ratios of PFS and **2** that comprised **3-5** were within 5% of the mol fraction of comomomer unit feed ratios that were employed. Therefore, for the purposes of this study, **3-5** will be referred to by their feed ratio values. Through this method, a linear series of polymers was generated that had the same general topology but was unique in the amount of branches, number of functional chain ends and fluorine content.

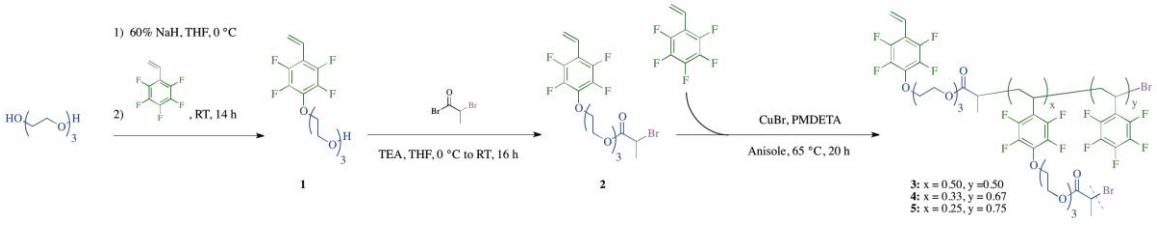

Scheme 2-1. Synthesis of HBFPs **3-5** by ATR-SCVCP.

A matrix approach was employed to prepare a series of crosslinked networks that possessed unique formulations, varying in both the structure of the HBFP and the relative stoichiometry of PEG, to understand the effects of each component on the network bulk and surface properties. The synthetic approach to establish the crosslinked

networks exploited the reactive bromoacetyl and bromobenzyl functionalities at the chain ends of the HBFP, originally used to propagate the growing polymer chains, to undergo reaction with diamine-terminated PEG (DA-PEG). A 3 × 3 array of nine samples was prepared by crosslinking **3**, **4** or **5** with 33, 50 or 60 wt% of DA-PEG affording the two-dimensional library of **6a-c**, **7a-c**, and **8a-c** (Scheme 2-2). These nanoscopically-complex materials were created through the co-deposition and curing of incompatible HBFP and PEG components, where the HBFP and PEG underwent supramolecular assembly processes to segregate into their respective domains through the differences in topology and energy, with coincident covalent crosslinking to kinetically trap non-thermodynamically stable nano- and microscopic morphologies that later exhibited dynamic reorganization events. To obtain a coating, a solution of HBFP and PEG in THF was cast onto glass microscope slides and a *ca*. 30-min period was allowed for excess solvent to evaporate leaving a thickened, optically transparent pre-gel. The coated slides were then cured at 110 °C for 45 min in N_2 atmosphere, which yielded a polymer coating 50-100 μm thick. These coatings were subjected to a complete set of rigorous analyses to determine which formulation(s) were optimum for selection to scale up and biological assays.

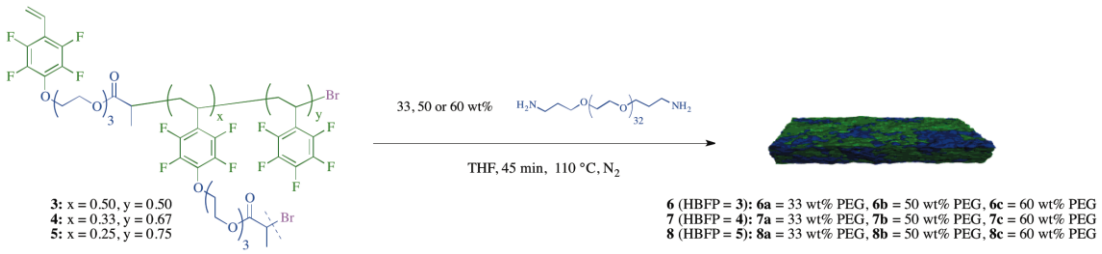

Scheme 2-2. Crosslinking strategy for the preparation of HBFP-PEG coatings at varying HBFP compositions and PEG concentrations.

2.5.2 Thermal Studies

The thermal transition temperatures and thermal stabilities of the polymer networks were obtained by differential scanning calorimetry (DSC) and thermogravimetric analysis (TGA). On the first heating pass, shoulders were observed on either side of a clear melting transition for **7a-c**. The network **7a** appeared to have lower homogeneity, with two crystallization temperatures upon cooling, than the **7b** and **7c** coatings, each of which exhibited a single transition. Additionally, the second phase transition for **7a** occurred below 0 °C, which was assigned to a PEG hydrate resulting from small amounts of water being present (Figure 2-1). For **6a**, there was an extremely large enthalpy energy cost in transitioning from 50 to 100 °C during the initial temperature ramp. This suggests that before heating, PEG was interacting in a non-energy minimized fashion with severe steric constraints, which is likely due to inclusion

of water or solvent molecules and supports that lower PEG loading leads to lower homogeneity of the PEG-rich domains, as observed in **7a**. Also, no T_m transitions were observed for **6a-c**, likely due to the lack of large PEG-rich regions capable of forming microcrystallites. Lastly, for **8a-c**, there was again a high initial energy cost when heating from 50 to 100 °C. After initial reordering, the systems returned to a single glass transition, at temperatures similar to those observed for **6a-c.** The DSC data imply PEG incorporation dictates the size and character of PEG-rich microdomains. This reveals a desired control; the ratio of PFS:inimer in HBFP can be tuned to a "sweet-spot" where domains are largely HBFP-free allowing for true crystalline character to be expressed or, alternately, compositions where this did not occur can be sought. The onset temperature of thermal degradation as well as the overall thermal stability was dependent on formulation parameters. One slight trend observed was that an increase in weight fraction of crosslinker resulted in a higher onset temperature of degradation. A more pronounced trend could be found in the overall mass loss (at 500 °C), which directly correlated to the amount of PEG present in the sample. All nine samples displayed thermal degradation response with the same general profile (Figure 2-1). A complete summary of the thermal properties for the crosslinked networks can be found in Table 2-1.

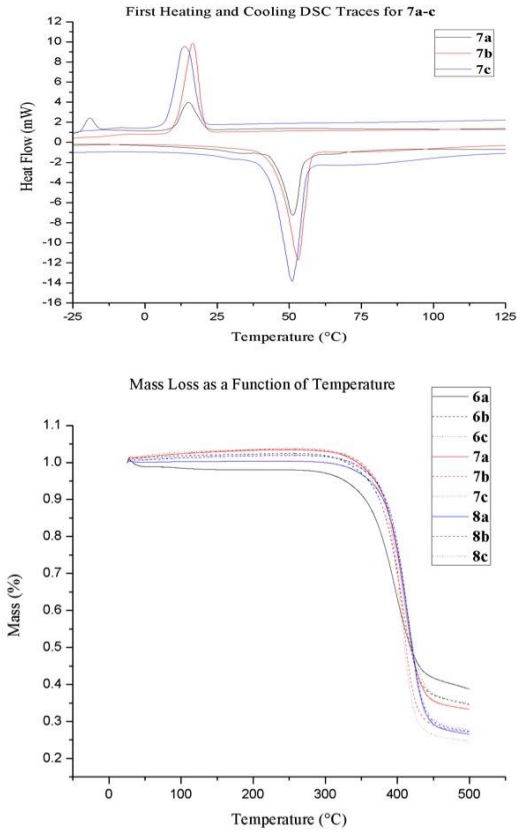

Figure 2-1. DSC curves for **7a-c** (top) and mass loss as a function of temperature for the HBFP-PEG array of coatings **6a-c**, **7a-c** and **8a-c (**bottom**)**.

Table 2-1. Summary of the thermal transitions of the HBFP-PEG array of coatings **6a-c**, **7a-c** and **8a-c**.

Network	**$T_{d,\ onset}$ (°C)**	**Mass Loss 250 °C to 500 °C (%)**	**T_c (°C)**	**T_m (°C)**	**T_g (°C)**
6a	356	59.3	-		32
6b	372	67.9	-		33
6c	378	69.0	-		33
7a	376	70.1	15, -19	47	33
7b	373	76.5	16	54	34
7c	380	77.5	13	47	33
8a	377	73.8			33
8b	382	74.6			32
8c	382	80.2			31

2.5.3 Mechanical Strength

Elongation tensile testing was used to determine the mechanical properties of the HBFP-PEG free-standing films and how water uptake affected the bulk moduli. Experiments were conducted at 22 °C, a Hencky strain of 0.01 s^{-1} and with an initial grip separation of ~5 mm. For each sample, at least five water-swollen specimens (approximate dimensions: 10 mm x 20 mm x 0.3 mm) were tested. The tensile modulus (*E*, MPa) was calculated as the slope of the initial linear (Hookean) portion of the stress-strain curves, and the ultimate tensile strength (ζ_{UTS}, MPa) and strain to failure (ε_f, %) were also recorded. A two-dimensional bar graph of Young‟s modulus, *E*, as a function of PEG wt% and HBFP chemical composition, revealed a two-dimensional influence on modulus (Figure 2-2). When varying PEG, maxima were found for films afforded from 33 wt% PEG (**6a**, **7a**, **8a**), relative to films with higher weight percent of PEG crosslinker. The decrease in Young‟s modulus observed with an increase in crosslinker wt%, regardless of HBFP composition, was likely a result of additional PEG allowing more water uptake into the bulk of the film resulting in a weaker network. For HBFP, local maxima were found for films obtained from **4** (**7a**, **7b**, **7c**) relative to films obtained from **3** and **5** at equal wt% PEG. The local maxima are likely a result of the combination of two mechanically-beneficial trends. HBFPs with higher mol% inimer in the polymer backbone resulted in more branching and chain end functionality that allowed for higher extents of crosslinking. However, less inimer in the HBFP framework resulted in a more hydrophobic polymer and films likely sequestered less

water. These results are complementary to the DSC findings for **7a-c**, which revealed the existence of microcrystalline PEG-rich regions, lending additional mechanical strength to the network. A summary of measured moduli values, ultimate tensile strengths and percent elongations has been compiled (Table 2-2).

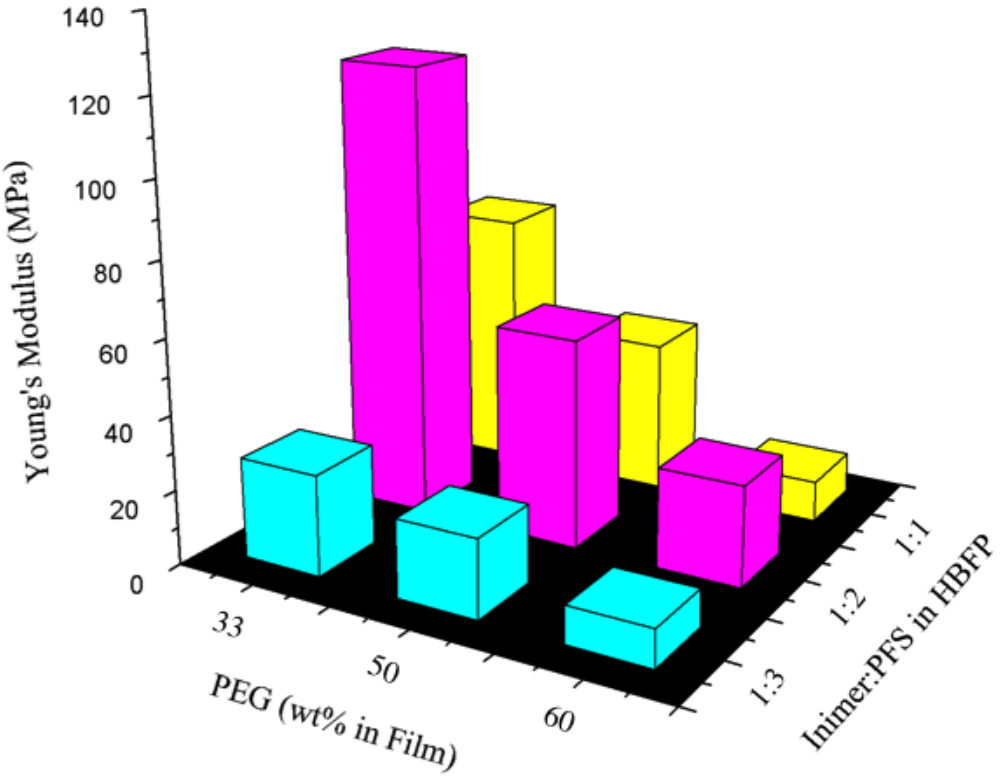

Figure 2-2. Young‟s modulus for a 3 × 3 array of HBFP PEG films based on the amount of crosslinker in the film (X axis) and the feed ratio of inimer:PFS in the HBFP (Y axis).

Table 2-2. Summary of the bulk mechanical properties of the HBFP-PEG array of coatings **6a-c**, **7a-c** and **8a-c**.

Network	Ultimate Tensile Strength (MPa)	Failure Strain (%)	Young's Modulus (MPa)
6a	12.9 ± 3.0	10 ± 4	70 ± 32
6b	18.9 ± 6.3	16 ± 5	41 ± 22
6c	6.9 ± 3.0	42 ± 20	11 ± 8
7a	41.7 ± 16.9	11 ± 2	121 ± 57
7b	18.7 ± 2.5	22 ± 8	56 ± 12
7c	6.0 ± 1.3	16 ± 5	27 ± 6
8a	15.4 ± 9.2	28 ± 11	27 ± 15
8b	10.9 ± 3.9	36 ± 19	21 ± 14
8c	7.5 ± 3.0	23 ± 16	10 ± 7

2.5.4 Surface Chemistry: Atomic force microscopy

Investigation of the surface contour *via* atomic force microscopy (AFM) allowed for the visualization and quantification of surface roughness to determine formulations that presented a complicated terrain that may inhibit bioadhesion. Some general trends were obtained from the images collected from the series of HBFP-PEG surfaces (Figure 2-3). Sub-micron topographical features were distributed across the surfaces of all formulations, with an average RMS roughness of 115 ± 49 nm for films in the dry state. Across all formulations in the dry state, the features were smoother at 33 wt% PEG compared to the formulations with higher wt% PEG. The films were swollen in water and re-examined to probe the dynamic reorganization of the surface features. The average RMS roughness increased to 214 ± 106 nm for the water-swollen samples. Prior to the introduction of water, features generally observed were hills, and after swelling in water, cavities appeared, which is consistent with results from previous generations of HBFP-PEG.[34,40] Qualitatively, it appeared that the amount and complexity of features increased with increased weight fraction of crosslinker, both in the dry and water swollen state. This increase in surface complexity was attributed to a larger percentage of PEG component needing to be surface energy-stabilized by the HBFP to which it was tethered. The complex, nanoscopic topography may present topographical obstacles for settling microorganisms, but the random distribution of chemical features across topographical features is also important, and investigations of the surface chemistry were needed.

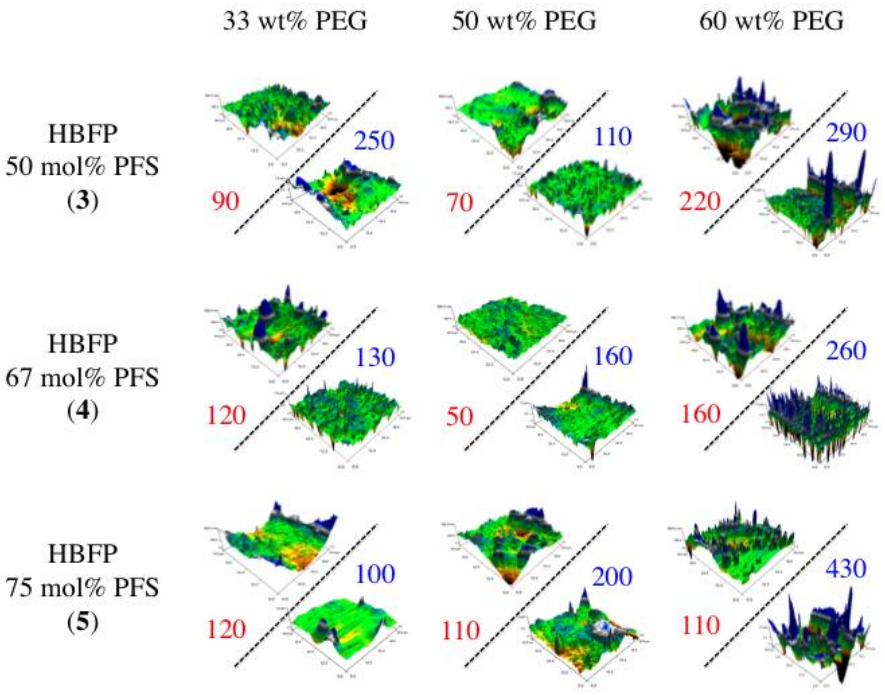

Figure 2-3. Atomic force microscopy images for the HBFP-PEG array in both the dry (upper left of division) and water-swollen (lower right of division) states. Scan size is $50 \times 50\ \mu m^2$, z axis is 600 nm (dry) and 1000 nm (water swollen) and the RMS roughness (nm, ±15%) is given in red for the dry state and blue for the water-swollen state.

2.5.5 Surface Chemistry: Contact angle

Coatings of **7a-c** were subjected to additional analysis, to observe static water contact angle before and after water swelling. This selection was made due to **7a-c** possessing the highest overall moduli, making them best suited to be replicated for investigation of fouling response. In both the dry and water swollen states, the contact angle decreased as the amount of PEG crosslinker increased in the formulations, indicating an increase in surface hydrophilicity. However, at any amount of PEG, the transition from the dry to the water-swollen state resulted in an increase in static water contact angle, which was an indication of an increasingly hydrophobic surface (Figure 2-4). Wynne observed this "contraphilic" behavior in polyurethane block copolymers with a semi-fluorinated polyether block, and determined hydrogen bonding with water was the driving force for this surface chemical composition change.[65,66] We believed that a similar interaction was occurring between the PEG and water molecules, where a dynamic reorganization process between neighboring PEG domains aggregated and sequestered water and forced the more hydrophobic HBFP to the surface. However, the AFM and contact angle measurements were incapable of quantifying the relative amount of HBFP and PEG on the surface before and after water swelling.

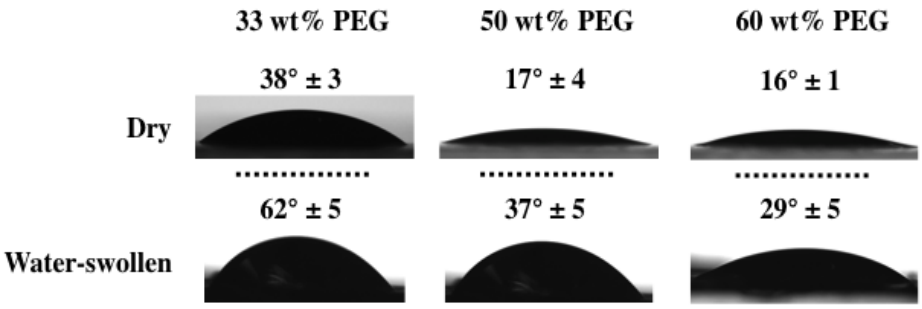

Figure 2-4. Static water contact angles of coatings from an HBFP with 67 mol% PFS, **4**, crosslinked with 33 (**7a**), 50 (**7b**) and 60 (**7c**) wt% PEG in the dry and water-swollen states.

2.5.6 Surface Chemistry: Secondary ion mass spectrometry

Event-by-event cluster SIMS was performed on a sample of **8a** to probe the effective fluorine coverage in both the dry and water-swollen states to determine if a chemical reorganization event was occurring. Four 200 μm radius regions were randomly chosen and each region was impacted by approximately 5×10^5 individual projectiles. All were averaged to ensure sample consistency both in the dry and water-swollen states (Figure 2-5). The static water contact angle in each state was also recorded. A quantitative estimate of fluorine surface coverage was calculated,[67] following equations 2-1 and 2-2, where it was determined in the dry state that fluorine coverage was 69.4% ± 1.8%, and corresponded to a static water contact angle of 34°.

After soaking the coating in water the fluorine coverage increased to 93.7% ± 1.8%, and the water contact angle increased as well to 74°. The increase in effective fluorine coverage by 24% supported the hypothesis that the fluoropolymer backbone migrated to the surface during the bulk inclusion of water.

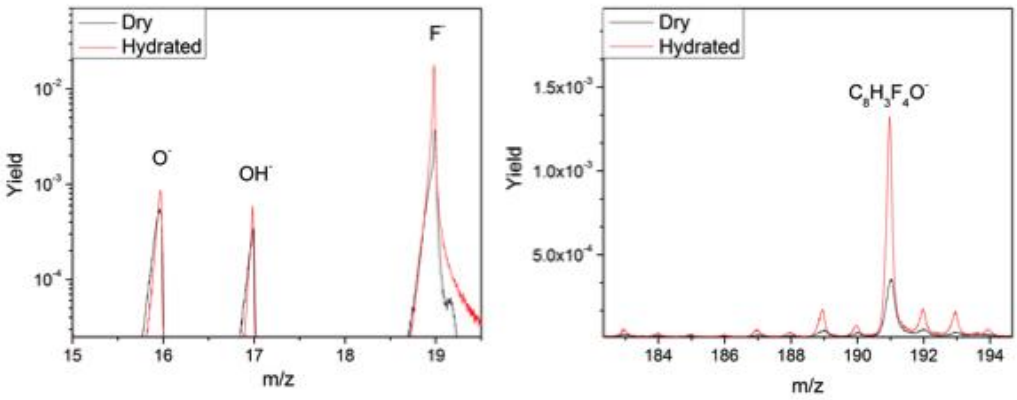

Figure 2-5. Dry (black) and hydrated (red) overlaid spectra for m/z ranges 15-19 (left) and 183-194 (right) for **8a** before and after submersion in water for 24 h.

$$N_E = \frac{Area_{Coincidental\ Emission}}{Area_F \times Area_{PFS}}$$

Equation 2-1. Calculation for the effective number of impacts.

$$Coverage = \frac{N_E}{N_O}$$

Equation 2-2. Calculation for the quantitative estimate for surface coverage.

2.5.7 Barnacle Cyprid Settlement and Removal

It was hypothesized that these surfaces would inhibit the settlement of marine organisms, so samples of **8a** were replicated first to investigate the surface‟s ability to inhibit settlement of barnacle cyprids (*B. amphitrite*).[19] In the first settlement assay using only replicates of **8a**, no cyprids settled over the course of 72 h. This assay was repeated using a second batch of larvae (again, 3 d old) and one cyprid settled, which was subsequently dislodged during observation of the assay, compared to the expected level of settlement on the laboratory standard surface. These data suggested that the HBFP-PEG surfaces possessed the ability to deter fouling. We chose to conduct a larger investigation that studied a range of coatings that were considered to be the best candidates from physical testing. Given that **7a-c** possessed the highest overall Young‟s modulus, complex topographical features and interesting wetting behavior, we believed these coatings were the best candidates for biological assays, and replicates for **7a**, **7b** and **7c** were studied for their settlement inhibition and ease of removal of cyprids. A third settlement experiment was conducted using the three sample types, **7a-c**, and carried out using 5-day-old cyprids but, again, settlement was negligible after 72 h, with

fewer than 10 cyprids settling across all surfaces (36 slides in total); numbers that are too low for interpretation. To all intents and purposes, therefore, surfaces **7a-c** effectively resisted settlement.

To determine the ease of removal of adhered barnacle cyprids to **7a-c**, experiments were attempted on three separate occasions. In the first experiment (potentially using the samples from the third settlement assay described above), settlement was insufficient to allow for testing. A second attempt employed the use of IBMX, a chemical settlement inducer, and yielded the bare minimum barnacle cyprid attachment required to achieve significant removal data. There appeared to be a trend of increased ease of removal with increasing wt% PEG (Figure 2-6). Validation of this observation required a third trial to be set up, using the same surfaces, except in this trial, many cyprids were observed unattached, but in varying states of metamorphosis by day 7 implying that they may have attached, initiated metamorphosis, but subsequently become detached during the process. Even after 7 d, insufficient numbers of settled cyprids were obtainable and the removal experiments could not proceed. The combination of high larval density with a chemical settlement inducer usually ensures at least 50% settlement after 24 h, providing sufficient individuals for removal assays on most surfaces. However, using this method, the maximum settlement achieved was around 2% (75 settled individuals across all surfaces), prohibiting removal experiments on all but one occasion. These assays support the conclusion that the materials tested were highly resistant to barnacle fouling and suggested a mechanism of action involving interference with cyprid adhesion to the surfaces.

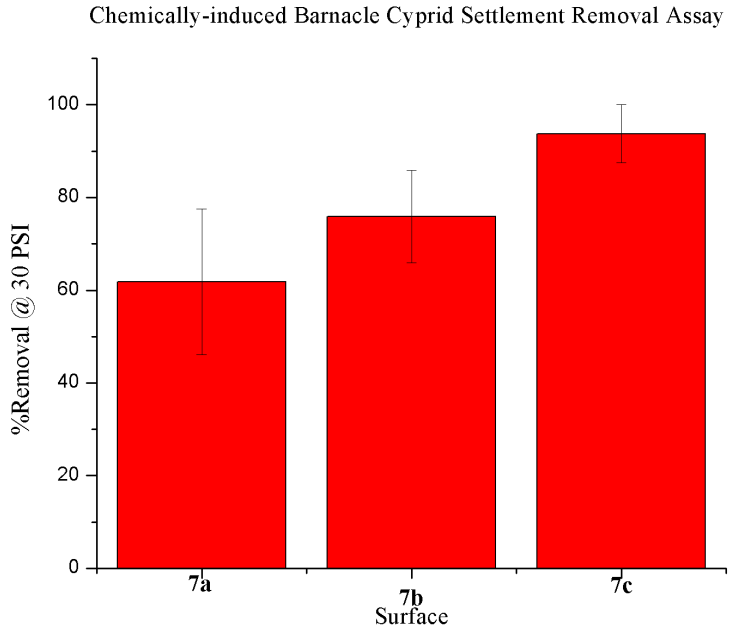

Figure 2-6. The percentage removal from HBFP-PEG coatings **7a-c** of barnacle cyprids induced to settle using IBMX.

2.5.8 Settlement and Removal of N. incerta

Additional studies on replicates of **7a-c** were conducted on an organism whose settlement behavior is not heavily dependent on the macroscopic topography, so the diatom *N. incerta* was chosen. Diatoms sink in the water column and reach the surface by gravity so each surface received the same density of diatoms landing on it. The gentle washing process removed unattached and weakly attached cells, so any differences in attachment density correlate with the ability of cells to attach firmly to the

surfaces. The initial attachment density of diatoms was lower on **7b** and **7c** than on **7a** and the PDMSe standard (one-way analysis of variance $F_{4,145}$ =5.4 P<0.05 supported by post hoc Tukey test) (Figure 2-7, left). Exposure to a shear stress of 52 Pa removed a significantly greater proportion of diatoms from **7a-c** than from the PDMSe standard (one-way analysis of variance and Tukey test; $F_{4,145}$ =12.5 P<0.05) (Figure 2-7, right). Adhesion strength of cells to the HBFP-PEG coatings was similar to the glass standard (diatoms adhere weakly to hydrophilic surfaces including glass). Samples **7a-c** displayed promising fouling-release potential with respect to the PDMSe standard and further studies with diatoms are warranted. Diatom adhesion strength generally shows a close correlation with surface energy being greater on hydrophobic surfaces[20] and the relatively high wettability of the test surfaces probably contributed to their fouling-release properties.

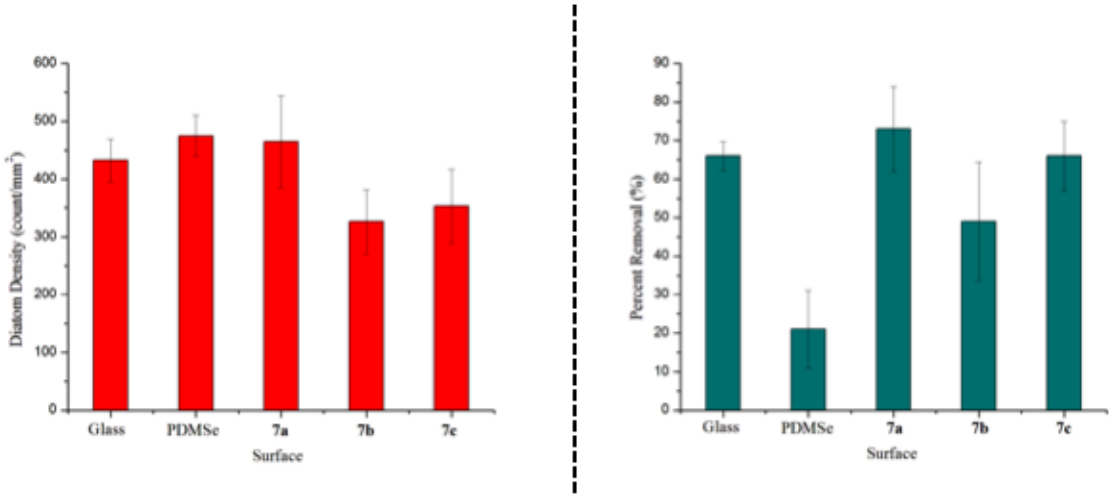

Figure 2-7. Settlement density (left) and percentage removal after exposure to a shear stress of 52 Pa (right) of cells of the diatom *N. incerta* from HBFP-PEG coatings. Each point is the mean from 30 counts (10 counts on each of 3 replicate slides). Bars show 95% confidence limits derived from arcsine-transformed data. PDMSe is Silastic T2.

2.5.9 Adhesion Strength of Sporelings of Ulva linza

The encouraging results that showed inhibition of settlement of barnacle cyprids as well as the ease of cell removal from the diatom assays led to the replication of samples of **7a-7c** and **8a** to study the fouling-release performance against sporelings (young plants) of the green macroalga *Ulva linza*. It was not possible to obtain accurate quantification of the number of spores that settled because the surface roughness and a

high degree of autofluorescence made accurate counting impossible. However, there was a similar density of spores settled across **7a-c** and **8a** to those on the glass and PDMSe standards, although spore settlement was patchy and strongly influenced by the macroscopic unevenness of the coating, which was a result of the free-released thin films being reattached to the substrate with an adhesive layer. A green lawn of sporelings developed on all of the coatings reflecting that broadly similar numbers of spores had settled. Sporeling strength of attachment on the HBFP-PEG series varied between coatings. Sporeling strength of attachment to **8a** was low and similar to that on the PDMSe standard, which was included in the assay because of its well-established fouling-release properties. Sporeling strength of attachment to **7a** varied between samples producing an erratic pressure-removal curve, which was attributed to the surface roughness imparted by the reattachment of the coatings to the glass substrate. Coatings of **7b** and **7c**, which had higher amounts of wt% PEG crosslinker, exhibited relatively strong strength of attachment of sporelings. These data suggest that **8a** had the best overall fouling-release profile. In the **7a-c** series, the best fouling-release profile was demonstrated by the coating crosslinked with the lowest wt% PEG, **7a**, which suggested that higher crosslinking densities are likely to reduce fouling-release performance (Figure 2-8). Ultimately, these data were probably compromised by the uneven surfaces of all the HBFP-PEG coatings (Figure 2-9). The exact effect the surface has on preventing colonization depends on a combination of the chemical nature of the substrate and the dimensions of the topographical features relative to the spores/sporelings. Spores are attracted to small fissures/depressions in coatings[68] that

also act as good anchorage sites and make sporelings resistant to hydrodynamic forces. Despite these shortcomings in terms of roughness, **8a** displayed release properties similar to that of the fouling-release standard (Silastic T2).

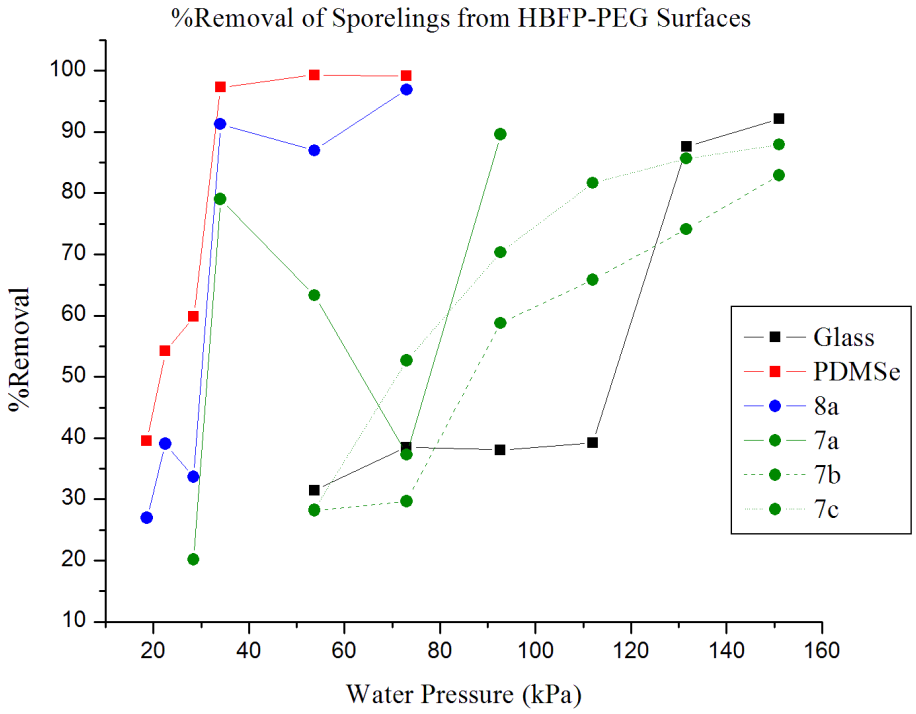

Figure 2-8. Detachment of sporelings of *U. linza* from HBFP-PEG copolymer coatings **7a-c** and **8a**. Coated slides were exposed to the water jet over a range of water pressures. One slide was used at each pressure. PDMSe is Silastic T2.

Figure 2-9. Image showing the dense growth of sporelings of *U. linza* on the surface and in crevices indicating preferential settlement of spores in those regions on **8a** (left) and image of coating after exposure to a water jet removing sporelings from flat areas and shallow depressions on **7b** (middle). A higher magnification image (field of view approx. 2 mm wide) shows sporelings growing densely in small channels (right).

2.6 Conclusions

A two-dimensional array of hyperbranched fluoropolymer-poly(ethylene glycol) crosslinked networks was prepared by the co-deposition and curing of compositionally-unique HBFPs with varying ratios of PEG, towards optimization for applications as anti-biofouling marine coatings. Mixing of the incompatible polymers afforded coatings with nanoscopically-resolved topography and morphology as well as varying physical, mechanical and anti-biofouling properties that were dependent on the polymer

composition and amount of crosslinker used. Thermal transition temperatures and thermal stabilities were varied through HBFP composition and crosslinker loading. Nanoscopic topographical features were observed in every formulation, as visualized by atomic force microscopy. Unique surface effects occurred with water swelling, resulting in an increase in hydrophobicity (verified by SIMS as an increase in fluorine atoms on the surface) and an increase in surface roughness. The Young‟s moduli of water swollen free-standing films were also found to be dependent on the polymer composition and amount of crosslinker incorporated, both of which affected the water uptake. The formulations resisted barnacle cyprid settlement almost entirely and the proportion of diatoms that detached from the **7a-c** coatings at a shear stress of 52 Pa was between 2 and 3 times that of the PDMSe standard. Both **7a** and **8a** displayed good fouling-release against sporelings of *U. linza*, in spite of the data being confounded by irregularities in surface roughness. Overall, the bioassays have provided encouraging results and support the hypothesis that nanoscopic surface complexity in chemistry, morphology and topography lead to materials that are resistant to biological adhesion of marine fouling organisms. This study provided insight into how polymer composition and amount of crosslinker affect the thermal, surface, mechanical and anti-biofouling properties and will be a guide for future formulations in the further development and implementation of these coatings.

2.7 Acknowledgements

Financial support provided by the Office of Naval Research under grant numbers N00014-10-1-0527 (KLW), N00014-08-1-1240 (ASC) and N00011-08-1-0010 (MEC/JAC), the NSF Grant CHE-0750377 (EAS), the NSF REU Grant CHE-0755207 and the W. T. Doherty-Welch Chair (KLW) is gratefully acknowledged. We also thank the Laboratory for Biological Mass Spectrometry (TAMU) for small molecule mass spectral analysis. D. Rittschof and A. B. Brennan are thanked for providing materials utilized in these studies.

CHAPTER III

NORADRENALINE-FUNCTIONALIZED HYPERBRANCHED FLUOROPOLYMER-POLY(ETHYLENE GLYCOL) CROSSLINKED NETWORKS AS DUAL-MODE, ANTI-BIOFOULING COATINGS*

3.1 Original Publication Information

This chapter was originally published as an article in *ACS Nano*.

Collaborative contributions: N. Gohad and A. Mount conducted biological assays and fluorescence microscopy; M. Eller and E. Schweikert performed SIMS; B. Orihuela and D. Rittschof provided barnacle cyprid brood stock.

Modifications to the original document are cosmetic and used only to conform the format of this document or provide uniformity of enumeration. Due to this formatting, compounds may be labeled out of sequential order, but are consistent with the compound numbers in the original publication and do not detract from the coherence of the chapter. Contents found in the supporting information, which was originally a separate document, has been included in the chapter, and schemes and figures have been renumbered to conform to the style of this document.

3.2 Overview

The strategy of decorating anti-biofouling hyperbranched fluoropolymer-poly(ethylene glycol) (HBFP-PEG) networks with a settlement sensory deterrent, noradrenaline (NA), and the results of biofouling assays are presented. This example of a dual-mode surface, which combines both passive and active modes of anti-biofouling, works in synergy to improve the overall anti-biofouling efficiency against barnacle cyprids. The HBFP-PEG polymer surface, prior to modification with NA, was analyzed by atomic force microscopy and a significant distribution of topographical features was observed, with a nanoscopic roughness measurement of 110 ± 8 nm. NA attachment to the surface was probed by secondary ion mass spectrometry to quantify the extent of polymer chain-end substitution with NA, where a three- to four-fold increase in intensity for a fragment ion associated with the NA was observed and 39% of the available sites for attachment were substituted. Cytoskeletal assays confirmed the activity of tethered-NA on adhering oyster hemocytes. Settlement assays showed deterrence towards barnacle cyprid settlement, while not compromising the passive biofouling resistance of the surface. This robust strategy demonstrates methodology for the incorporation of actively anti-biofouling moieties onto a passively anti-biofouling network.

3.3 Introduction

There are significant efforts underway world-wide to produce coatings that can be applied in the marine environment, for instance to address the issue of biofouling on ship hulls, which can result in up to 70% increased fuel consumption and added operational costs.[4,8] Barnacle growth alone can reach 150 kg/m^2 in just 6 months.[1] Marine biofouling has been controlled, traditionally, through the use of anti-biofouling paints that rely on the release of toxic agents,[2] such as organotin compounds, which are banned from use, and copper ablatives, the usage of which is being restricted, with a USA-wide regulatory decision expected in *ca*. 2015.[3,69] Action had been taken to ban the use of organotin paints because of the irreversible accumulation of the leachates in the sediment that results in unwanted environmental effects; similar environmental accumulation of copper in seawater, estimated to be 15×10^6 kg/yr world-wide, is becoming increasingly problematic.[5] Next-generation materials that are environmentally-benign are desired.[70] Leading commercially-available formulations often incorporate low surface energy polymer components, *e.g*., silicones (Intersleek®700, SeaGuard®, *etc*.) and/or fluoropolymers (Intersleek®900, *etc*.), to inhibit initial adhesion of biofouling organisms and promote their release,[41] each by passive modes of action. Anti-biofouling coatings that present tethered biocidal groups, for example quaternary ammonium salts,[22] and commercially-available formulations that leach biocides (Irgarol®, ZPT®, Diuron®, Sea-Nine®)[5] operate by active modes of anti-biofouling. It was hypothesized that the combination of these two distinctive modes of

action would lead to superior anti-biofouling coatings. As our interests are in the development of non-toxic anti-biofouling coatings, we chose to avoid the use of biocidal agents, and instead designed a multi-functional polymer coating that presents bioactive fouling-deterrent molecules[71] across a nanoscopically-complex surface that provides for additional passive anti-biofouling.

Previous studies by our laboratory investigating anti-biofouling coatings comprised of hyperbranched fluoropolymers (HBFP) crosslinked with poly(ethylene glycol)s, (HBFP-PEG),[14] have led to optimization of the chemistries and mechanical properties.[37,38] Fluoropolymers were chosen because of their low surface energy and extensive use in marine applications,[10,47,72] and PEGs were incorporated into the system because of their demonstrated resistance to protein adsorption.[9,17,73] The HBFP-PEG passive mode of anti-biofouling is thought to be generated from a combination of complex surface topographies, morphologies, and compositions over nano- and microscopic dimensions,[35,36,40] inhibiting protein adhesion and whole organism settlement simultaneously.

The possibility of using soluble noradrenaline (NA), an adrenoreceptor agonist that is known to inhibit larval settlement in oysters[74-76] and barnacles,[77,78] as an anti-biofouling agent has been explored previously, without NA being covalently bonded to the substrates.[79] Therefore, NA is an attractive moiety for tethering into environmentally-benign, passively anti-biofouling coatings to add the active mode of action, directly at the surface. Previous studies by Gohad *et al.* probed the interactions between NA tethered to poly(methacrylic acid) (PMAA) and poly(2-hydroxyethyl

acrylate) (PHEMA) brushes and hemocytes of the Eastern Oyster, *C. virginica*.[71] These studies showed that NA molecules covalently linked to polymer brushes retained their bioactivity and were able to induce physiological changes in the hemocytes. Settlement assays using barnacle cyprids identified that the concentration of NA on the surface was sufficient to preserve the ability of NA-conjugated polymers to deter larval settlement. Questions remained, however, as to what extent the NA was covalently bound to the surface and whether advanced anti-biofouling polymer substrates would provide for enhanced performance.

In this work, NA was incorporated into HBFP-PEG to produce a highly-complex, dual-mode anti-biofouling polymer coating, with confirmation of its surface presentation and biological activity. This system utilized a new generation of HBFP bearing ethylene glycol units,[80] which was crosslinked with PEG. After deposition and curing, the passive mode of anti-biofouling was provided by the complex surface topography and chemical heterogeneity. The coating surface properties were characterized by atomic force microscopy and contact angle experiments. Bromoacetyl and bromobenzyl functionalities at the HBFP chain ends, unconsumed during crosslinking, allowed for surface modification reactions with NA. Decoration of the HBFP-PEG with this small molecule provided the active mode of fouling deterrence. The extent of substitution was monitored *via* secondary ion mass spectrometry (SIMS), a versatile technique capable of analyzing a wide range of materials, including polymers, semiconductor assemblies, metals, biological samples and nano-objects.[49-52] The technique employs a primary ion that impinges on a surface, resulting in the emission of secondary ions, electrons and

neutral species.[54] Cluster SIMS exhibits emission from the top 5 to 10 nm of a surface, allowing for the analysis of only the top fraction of a material. Therefore, NA that is sequestered into the bulk of the material, in this study, would not contribute to the mass spectrum obtained. Understanding the surface chemistry and the extent to which the substrate is decorated with this active deterrent allowed for correlation of the surface coverage to biofouling performance. Additionally, a comprehensive characterization study was performed against oyster hemocytes and barnacle cyprids on both unmodified HBFP-PEG and modified NA-HBFP-PEG surfaces to assess the enhanced organismal response to the dual-mode surface.

3.4 Experimental

3.4.1 Materials

Reagents and starting materials were purchased from Sigma Aldrich and used as received unless otherwise noted. 2,3,4,5,6-Pentafluorostyrene (PFS) was purchased from Apollo Scientific (UK) and filtered through a plug of neutral alumina prior to use.

3.4.2 Characterization

Monomers and polymers were characterized by ^{1}H, ^{13}C and ^{19}F nuclear magnetic resonance (NMR) spectroscopies using a Varian Inova 300 MHz spectrometer. ^{1}H and ^{13}C NMR spectra were analyzed using the solvent signal as an internal reference and ^{19}F NMR spectra were analyzed with CF_3COOH as an external standard. IR spectra were obtained on a Shimadzu IR Prestige Attenuated Total Reflectance Fourier-transform Infrared Spectrometer (ATR-FTIR). Spectra were analyzed using IRsolution software package (Shimadzu). High-resolution mass spectrometry (HRMS) was conducted on an Applied Biosystems PE SCIEX QSTAR. Gel permeation chromatography was performed on a Waters Chromatography, Inc. (Milford, MA), 1515 isocratic HPLC pump equipped with an inline degasser, a model PD2020 dual-angle (15° and 90°) light scattering detector (Precision Detectors, Inc.), a model 2414 differential refractometer (Waters, Inc.), and four PL_{gel} polystyrene-*co*-divinylbenzene gel columns (Polymer Laboratories, Inc.) connected in series: 5 μm Guard (50 × 7.5 mm), 5 μm Mixed C (300 × 7.5 mm), 5 μm 10^4 (300 × 7.5 mm), and 5 μm 500 Å (300 × 7.5 mm) using the Breeze (version 3.30, Waters, Inc.) software. The instrument was operated at 35 °C with THF as the eluent (flow rate set to 1.00 mL/min). Polymer solutions were prepared at a known concentration (*ca*. 3 mg/mL) and an injection volume of 200 μL was used. Data collection was performed with Precision Acquire 32 Acquisition program (Precision Detectors, Inc.) and analyses were carried out using Discovery32 software (Precision Detectors, Inc.) with a system calibration curve generated from plotting molecular

weight as a function of retention time for a series of broad polydispersity poly(styrene) standards. Differential scanning calorimetric (DSC) studies were performed on a Mettler-Toledo DSC822[e] (Mettler-Toledo, Inc., Columbus, OH), with a heating rate of 10 ºC/min. The T_g was taken as the midpoint of the inflection tangent, upon the third heating scan. Thermogravimetric analysis was performed under Ar atmosphere using a Mettler-Toledo model TGA/DSC 1 Star[e] system, with a heating rate of 10 ºC/min. Measurements were analyzed using Mettler-Toledo Star software version 10.00c. Atomic force microscopy was performed under ambient conditions in air. The AFM instrumentation consisted of a MFP-3D-BIO AFM (Asylum Research; Santa Barbara, CA) and standard silicon tips (type, OTESPA-70; L, 160 μm; normal spring constant, 50 N/m; resonance frequency, 246-282 kHz). Contact angles were measured as static contact angles using the sessile drop technique[53] with an Attension Theta optical tensiometer (Biolin Scientific). Drops were fitted with a Young-Laplace formula to calculate the static contact angle in the Theta software (Biolin Scientific). The reported values are an average of five such measurements on different regions of the same sample. Fluorescence microscopy was carried out using a Nikon Eclipse TiE microscope equipped with a CoolSnap HQ2 (Roper Scientific) mono-chrome CCD camera and appropriate filter sets for the fluorophores used. Confocal microscopy was performed using a Nikon Eclipse TiE microscope equipped with a Nikon C1Si spectral confocal with appropriate laser lines and filter sets for DAPI, FITC, TRITC fluorophores.

3.4.3 Synthesis

4-[Oxy(tri(ethylene glycol))]-2,3,5,6-tetrafluorostyrene (4). To a stirring solution of sodium hydride (60 wt% dispersion in mineral oil, 4.95 g, 124 mmol) in THF (400 mL) in a 1000 mL two-neck round-bottomed flask suspended in an ice bath, was added tri(ethylene glycol) (TrEG) (41.3 mL, 309 mmol), followed by the addition of PFS (14.2 mL, 20.0 g, 103 mmol). The solution was allowed to warm to room temperature and with stirring under N_2 for 14 h. The reaction mixture was then concentrated *in vacuo*, dissolved in deionized water (300 mL) and was extracted with ethyl acetate (4 x 300 mL). The organic fractions were combined, dried over anhydrous $MgSO_4$, filtered and concentrated *in vacuo* to afford a clear, pale yellow oil. Further purification by silica gel flash chromatography using 10% MeOH in DCM as the eluent afforded **4** as a clear, colorless oil in 62% yield (20.6 g). T_{decomp}: 362 °C, 74% mass loss @ 500 °C. IR = 3600-3200, 3050-2800, 1643, 1489, 1358, 1288, 1250, 1080, 941 cm^{-1}. ^{1}H NMR (acetone-d_6, ppm): δ 6.60 (dd, *J* = 12 Hz and 18 Hz, 1H, H_2C=C***H***-R), 5.96 (d, *J* = 18 Hz, 1H, ***H***(H)C=CH-R (*trans*)), 5.65 (d, *J* = 12 Hz, 1H, H(***H***)C=CH-R (*cis*)), 4.38 (t, *J* = 5 Hz, 2H, TFS-O-C***H***$_2$-CH_2-OR), 3.78 (t, *J* = 5 Hz, 2H, TFS-O-CH_2-C***H***$_2$-OR"), 3.40-3.70 (m, 8H, R-O-(C***H***$_2$-C***H***$_2$-O-C***H***$_2$-C***H***$_2$-OH) ppm. ^{13}C-NMR (acetone-d_6, ppm): δ 147.2, 143.7, 143.0, 140.2, 137.3, 122.5, 122.4, 122.3, 122.2, 111.0, 74.8, 73.2, 71.1, 70.8, 70.5 and 61.6 ppm. ^{19}F NMR (acetone-d_6, ppm): δ -147 (m, *ortho*-***F*** to C=CH_2), -159 (m, *meta*-***F*** to C=CH_2) ppm. HRMS m/z calculated for $C_{14}H_{16}F_4O_4$ $[M + H]^+$ 325.10 Da, found 325.1063 Da.

4-[Oxy(tri(ethylene glycol))bromoisopropionyl]-2,3,5,6-tetrafluorostyrene (5). To a stirring solution of triethylamine (7.70 mL, 55.5 mmol) in THF (259 mL) in a 500 mL two-neck round bottom flask was added **4** (5.00 g, 15.4 mmol). The solution was cooled to 0 °C and 2-bromoisopropionyl bromide (3.99 g, 18.5 mmol) was added dropwise. The solution was allowed to warm to room temperature with stirring under N_2 for 16 h. The reaction mixture was filtered, the filtrate was then concentrated *in vacuo*, was dissolved in dichloromethane (500 mL) and was washed with deionized water (4 x 500 mL). The organic fraction was dried over anhydrous $MgSO_4$, filtered and concentrated *in vacuo* to afford a clear, pale yellow oil. Further purification by silica gel flash chromatography using 30% ethyl acetate in hexanes as the eluent afford **5** as a clear, colorless oil in 82% yield (5.81 g) which was stored at 4 °C to prevent side-reaction. T_{decomp}: 297 °C, 70% mass loss @ 500 °C. IR = 3050-2800, 2874, 2747, 1738, 1647, 1485, 1451, 1429, 1406, 1377, 1354, 1335, 1223, 1153, 1119, 1078, 1030, 968, 937, 858, 762, 677, 648 cm^{-1}. ^1H NMR (Acetone-d_6, ppm): δ 6.60 (dd, *J* = 12 Hz and 18 Hz, 1H, H_2C=C***H***-R), 5.96 (d, *J* = 18 Hz, 1H, ***H***(H)C=CH-R (*trans*)), 5.65 (d, *J* = 12 Hz, 1H, H(***H***)C=CH-R (*cis*)), 4.6 (q, *J* = 5 Hz, 1H, R-C(***H***)(Br)CH_3), 4.5 (t, *J* = 5 Hz, 2H, TFS-O-C***H***$_2$-CH_2-OR), 4.3 (t, *J* = 5 Hz, 2H, R-CH_2-C***H***$_2$-O(O)C-R‟), 3.9 (t, *J* = 5 Hz, 2H, TFS-O-CH_2-C***H***$_2$-OR), 3.8-3.6 (m, 6H, R-O-C***H***$_2$-C***H***$_2$-O-C***H***$_2$-CH_2-O(O)C-R‟), 1.8 (d, *J* = 5 Hz, 3H, R-C(H)(Br)C***H***$_3$) ppm. ^{13}C-NMR ($CDCl_3$, ppm): δ 171.3, 145.7, 144.0, 141.8, 140.2, 136.4, 122.0, 121.8, 110.6, 74.1, 70.6, 70.1, 64.9, 55.6 and 30.5 ppm. ^{19}F NMR (Acetone-d_6, ppm): δ -147 (m, *ortho*-***F*** to C=CH_2), -159 (m, *meta*-***F*** to C=CH_2) ppm. HRMS m/z calculated for $C_{17}H_{19}BrF_4O_5$ $[M + H]^+$ 459.04 Da, found 459.0439 Da.

Hyperbranched Fluoropolymer (HBFP) (2). To a dry 50 mL Schlenk flask equipped with a stir bar was added **5** (5.00 g, 10.9 mmol, 1 equiv.), PFS (6.34 g, 32.7 mmol, 3 equiv.), PMDETA (3.33 g, 19.2 mmol, 2 equiv./Br), CuBr (1.57 g, 10.9 mmol, 1 equiv./Br) and anisole (100 mL). The solution was degassed *via* freeze-pump-thaw (3x), the vessel was backfilled with N_2 and then lowered into an oil bath set at 65 °C and the reaction was allowed to proceed for 20 h. The polymerization was quenched by opening the flask to air and submerging the flask in liquid nitrogen. Once thawed, the contents were dissolved in dichloromethane (450 mL), eluted through a plug of alumina to remove the catalyst, concentrated *in vacuo*, and the product was isolated by precipitation into cold hexanes (3 x 1.2 L) to afford a white powder of **2** in 62% yield (7.03 g). M_w^{GPC} = 17400 Da, M_n^{GPC} = 8600 Da, M_w/M_n = 1.72. T_g = 73 °C. T_{decomp}: 310 °C, 85% mass loss @ 500 °C. IR = 2947, 2878, 2361, 1744, 1651, 1497, 1296, 956, 864 cm^{-1}. ^{1}H NMR ($CDCl_3$, ppm): 4.6-4.0 (br, m, TFS-O-C***H***$_2$-CH_2-OR and R-CH_2-C***H***$_2$-O(O)C-R‟‟), 4.0-3.4 (br, m, R-O-C***H***$_2$-C***H***$_2$-OR‟‟), 3.1-1.5 (br, m, C***H***$_2$-C***H***(R)-backbone), *δ* 1.5-0.7 (br m, C-C***H***$_3$) ppm. ^{13}C-NMR ($CDCl_3$, ppm): δ 176.6, 144.7, 140.7, 137.6, 122.2, 114.7, 74.3, 70.8-70.0, 68.8, 63.6, 41.7-32.1, 30.7-29.7, 24.7 ppm. ^{19}F NMR ($CDCl_3$, ppm): δ -143 (br, m, *o*-F (PFS) and *o*-F (TFS)), -157 (br, m, *p*-F (PFS) and *m*-F (TFS)), -162 (br, m, *m*-F (PFS)) ppm.

General Procedure for the Preparation of HBFP-PEG Films (3). To a scintillated vial was added **2** (0.70 g) and 1500 Da DA-PEG (0.35 g, 33 w/w% of total mass) and mixed in THF (8 mL) until homogenous. A catalytic amount of diisopropylethylamine (100 μL) was syringed into the vial. Approximately 0.2 mL of

the solution was drop cast onto pre-cut 1 cm^2 glass microscope slides. The THF was allowed to evaporate over *ca.* 20 min. period affording a pre-gel. The slides were placed in an oven purged with N_2 at 110 °C for 45 min to cure followed by submersion in a water bath overnight to leach any VOCs and release a free standing film of **3**. θ_{H20} = 76 ± 2°. RMS Roughness = 110 ± 8 nm.

General Procedure for the Preparation of Noradrenaline-functionalized HBFP-PEG Films (1). Samples of **3** (1 x 1 cm^2) were placed individually into wells of a 12-well plate. To each well was added a solution of noradrenaline·HCl in pH 7.4 PBS (*ca*. 2 mL, 1 mg/mL). The plate was covered in parafilm and aluminum foil and placed on an orbital shaker at 4 ºC for 48 h. The solution was decanted and the coatings were rinsed with fresh, cold PBS, followed by brief sonication in cold PBS and were stored dry under N_2 at -20 °C prior to use.

3.4.4 Surface Studies

SIMS. The instrument used in these studies is a custom built instrument equipped with a custom built C_{60} source capable of producing C_{60}^{+2} at 43 keV total impact energy.[54,56,81] The instrument is equipped with a 1 m linear time of flight (ToF) and an electron emission microscope. All samples were analyzed in negative ion mode using the emitted electrons as the start for the ToF measurement. SIMS analysis was performed on a series of samples throughout the production/modification of the HBFP-PEG: two HBFP-PEG samples after hydration, unmodified HBFP-PEG after incubation

in PBS and modified NA-HBFP-PEG after incubation in NA/PBS. Two or three 200 μm radius spots were analyzed for each sample to ensure sample consistency.

3.4.5 Biological Assays

Oyster Culture. Eastern Oyster (*Crasostrea Virginica*) adults were purchased from Pemaquid Oyster Company Inc. (Waldoboro, Maine). The oysters were maintained in a 180 Gal (681 L) tank at 18 °C in artificial seawater (ASW) at 21% salinity with saturating levels of dissolved oxygen. Shellfish Diet 1800® (Reed Mariculture Inc.) was used to feed the animals. Hemocytes (immune cells) were obtained by notching the oyster shell with a cement saw and extracting the hemolymph from the adductor muscle with a 22-guage needle affixed to a disposable syringe.[82] Depending on the size and weight of the oyster, 1-2 ml of hemolymph was extracted.

Cytoskeletal Assay I. Cytoskeletal assay-I was performed as described by Gohad *et al*.[71] Briefly, 500 μL of hemolymph was aliquated onto unmodified HBFP-PEG and NA-HBFP-PEG substrates, and hemocytes were allowed to settle on surfaces for 60 min. Cells were then fixed with 4% formaldehyde freshly prepared from paraformaldehyde, made up in phosphate buffer saline (PBS) for 40 min. Surfaces were rinsed twice for 5 min each on an orbital shaker to remove any unreacted formaldehyde. For staining with fluorescent phalloidin labeling F-actin, cells were permeabalized by incubating in 0.1% Triton-X100 in PBS for 5 min. Surfaces were then washed twice for 5 min each, then incubated in a 50 μM solution of TRITC-Phalloidin (Sigma) for 45

min, and washed twice to remove excess phalloidin. Hemocytes were then counterstained with DAPI, labeling nuclei, and fluorescence microscopy was carried out.

Cytoskeletal Assay II. Hemocytes incubated on HBFP-PEG and NA-HBFP-PEG were fixed and permeabalized as described above. Cells on surfaces were then blocked using a 4% solution of bovine serum albumin (Sigma) made up in PBS for 40 min. After which, the surfaces were incubated in a 1:500 dilution of anti-beta tubulin antibody (Developmental studies hybridoma bank) over night at 4° C. The surfaces were then washed twice for 5 min each and incubated with a 1:1000 dilution of AlexaFluor-555 fluorescent secondary antibody (Life technologies) for 1 h. Surfaces were washed twice for 5 min each and incubated with a 50 μM solution of FITC-Phalloidin (Sigma) labeling F-actin for 45 min, the samples were counterstained with DAPI, labeling nuclei, and confocal microscopy was carried out.

Control samples for Cytoskeletal assay II (hemocytes on HBFP-PEG and NA-HBFP-PEG) were labeled only with the fluorescent secondary antibody to rule out any non-specific interactions between the secondary antibody and samples. Control samples did not show any non-specific labeling with the fluorescent secondary antibody.

Unstained HBFP-PEG and NA-HBFP-PEG with hemocytes were also used as auto-fluorescence controls and inspected under the microscope using the same excitation and emission filter-sets and imaging modalities (wide field fluorescence and confocal microscopy) for DAPI, FITC and TRITC fluorophores. Unstained samples were not found to be auto-fluorescent in either of the imaging modalities.

Cyprid Settlement Assays. Cyprid (settlement stage) larvae of the striped barnacle *Balanus amphitrite* were obtained from Dr. Dan Rittschof's laboratory at Duke University Marine Laboratory and were shipped and handled as described previously.[78] HBFP-PEG and NA-HBFP-PEG surfaces were placed in 24 well plates (Kimtec), filled with ASW and washed several times and allowed to equilibrate with ASW for 10 min. The 1 x 1 cm^2 samples covered majority of the surface area of the well bottom. Approximately 16 to 20 cyprids were added to each well in ASW, after which the plates were covered with aluminum foil and placed in a humid chamber at room temperature for 48 h. At the end of the incubation period, number of settled cyprids was counted for each well using the Nikon- AZ100 macro-scope. The percentage of total larvae settled was calculated for NA-conjugated and control surfaces, and subjected to a one-way ANOVA with the significance cutoff set to $p \leq 0.05$.

3.5 Results and Discussion

The dual-mode, anti-biofouling surface, **1** (Scheme 3-1) was designed to combine amphiphilic, morphologic and topographic complexities of HBFP-PEG with the active deterrence of NA. The synthetic approach, therefore, relied upon reactive bromoacetyl and bromobenzyl functionalities at the chain ends of HBFP, **2**, to undergo the crosslinking reactions with diamino-terminated PEG, affording **3**, and also the chemical modification reactions with NA to give **1**. The particular HBFP utilized, **2**, was of a unique chemical composition and structure, by linking hydrophobic and

hydrophilic characteristics on a molecular level throughout the hyperbranched polymer framework.[80] The HBFP was synthesized *via* atom transfer radical self-condensing vinyl copolymerization (ATR-SCVCP) to control the molecular weight of the polymer and yield the reactive chain ends. The preparation of **2**, therefore, began from the nucleophilic aromatic substitution of the *para*-fluorine of 2,3,4,5,6-pentafluorostyrene (PFS) with an excess of tri(ethylene glycol) (TrEG), to give **4**, followed by esterification with 2-bromoisopropionyl bromide to yield the amphiphilic initiating monomer (inimer) **5** for ATR-SCVCP. Copolymerization of **5** with three molar equivalents of PFS achieved **2**, bearing TrEG throughout the backbone of the polymer.[14,80] A robust free-standing thin film, **3**, was then obtained from deposition and curing of **2** with a diamino-poly(ethylene glycol) (DA-PEG) in the presence of base. Incubating the crosslinked networks in water leached residual organic compounds and also released **3** from the substrate. Films of **3** were incubated in a PBS buffer solution of noradrenaline (NA) at 4 °C in the dark, to allow for substitution of the alkyl bromide functional handles on the surface to yield the noradrenaline-modified HBFP-PEG film, **1** (NA-HBFP-PEG). A series of replicates, **1a-d** and **3a-d**, was prepared to allow for complete physicochemical, compositional and biological studies.

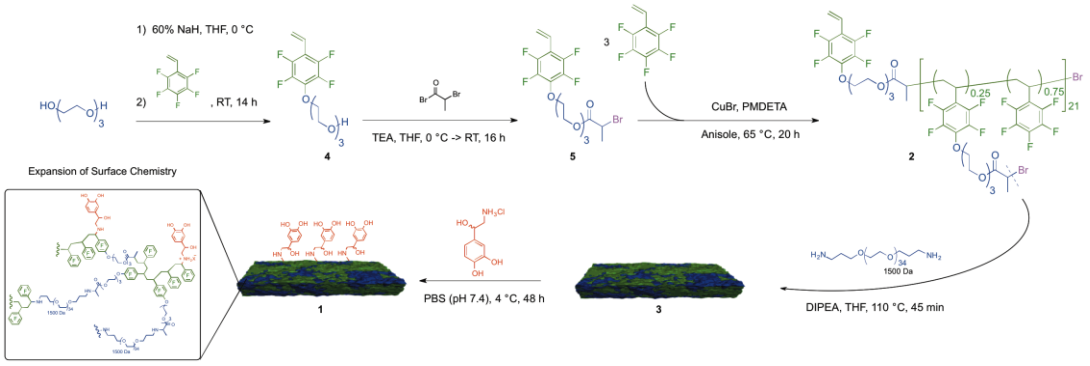

Scheme 3-1. Synthesis of noradrenaline-functionalized HBFP-PEG thin films (NA-HBFP-PEG), **1**.

The materials exhibited complex surface topography and chemical heterogeneity that were created through the co-deposition and curing of incompatible HBFP and PEG components, where the HBFP and PEG segregated into their respective domains through differences in topology and composition, yet were covalently trapped on the molecular level through covalent bond formation. The properties of the film surfaces were observed by atomic force microscopy and static contact angle (Figure 3-1). It was found that sub-micron topographical features were distributed across the surface, with an overall RMS roughness of 110 ± 8 nm and the film surface had a static water contact angle of 76 ± 2°. This combination of complex nanoscopic topography and amphiphilicity presents obstacles for a settling organism, which complicates the search for an area suitable for adhesion, resulting in passive resistance to biofouling. It was expected that marine invertebrate larvae, such as barnacle cyprids, would sense surface-

bound NA unfavorably and would avoid settling on those areas, resulting in an active fouling deterrence mode. However, AFM and contact angle measurements after NA conjugation gave data similar to those for the unmodified HBFP-PEG, preventing confirmation and quantification of the presence of NA on **1**.

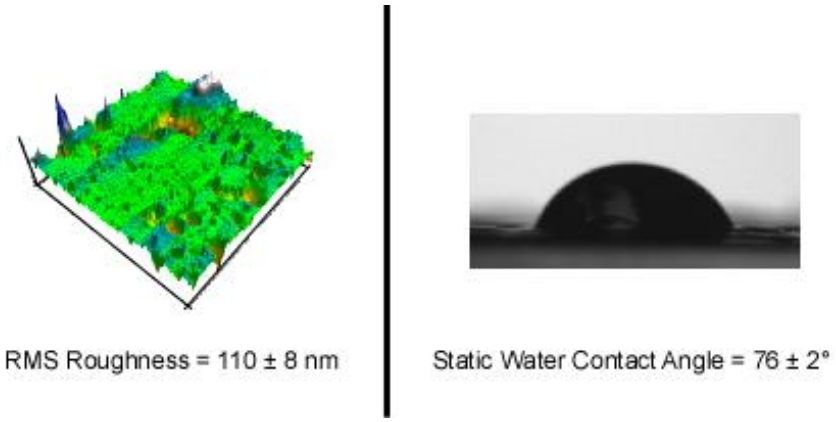

Figure 3-1. Atomic force microscopy (AFM) of HBFP-PEG films, **3**, (left) and static water contact angle (right) after swelling in water overnight. AFM → scan size = 50 × 50 μm^2; z axis = 1.0 μm.

Secondary ion mass spectrometry (SIMS) was employed to confirm the covalent attachment of NA to the polymer backbone. In SIMS, the primary ion plays a key role in the emission of ions, specifically the molecular ions, and for this reason C_{60} was selected as the primary ion. C_{60} is surface sensitive, generates secondary ion emission from the top 5 - 10 nm of a substrate, and displays higher molecular ion emission

compared to atomic and small cluster projectiles.[83,84] The SIMS experiments for this study were conducted in the super static regime, where less than 0.1% of the surface is impacted. This limitation ensured that each time the surface was impacted by a primary ion, an unperturbed area of the surface was sampled. Super static measurements were conducted in the event-by-event bombardment-detection mode of operation, where a single primary ion impacted on the surface and the secondary ions were collected and analyzed prior to subsequent primary ions impacting the surface. All secondary ions detected in a single impact originated from a 10 nm radius on the surface.[85] To minimize variances between surfaces, a single HBFP-PEG film, **3a**, was obtained from a THF solution of HBFP and PEG (Scheme 3-1). The film was divided in half to afford two films with "identical" surfaces. These unmodified samples were analyzed by event-by-event cluster SIMS and found to have equivalent mass spectra (Figure 3-2).

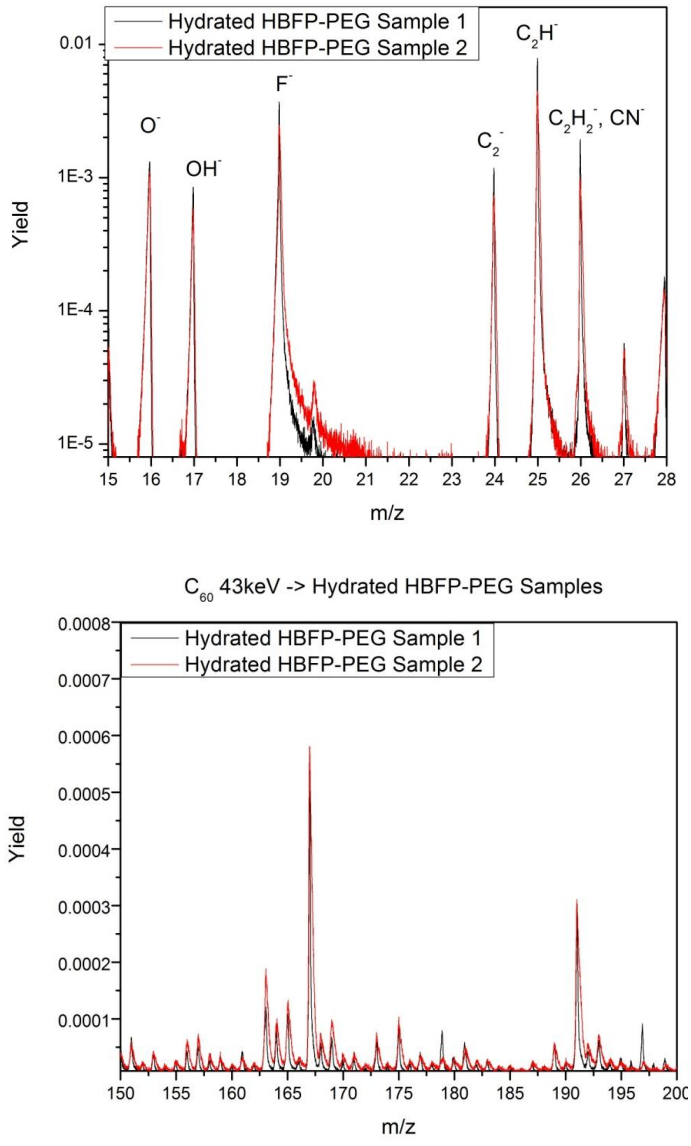

Figure 3-2. Mass spectra for the two hydrated HBFP-PEG samples pre-modification reactions. Top) 15 – 28 m/z; Bottom) 150 – 200 m/z.

Three different regions were investigated for each sample to ensure sample consistency. In these spectra, we observed several peaks from the HBFP portion of the crosslinked network corresponding to the PFS monomer, including 191, 167, and 19 m/z. Larger fragments of the polymer structure were also detected, such as m/z 353, a fragment of the inimer-based repeat units. One film was modified by incubation in a noradrenaline/PBS solution to give **1a**, followed by sonication and washing to ensure removal of physically-entrapped NA. The other film underwent the same procedure, in PBS solution, to yield **3a**. Both surfaces were analyzed after washing (Figures 3-3 and 3-4). A quantitative estimate of surface coverage of PFS was calculated,[86] and we found that the coverage of the PFS was 70% ± 5% for **3a** and 77% ± 2% for **1a**. These results supported sample consistency, given that there was a similar detectable amount of PFS on either of the unmodified HBFP-PEG or modified NA-HBFP-PEG surfaces.

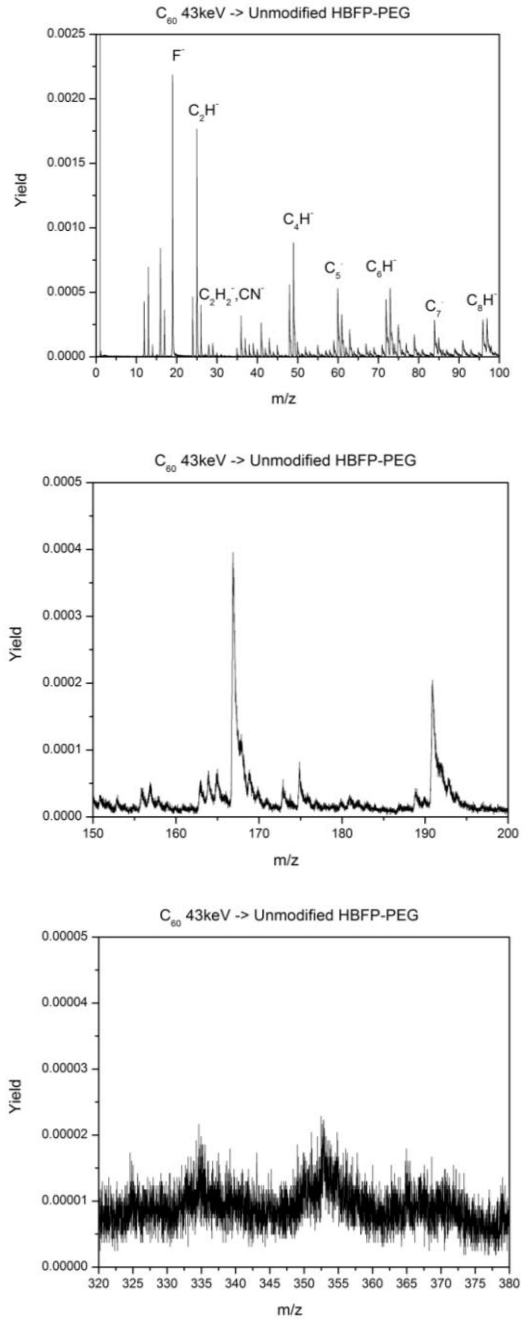

Figure 3-3. Mass spectra for unmodified HBFP-PEG in 3 mass ranges. Top) 0 – 100 m/z; Middle) 150 – 200 m/z; Bottom) 320 – 380 m/z.

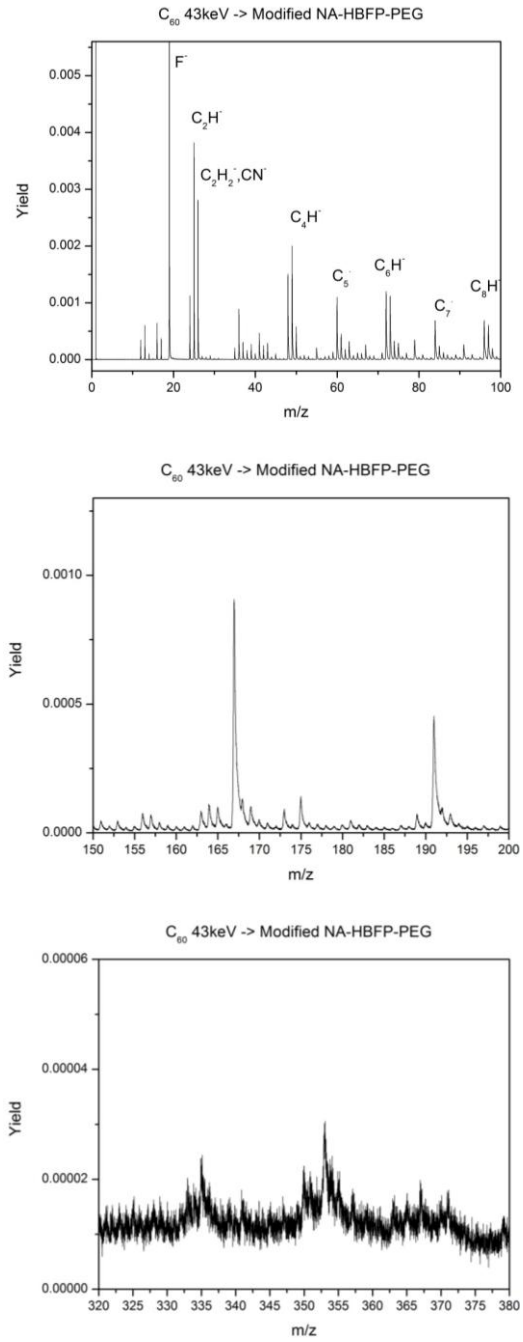

Figure 3-4. Mass spectra for modified NA-HBFP-PEG in 3 mass ranges. Top) 0 – 100 m/z; Middle) 150 – 200 m/z; Bottom) 320 – 380 m/z.

The existence of the covalently bound NA was substantiated by the presence of the fragment ion CN^- in the mass spectra. The intact noradrenaline was not observed due to its poor ionization in negative mode. Indirectly, NA was quantified by observing the change in yield, Y, defined as the number of SIs detected per projectile impact for a chosen m/z, for the nominal m/z 26 ion between the unmodified and modified samples. Although many fragment ions could potentially contribute to the m/z 26 peak (CN^- from the PEG chain ends, $C_2H_2^-$ from the HBFP backbone and PEG backbone), it was expected that there was an equal contribution from the polymer backbone in **3a** and **1a** because both samples were obtained from a single parent film. This assumption was verified by the consistent coverage of PFS on each surface. The 3- to 4-fold increase in m/z 26 yield (Figures 3-5 and 3-6) between the surfaces of **3a** and **1a** was a strong indication of NA on the surface; however, it did not indicate the selective attachment of the molecule at the labile chain ends.

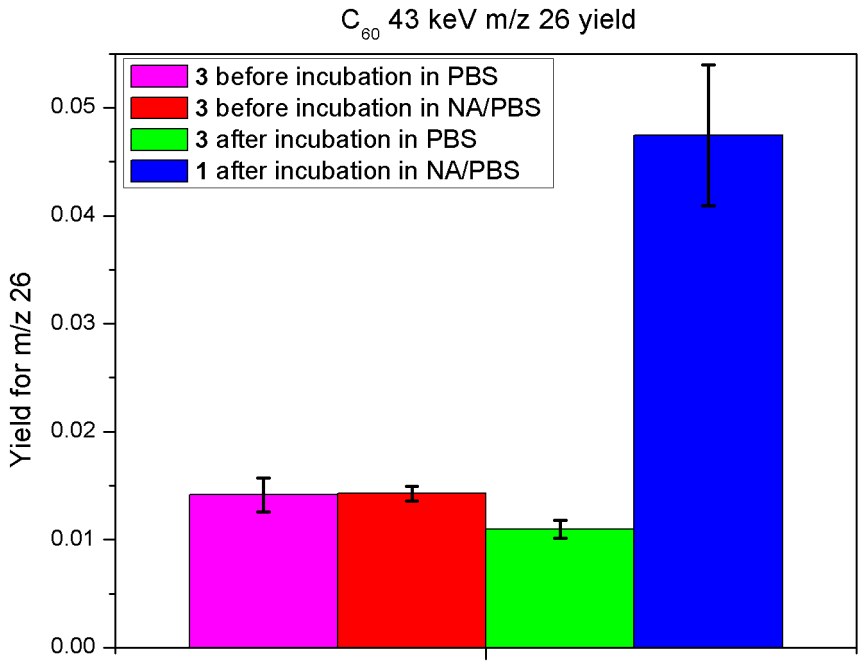

Figure 3-5. Yields for m/z 26 for **3a** (before and after PBS buffer, and before NA/PBS buffer) and **1a** (after NA/PBS buffer).

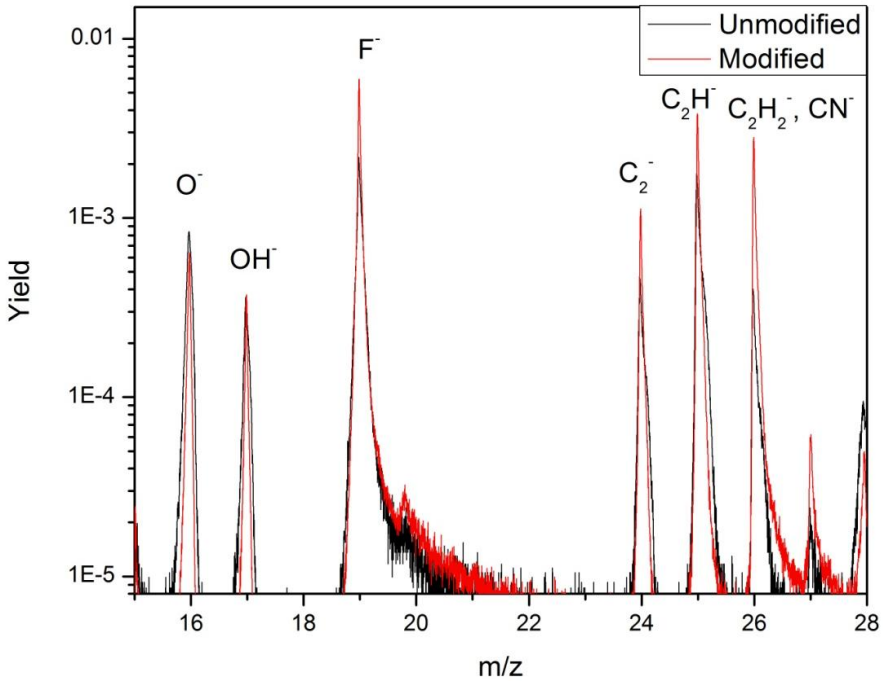

Figure 3-6. Comparison of m/z 26 with short range mass spectra for unmodified HBFP-PEG and modified NA-HBFP-PEG.

To probe substitution of labile Br with NA, a calculation comparing the relative number of Br sites on **3a** and **1a** was employed (Equation 3-1). On the surface of the films, specifically from the HBFP portion of the crosslinked network, there are finite numbers of initial Br sites, which can be viewed as both random and disperse. The initial amount of sites in **3a** was determined by calculating the ratio of Br^- to F^- yields. After tethering NA to the surface, the remaining sites were found by the same calculation for **1a**. The quotient of the ratios of the final sites (0.027 ± 0.003) to the

initial sites (0.044 ± 0.002) yielded the percentage of Br sites that remained on the surface after modification (Table 3-1). We found that 61% of the Br sites remained after incubation with noradrenaline, indicating that NA had replaced 39% of the Br sites on the surface. The substitution of Br with NA is supported by the increase in the yield of m/z 26 (Figure 3-2). It can be shown at the 85% confidence level that the Br^- yield for the 3a samples (mean value of 0.0038) are significantly different from the Br^- yields measured from sample 1a (mean value of 0.0032), further indicating the replacement of Br.

$$\left[\frac{Y_{Br^-,NA\text{-}HBFP\text{-}PEG}}{Y_{F^-,NA\text{-}HBFP\text{-}PEG}} \Big/ \frac{Y_{Br^-,HBFP\text{-}PEG}}{Y_{F^-,HBFP\text{-}PEG}}\right] * 100\% = \text{percentage of unconsumed sites}$$

Equation 3-1. Ratio of secondary ion yields of Br^- to F^- for NA-HBFP-PEG to HBFP-PEG.

Table 3-1. Secondary ion yields for Br and F from unmodified **3a** and NA-modified **1a**.

Sample Name	**Yield Br^-**	**Yield F^-**	**Y_{Br^-}/Y_{F^-}**
3a (region 1)	0.0038	0.083	0.046
3a (region 2)	0.0033	0.080	0.042
3a (region 3)	0.0041	0.093	0.044
3a (Avg. ± S.D.)			**0.044 ± 0.002**
1a (region 1)	0.0034	0.120	0.029
1a (region 2)	0.0027	0.117	0.023
1a (region 3)	0.0035	0.122	0.029
1a (Avg. ± S.D.)			**0.027 ± 0.003**

The presence of NA on the surface allowed us to test the hypothesis that the NA would act in conjunction with the complicated surface features to improve the overall anti-biofouling efficiency of the system. Hemocytes (cells) of the Eastern Oyster (*Crassostrea virginica*) were used to determine if the NA molecules retained their bioactivity after covalent conjugation to the HBFP-PEG surface. Oyster hemocytes have been found to express adrenergic receptors (target receptors for NA) and the effects of NA on oyster hemocyte physiology have been well documented. In fact, hemocytes are known to undergo apoptosis (programmed cell death) upon NA stimulation.[87-90] Since

oysters are a prominent fouling species and their cells express the target receptors, hemocytes make for a good model system to screen NA-conjugated polymer surfaces.[71,87] A similar strategy was employed by Gohad *et al.* to observe interactions between NA-conjugated PHEMA (poly(hydroxyethyl methacrylate)) and PMAA (poly(methacrylic acid)) polymer brushes and oyster hemocytes.[71] In that study, a cytoskeletal assay was used to confirm that covalently linked NA molecules were able to induce apoptosis in the adhering hemocytes, which was demonstrated by the loss of cell membrane integrity, abnormal accumulation of cytoskeletal elements and finally enucleation (dislodgment of the nucleus) and membrane blebbing, hallmarks of the apoptotic progression.

A cytoskeletal assay was employed to observe the effects that unmodified HBFP-PEG and modified NA-HBFP-PEG films had on settled cell physiology. Cells adhering to unmodified HBFP-PEG surfaces **3** (Figures 3-7 (A) and 3-7 (B)) exhibited a diffused pattern of actin filaments and an absence of stress filaments. The cells had intact cell membranes and exhibited a normal morphology, indicating that HBFP-PEG surfaces on their own did not affect the cells adversely. In contrast, cells adhering to NA-HBFP-PEG surfaces, **1**, showed stressed actin filaments, an abnormal aggregation of actin, and disintegrated cell membranes. Extensive enucleation was also evident, indicating that cells interacting with NA-HBFP-PEG surfaces underwent apoptosis (Figures 3-7 (C) and 3-7 (D)). To confirm the effects of NA-HBFP-PEG surfaces on hemocyte physiology, the cytoskeletal assay was further modified. Gohad *et al.* had used F-actin as a marker to demonstrate cytoskeletal deterioration.[71] In this study, β-tubulin, a component of

microtubules, was used in addition to F-actin. Microtubules, along with F-actin, form the cytoskeleton of cells and any adverse effects of the cell-surface interaction can be confirmed by observing these cytoskeletal elements. Cells interacting with unmodified HBFP-PEG showed no abnormal distribution of either F-actin or β-tubulin (Figure 3-8 (A)). Actin stress filaments were absent and the microtubules were organized around the nucleus, with the nucleus serving as the organizing center, indicating that unmodified HBFP-PEG, **3**, did not adversely affect the cytoskeleton, and in turn, cell physiology. Cells interacting with NA-HBFP-PEG, **1**, not only displayed stressed actin filaments, but also showed abnormal accumulation of microtubules with the loss of a centrally organized structure (Figure 3-8 (B)).

The hemocytes not being able to internalize the receptors, considering that the NA molecules were covalently tethered to polymer surfaces, could lead to hyper-stimulation of the hemocyte β-adrenergic receptors (β-AR), which could support the observed apoptosis.[71] The aberrant signaling caused by a hyper-stimulated β-AR could result in the observed apoptosis in hemocytes that interacted with NA-HBFP-PEG.

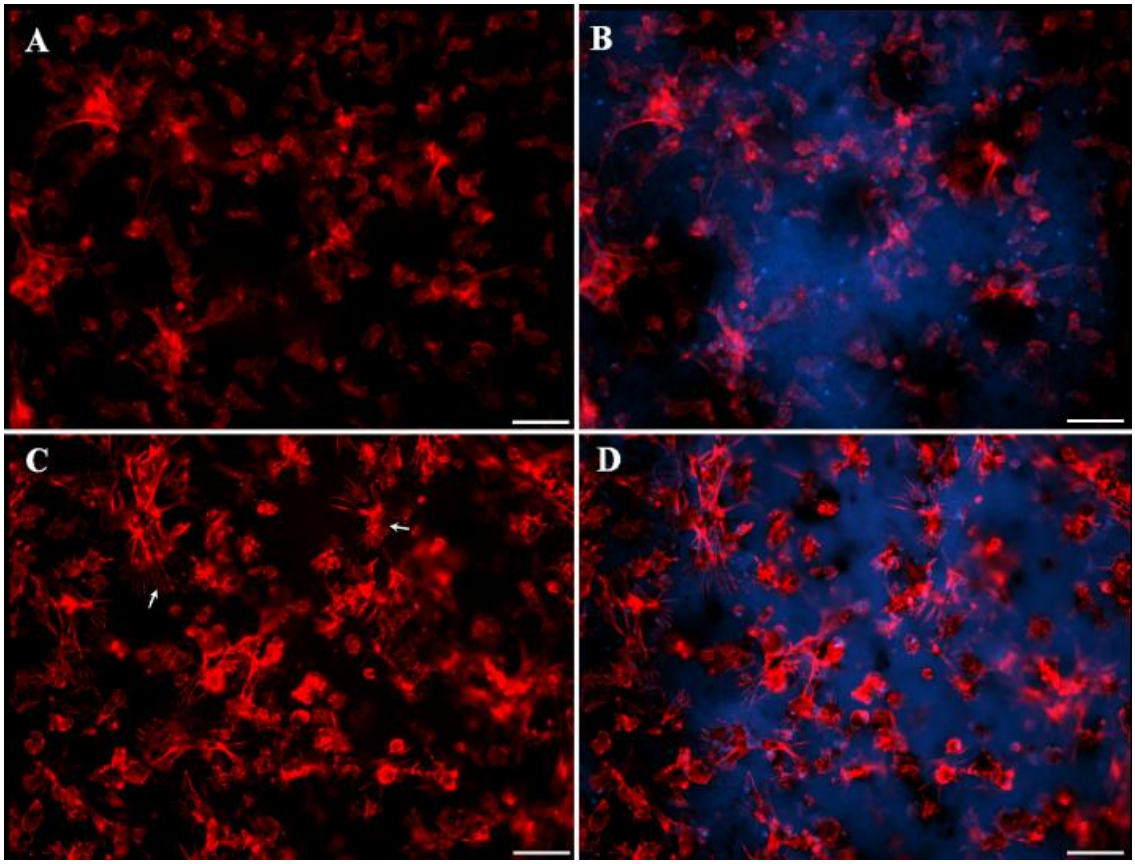

Figure 3-7: Cytoskeletal assay I. A-B) Fluorescent micrograph of hemocytes interacting with unmodified HBFP-PEG surfaces stained with fluorescent phalloidin labeling F-actin (red) and DAPI labeling nuclei (blue) display a normal morphology, intact cell membranes and lack of actin stress filaments. C-D) Hemocytes interacting with NA-HBFP-PEG surfaces on the other hand show an abnormal morphology with disintegrated cell membranes, presence of actin stress filaments, hallmarks of the apoptotic cascade. Scale bar A-D: ~30 µm.

Gohad *et al.* postulated scenarios to explain the observed cytoskeletal deterioration in hemocytes interacting with NA-conjugated polymer surfaces.[71] The observed cytoskeletal deterioration could be a direct indicator of end stages of the apoptotic cascade, as a result of NA induced stimulation of the hemocyte (β-AR). β-AR stimulation is known to activate L-type Ca^{2+} channels, leading to influx and overload of Ca^{2+} which then leads to apoptosis.[71,91-93] In rat cardiomyocytes, β-AR stimulation induces microtubule disassembly *via* cAMP-mediated Ca^{2+} overload.[94] From the observed results (Figure 3-8 (B)) it is possible that hyper-stimulation of β-AR by polymer-tethered NA molecules could lead to microtubule disassembly in hemocytes. G-protein coupled receptor kinase-2 (GRK2) is a signal transducer that mediates the effects of an activated (agonist bound) GPCR (G-protein coupled receptor) on the cytoskeleton by forming a complex with tubulin.[95] A hyper-activated GPCR could lead to unregulated GRK2-tubulin complex formation causing tubulin to abnormally accumulate at the plasma membrane, which could explain the observed loss of a centrally-organized structure (Figure 3-8 (B)).[71] The observed actin stress filaments and disintegrated actin filaments could also be results of the apoptotic cascade. Caspases, mediators of apoptosis, cleave actin, which in turn is targeted to mitochondria and regulates the release of Ca^{2+} through inositol triphosphate and ryanodine-sensitive calcium stores. This process leads to the accumulation of Ca^{2+} in the mitochondrial matrix, forming a feedback loop that progresses the apoptotic cascade even further.[71,96]

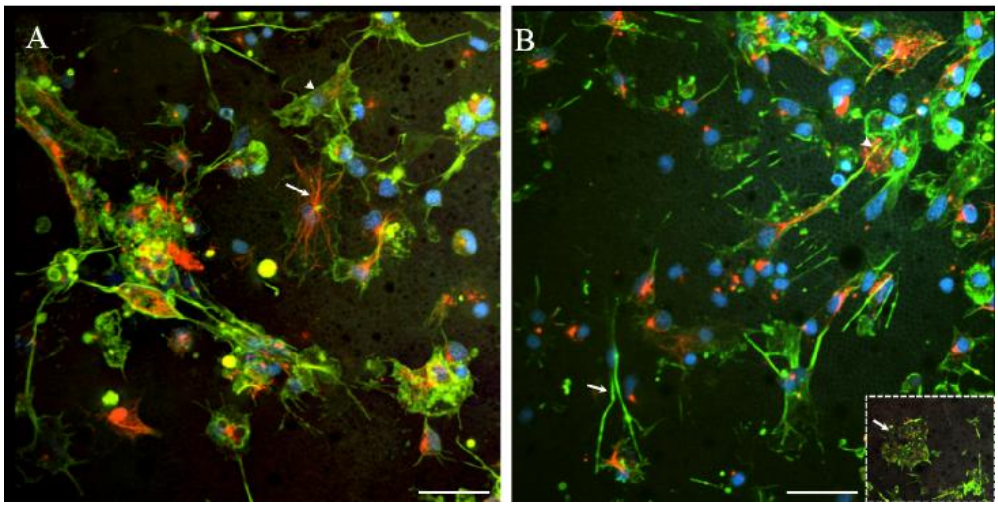

Figure 3-8: **Cytoskeletal assay II.** A) Laser scanning confocal micrograph of hemocytes interacting with HBFP-PEG surfaces stained with phalloidin labeling F-actin (green), anti β-tubulin antibody labeling microtubules (red) and DAPI labeling nuclei (blue) display a normal morphology, intact cell membranes (arrow head), lack of actin stress filaments and microtubules organized around the nucleus as the organizing center (arrow). B) Hemocytes interacting with NA-HBFP-PEG surfaces, on the other hand, show disintegrated cell membranes (inset box, arrow) along with actin stress filaments and abnormal accumulation of actin (arrow). The microtubules seem to have lost the centrally organized structure and accumulate in the cytoplasm or near plasma membranes (arrow head) indicating progression of the apoptotic cascade. Scale bars: ~20 μm.

Barnacle cyprid settlement assays showed that cyprid settlement on NA-HBFP-PEG was significantly reduced as compared to unmodified HBFP-PEG surfaces, indicating that cyprid larvae could sense the HBFP-tethered NA molecules and as a result were deterred from settling (Figure 3-9). When exposed to micromolar solutions of NA, barnacle cyprids are known to lose their settlement behavior and metamorphose into normal juvenile adults, which are not cemented to the substratum.[87] This behavior could perhaps be explained by the fact that barnacles express a GPCR that is almost 37% similar to the human α_2-adrenergic receptor.[97] In addition, micromolar solutions of many other adrenergic receptor ligands, such as medetomidine, clonidine, idozaxan and phentolamine are also known to inhibit barnacle cyprid settlement.[98,99]

It is important to discuss the observed settlement deterrence and how the cyprids are capable of sensing surface-tethered NA molecules. The fourth antennular segment of the barnacle cyprids possesses an array of sophisticated structures, the sole purpose of which is to examine the various aspects of the substratum prior to settlement.[100-102] Cyprids are known to respond favorably to surface-adsorbed molecules, as opposed to soluble ones.[103,104] While exploring the surface, the four subterminal setae and the two postaxial setae of the cyprid antennule are pressed against the substratum to possibly sense the surface adsorbed molecules.[100,102] Since the cyprids have such a sophisticated chemosensory apparatus, it can be speculated that when HBFP-PEG-tethered NA molecules stimulate these sensors, these stimuli are, in turn, perceived as unfavorable settlement cues by the cyprids causing deterrence of settling on such surfaces.[71] The observed reduction in larval settlement (Figure 3-9) further indicates that a dual-mode of

biofouling resistance was attainable through the addition of an active sensory deterrent to a passive anti-biofouling substrate.

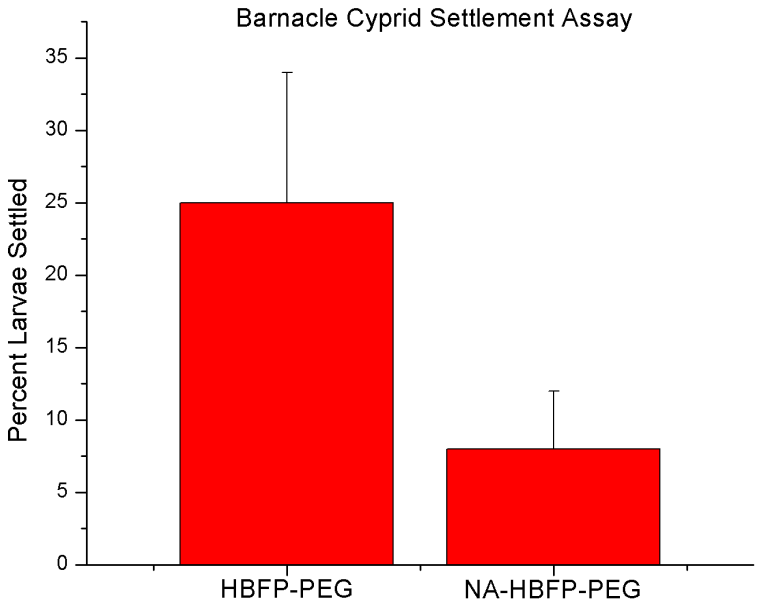

Figure 3-9: Cyprid settlement assay. Barnacle cyprid settlement on NA-HBFP-PEG was significantly reduced as compared to unmodified HBFP-PEG surfaces.

3.6 Conclusions

Dual-mode anti-biofouling surfaces were synthesized by modifying passively anti-biofouling HBFP-PEG with NA, and extensive characterization studies were performed. The co-deposition of HBFP and PEG afforded surfaces with nanoscopically-resolved topography and morphology that were passively anti-biofouling. Modification with the settlement deterrent NA afforded the dual-mode surface. The extent of substitution on the surface was determined by SIMS, which was quantified by the increase of m/z 26 and the reduction in the ratio of Br to F. The biological activity of the system was investigated through oyster hemocyte and barnacle cyprid assays. The activity of tethered-NA was confirmed by the observed cytoskeletal deterioration and apoptosis. The decoration of NA led to reduced settlement of barnacle cyprid larvae on NA-modified surfaces. The combination of passive and active modes of anti-biofouling increased the overall surface performance towards the inhibition of barnacle cyprid settlement. This study provides a new strategy for combining known fouling deterrent methodologies into a single coating and will be a guide for future formulations that optimize the effective application of these materials.

3.7 Acknowledgements

Financial support was provided by the Office of Naval Research under Grant Numbers N00014-10-1-0527 (KLW) and N00014-08-1-0157 (ASM & NVG), the National Science Foundation, Grant No. CHE-0750377 (EAS) and the W. T. Doherty-Welch Chair in Chemistry, Grant No. A-0001 (KLW). We also thank the Texas A&M University Laboratory for Biological Mass Spectrometry for small molecule mass spectral analysis. The anti-beta tubulin monoclonal antibody developed by M. Klymkowsky was obtained from the Developmental Studies Hybridoma Bank developed under the auspices of the NICHD and maintained by the University of Iowa, Department of Biology, Iowa City, IA 52242.

CHAPTER IV

MODEL DIELS-ALDER STUDIES FOR THE CREATION OF AMPHIPHILIC CROSSLINKED NETWORKS AS HEALABLE, ANTI-BIOFOULING COATINGS*

4.1 Original Publication Information

This chapter was originally published as a letter in *ACS Macro Letters*.

Collaborative contributions: C. Fidge conducted the small molecule and linear oligomer model studies; J. Raymond conducted protein adsorption assay and quantitative scratch healing analysis; S. Cauët conducted DLS experiments.

Modifications to the original document are cosmetic and used only to conform the format of this document or provide uniformity of enumeration. Due to this formatting, compounds may be labeled out of sequential order, but are consistent with the compound numbers in the original publication and do not detract from the coherence of the chapter. Contents found in the supporting information, which was originally a separate document, has been included in the chapter, and schemes and figures have been renumbered to conform to the style of this document.

4.2 Overview

Diels-Alder chemistry was used in the construction of amphiphilic crosslinked polymer networks comprised of furan-functionalized hyperbranched fluoropolymers and maleimide-functionalized linear poly(ethylene glycol)s, which were designed as anti-biofouling coatings capable of repair. Discrete molecules and a linear polymer analog were studied as model systems to understand the nature of the thermally-reversible [4+2] cycloaddition reaction involving a tetrafluorobenzylfuranyl ether unit, which was part of the structure for incorporation of the Diels-Alder functionalities into the composite network materials. Atomic force microscopy confirmed the complex, nanoscopically-resolved topography needed for anti-biofouling. Bright field and fluorescence imaging monitored healing at damage sites as well as the ability of the coatings to resist protein adsorption.

4.3 Introduction

It has become ever more desirable to prepare smart polymers using increasingly simpler methods. A popular topic to emerge in the last decade is that of reversible chemistry, which has allowed the development of repairable or „self-healing" materials. A few truly elegant examples in this field include the work of Jen *et al.*,[105] Leibler *et al.*,[106] White and Sottos *et al.*[107,108] and Wudl *et al.*[109] Many of these healable systems use, or share the characteristics of, „Click" chemistry,[110-114] which has received

significant attention as it involves reactions that have led to highly efficient and diverse production of complex materials.[112] Chemistries such as azide-alkyne Huisgen cycloaddition,[110] thiol-ene,[115-117] Michael addition[118] and *para*-fluoro-thiol click[119] are selective, orthogonal and quantitative. Diels-Alder cycloadditions[109] not only provide the qualities of „Click" reactions, but have the added benefit of being reversible and provide an opportunity for self-healing. The use of Diels-Alder (DA) chemistry in polymerizations is widespread and can be found in the synthesis of dendritic,[120-123] linear,[124-129] block,[130] graft,[131,132] star[133,134] and crosslinked polymers,[109,133,135-140] as has been reviewed recently.[141] DA chemistry is selective, yet versatile; the diene and dienophile are not restricted to one class of compounds. Indeed, some more exotic examples have been published under the title of Hetero-Diels-Alder (HDA), where for example, dithioesters have been coupled with butadiene and cyclopentadienyl moieties.[132,136] One of the most popular pairings for Diels-Alder is that of a maleimide-type dienophile with a furfuryl-based diene.[122,123,128,137-140]

Having demonstrated that hyperbranched fluorinated polymers (HBFP, **1**) crosslinked with poly(ethylene glycol) (PEG), HBFP-PEG, exhibit unique anti-biofouling capabilities yet lack adequate durability as coatings for application in the marine environment,[14] a current goal has been to incorporate a healable function for increased longevity. Based upon the thermally-triggered reversibility of the DA reaction and the chemical versatility of dienes and dieneophiles, we chose to install DA-reactive furan and maleimide functionalities onto HBFP (**2**) and PEG (**3**), respectively, to utilize DA chemistry as the mechanism for healable anti-biofouling coatings, **4**. However, because the chemical compositions and structures are difficult to characterize within crosslinked networks and unusual electronic effects were anticipated for the furfuryl group of the HBFP material, two model systems were designed by systematically deconstructing the HBFP and PEG components (Scheme 4-1) into A_2 (**5**) + B_2 (**3**) comonomers for linear polymer formation **6** (model reaction 2) and, further, into monofunctional small molecules, **7** and N-methylmaleimide, for coupling to a DA adduct **8** (model reaction 1). Studies were then performed to understand the reaction conditions to effect the reversible chemistry.

4.4 Experimental

4.4.1 Materials

N-methylmaleimide was purified by sublimation. Sodium hydride (60% dispersion) was washed with hexanes prior to use to remove protective mineral oil. 2,3,4,5,6-Pentafluorobenzyl bromide was obtained from Apollo Scientific Ltd. Bis-maleimide poly(ethylene glycol) M_n = 2000 Da (Bis-maleimide PEG B_2 monomer) was obtained from Rapp Polymere GmbH. Bovine serum albumin (66 kDa) AlexaFluor-488 conjugate was purchased from Invitrogen. All other reagents and solvents were obtained at the highest purity available from Sigma-Aldrich or VWR and used without further purification unless stated.

4.4.2 Characterization

^{1}H (300 MHz), ^{13}C (75 MHz) and ^{19}F (282 MHz) nuclear magnetic resonance (NMR) spectra were recorded using a Varian Inova 300 MHz spectrometer using $CDCl_3$ as the NMR solvent. ^{1}H and ^{13}C NMR spectra were analyzed using the solvent signal as an internal reference and ^{19}F NMR spectra were analyzed with CF_3COOH as an external standard. Gel permeation chromatography was performed on a Waters Chromatography, Inc. (Milford, MA), 1515 isocratic HPLC pump equipped with an inline degasser, a model PD2020 dual-angle (15° and 90°) light scattering detector (Precision Detectors,

Inc.), a model 2414 differential refractometer (Waters, Inc.), and four PL_{gel} polystyrene-*co*-divinylbenzene gel columns (Polymer Laboratories, Inc.) connected in series: 5 μm Guard (50 × 7.5 mm), 5 μm Mixed C (300 × 7.5 mm), 5 μm 10^4 (300 × 7.5 mm), and 5 μm 500 Å (300 × 7.5 mm) using the Breeze (version 3.30, Waters, Inc.) software. The instrument was operated at 35 °C with THF as the eluent (flow rate set to 1.00 mL/min). Polymer solutions were prepared at a known concentration (*ca*. 3 mg/mL) and an injection volume of 200 μL was used. Data collection was performed with Precision Acquire 32 Acquisition program (Precision Detectors, Inc.) and analyses were carried out using Discovery32 software (Precision Detectors, Inc.) with a system calibration curve generated from plotting molecular weight as a function of retention time for a series of broad polydispersity poly(styrene) standards. Differential scanning calorimetric (DSC) studies were performed on a Mettler-Toledo DSC822^e (Mettler-Toledo, Inc., Columbus, OH), with a heating rate of 10 ºC/min. The T_m was taken as the local minima upon the third heating scan. Measurements were analyzed using Mettler-Toledo Star software version 10.00c. IR spectra were obtained on a Shimadzu IR Prestige Attenuated Total Reflectance Fourier-transform Infrared Spectrometer (ATR-FTIR). Spectra were analyzed using IRsolution software package (Shimadzu). Dynamic light scattering (DLS) measurements were conducted using Delsa Nano C (Beckman Coulter, Inc., Fullerton, CA) equipped with a laser diode operating at 658 nm. Size measurements were made in water (n = 1.3329, η = 0.890 cP at 25 ± 1 °C). Scattered light was detected at 15° angle and analyzed using a log correlator over 10 runs each consisting of 70 accumulations for a 0.5 mL of sample in a glass size cell (0.9 mL

capacity). The samples in the glass size cell were filtered through a 0.45 μm nylon membrane and equilibrated at the desired temperature for 60 minutes before measurements were made. The photomultiplier aperture and the attenuator were automatically adjusted to obtain a photon counting rate of *ca.* 10 kcps. The calculation of the particle size distribution and distribution averages was performed using CONTIN particle size distribution analysis routines. The peak average of histograms from intensity, volume or number distributions out of 70 accumulations was reported as the average diameter of the particles. Atomic force microscopy was performed under ambient conditions in air. The AFM instrumentation consisted of a MFP-3D-BIO AFM (Asylum Research; Santa Barbara, CA) and standard silicon tips (type, OTESPA-70; L, 160 μm; normal spring constant, 50 N/m; resonance frequency, 246-282 kHz). High-resolution mass spectrometry (HRMS) was conducted on an Applied Biosystems PE SCIEX QSTAR, a walk-up service provided by the Texas A&M University Laboratory for Biological Mass Spectrometry, which is gratefully acknowledged. Fluorescence microscopy was conducted on an Olympus IX70 inverted microscope equipped with a mercury arc lamp and an Olympus DP72 digital camera. Images were collected through a 10× objective (Olympus UPlanFl n 10x/NA 0.30). Excitation and emission collection was achieved with the use of an Olympus U-MNIBA3 filter cube (excitation: 470-495 nm, emission: 510-550 nm). Wide field phase contrast imaging was performed in order to return to the same region of interest. All collection during fluorescence imaging was done with the same optics set and with the same collection time and CCD gain in order to maintain comparability from frame-to-frame.

4.4.3 Synthesis

Scheme 4-1. Synthesis of 1-(phenyloxymethyl)-2,3,4,5,6-pentafluorobenzene (**9**) as a precursor to the small molecule model diene.

1-(phenyloxymethyl)-2,3,4,5,6-pentafluorobenzene (9). To a 250 mL round bottom flask was added acetone (250 mL), which was deoxygenated by sparging with nitrogen for 10 min. Phenol (5.608 g, 59.60 mmol), potassium carbonate (8.236 g, 59.60 mmol) and 18-crown-6 (1.313 g, 4.960 mmol) were added and the solution was allowed to undergo reaction while stirring under nitrogen for an additional 30 min. 2,3,4,5,6-Pentafluorobenzyl bromide (12.96 g, 49.70 mmol) was added *via* syringe and the reaction was left to stir at room temperature under nitrogen for 169 h. After this time elapsed, ^{19}F NMR indicated less than ca. 10% substitution of the *para*-fluorine with near complete conversion of the benzylic bromide to give the desired product, **9**. The reaction mixture was concentrated *in vacuo* and purified by silica gel flash chromatography using 10% dichloromethane (DCM) in hexanes as the eluent which

afforded **9** in 78% yield (10.59 g). T_m: 79.3 °C. ^{1}H NMR: δ (ppm) 7.32 (m, 2H, *meta*-***H***), 7.00 (m, 3H, *ortho*-***H*** and *para*-***H***) and 5.13 (s, 2H, ArOC***H***$_2$). ^{13}C NMR: δ (ppm) 158.0 (1C, *ipso*-***C*** of Ar-O), 129.7 (2C, *meta*-***C*** of Ar-O), 121.9, (1C, *para*-***C*** of Ar-O), 114.9 (2C, *ortho*-***C*** of Ar-O), 147.4 (2C, *meta*-***C*** of -C_6F_5), 139.9, (1C, *para*-***C*** of -C_6F_5), 136.0 (2C, *ortho*-***C*** of -C_6F_5), 105.0 (1C, *ipso*-***C*** of -C_6F_5) and 57.4 (1C, ArO***C***H$_2$). ^{19}F NMR: δ (ppm) -142.3 (dd, 2F, J_A = 9 Hz, J_B = 13 Hz, *ortho*-***F***), -152.8 (t, 1F, ^3J = 21 Hz, *para*-***F***) and -161.7 (m, 2F, *meta*-***F***). IR ν (cm^{-1}): 3100-3000, 3000-2865, 2056, 1659, 1589, 1501, 1470, 1427, 1385, 1308, 1289, 1172, 1126, 1227 and 1053. HRMS m/z calculated for $C_{13}H_7F_5O$ [M + H]$^+$ 275.04 Da, found 275.0495 Da.

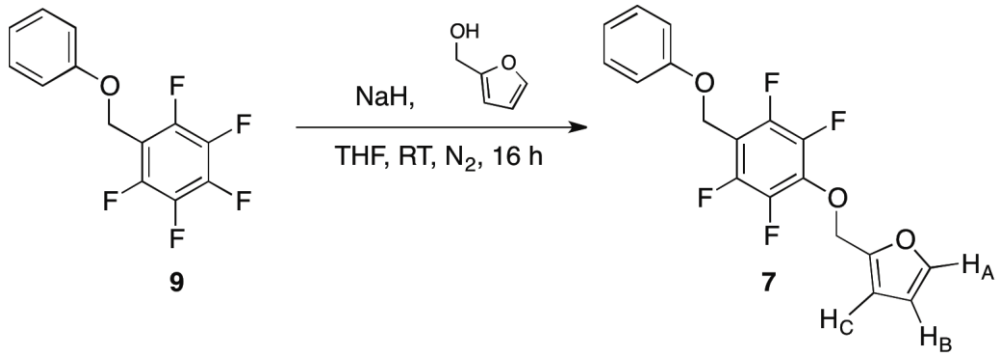

Scheme 4-2. Synthesis of 1-(phenyloxymethyl)-4-furfuryloxy-(2,3,5,6-tetrafluorobenzene) (**7**) as a small molecule model diene.

1-(phenyloxymethyl)-4-furfuryloxy-(2,3,5,6-tetrafluorobenzene) (7). To a 250 mL round bottom flask was added sodium hydride (1.823 g, 45.59 mmol) and dry THF (80 mL). Furfuryl alcohol (3.936 g, 40.12 mmol) was introduced *via* syringe into the solution and stirring was continued for 20 min under nitrogen, at which point **9** (5.0 g, 18 mmol) was added. The reaction was left to proceed while stirring under nitrogen for 16 h. The reaction mixture was then concentrated *in vacuo* and purified by silica gel flash chromatography using 30% DCM in hexanes as the eluent to afford **7** in 45% yield (2.867 g). T_m: 71.1 °C. ^{1}H NMR: δ (ppm) 7.45 (d, 1H, J = 2 Hz, $\boldsymbol{H_A}$), 7.32 (m, 2H, *meta*-***H***), 7.00 (m, 3H, *ortho*-***H*** and *para*-***H***), 6.44 (d, 1H, J = 1 Hz, $\boldsymbol{H_C}$), 6.36 (dd, 1H, J = 3 Hz and J = 2 Hz, $\boldsymbol{H_B}$), 5.21 (s, 2H, C_6F_4-OC$\boldsymbol{H}_2$) and 5.09 (s, 2H, C_6F_4-C$\boldsymbol{H}_2$O). ^{13}C NMR: δ (ppm) 158.2 (1C, ipso-***C*** of Ar-O), 148.3 (1C, HC=***C***(O)CH_2), 148.2 (2C, *ortho*-***C*** of C_6F_4 to $C_6F_4OCH_2$, 144.2 (1C, $\boldsymbol{C_A}$), 137.2 (2C, *meta*-***C*** of C_6F_4 to $C_6F_4OCH_2$), 129.7 (2C, *meta*-***C*** of Ar-O), 121.8 (1C, *para*-***C*** of Ar-O), 115.1 (2C, *ortho*-***C*** of Ar-O), 111.8 (1C, $\boldsymbol{C_B}$), 110.7 (1C, $\boldsymbol{C_C}$), 107.8 (1C, *ipso*-***C*** of $OCH_2C_6F_4$), 105.1 (1C, *ipso*-***C*** of $C_6F_4OCH_2$), 67.8 (1C, $C_6F_4O\boldsymbol{C}H_2$) and 57.7 (1C, ArO$\boldsymbol{C}H_2$). ^{19}F NMR: δ (ppm) -144.2 (m, 2F, *ortho*-***F*** to CH_2OAr) and -156.0 (m, 2F, *meta*-***F*** to CH_2OAr). IR ν (cm^{-1}): 3200-3100, 3085-3000, 3000-2910, 2910-2820, 2630, 2584, 2523, 2422, 2230, 2168, 1982, 1932, 1659, 1597, 1489, 1381, 1234, 1142, 1049.

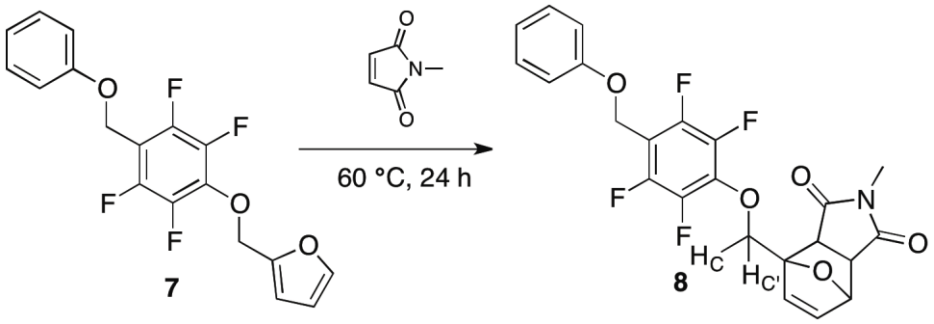

Scheme 4-3. Synthesis of 2-methyl-4-((2,3,5,6-tetrafluoro-4-(phenoxymethyl)phenoxy)methyl)-3a,4,7,7a-tetrahydro-1H-4,7-epoxyisoindole-1,3(2H)-dione (**8**) as the product of the Diels-Alder forward reaction.

2-methyl-4-((2,3,5,6-tetrafluoro-4-(phenoxymethyl)phenoxy)methyl)-3a,4,7,7a-tetrahydro-1H-4,7-epoxyisoindole-1,3(2H)-dione (8). To a conical vial was added **7** (0.101 g, 0.287 mmol) and *N*-methylmaleimide (0.321 g, 2.89 mmol). The vessel was sealed and the contents were heated at 60 °C for 24 h. ^{1}H NMR revealed approximately 60% conversion to **8**. The mixture was dissolved in DCM and eluted through a plug of silica gel to isolate one of the Diels-Alder (DA) adducts for analysis. ^{1}H NMR: δ (ppm) 7.32 (m, 2H, *meta*-***H***), 7.00 (m, 3H, *ortho*-***H*** and *para*-***H***), 6.66 (m, 2H, ***H***-C=C-***H***), 5.30 (s, 1H, O-bridgehead-C***H***), 5.09 (s, 2H, C_6F_4-C$\boldsymbol{H}_2$O), 4.92 (d, 1H, J = 12 Hz, $\boldsymbol{H}_{C'}$), 4.71 (d, 1H, J = 12 Hz, $\boldsymbol{H}_{C}$), 3.02 (m, 2H, bicyclo-C***H***) and 2.97 (s, 3H, C$\boldsymbol{H}_3$). ^{13}C NMR: δ (ppm) 175.75, 174.51, 158.21, 137.48, 136.96, 129.74, 121.81, 115.00, 109.40, 89.77, 81.40, 71.93, 57.70, 50.03, 49.04, 48.48 and 25.18. ^{19}F NMR: δ

(ppm) -143.8 (m, 2F, *ortho*-***F*** to CH_2OAr) and -156.2 (m, 2F, *meta*-***F*** to CH_2OAr). IR ν (cm^{-1}): 3120-3000, 3000-2870, 2870-2760, 1775, 1697, 1597, 1497, 1443, 1389, 1288, 1227, 1134 and 1026.

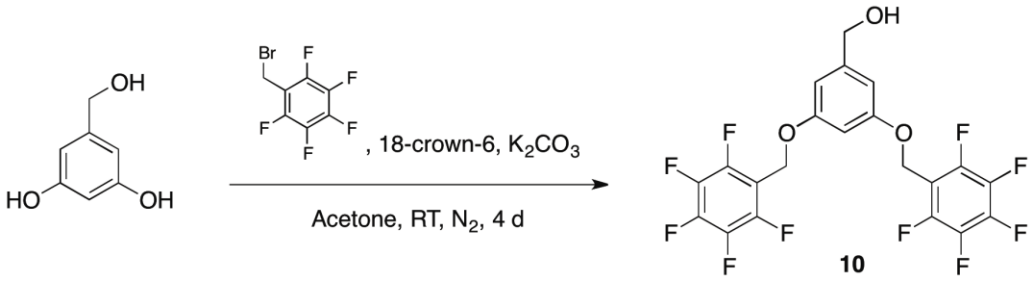

Scheme 4-4. Synthesis of 3,5-*bis*(2,3,4,5,6-pentafluorobenzyloxy) benzyl alcohol (**10**) as a precursor to the A_2 monomer for the linear condensation polymerization model reaction.

3,5-*bis*(2,3,4,5,6-pentafluorobenzyloxy) benzyl alcohol (10). To a 1 L round bottom flask was added 3,5-dihydroxybenzyl alcohol (14.36 g, 102.4 mmol), 18-crown-6 (2.706 g, 10.24 mmol), potassium carbonate (31.14 g, 22.54 mmol) and acetone (400 mL). The solution was deoxygenated with a stream of nitrogen for 30 min. 2,3,4,5,6-Pentafluorobenzyl bromide (58.82 g, 22.54 mmol) was added *via* syringe and the reaction and was left to proceed at room temperature under a blanket of nitrogen stirring vigorously for 4 d. The precipitate was filtered away and the filtrate was concentrated *in*

vacuo to afford an orange oil and the product was obtained by recrystallization from warm DCM and hexanes. The product was further purified by silica gel flash chromatography using DCM as the eluent, which afforded **10** in 74% yield (38.078 g). T_m: 100.2 °C. ^{1}H NMR: δ (ppm) 6.66 (d, 2H, J = 2 Hz, Ar***H***, *ortho* to -CH_2OH), 6.50 (t, 1H, J = 2 Hz, Ar***H***, *para* to -CH_2OH), 5.11 (s, 4H, $C_6F_5C\boldsymbol{H}_2$O-), 4.67 (d, 2H, J = 6 Hz, Ar$C\boldsymbol{H}_2$OH) and 1.72 (t, 1H, J = 6 Hz, -$CH_2O\boldsymbol{H}$). ^{13}C NMR: δ (ppm) 159.5 (2C, *ipso*-***C*** of Ar-$OCH_2C_6F_5$), 147.6 (4C, *meta*-***C*** of -C_6F_5), 143.6 (1C, *ipso*-***C*** of Ar-CH_2OH), 139.4, (2C, *para*-***C*** of -C_6F_5), 136.1 (4C, *ortho*-***C*** of -C_6F_5), 110.0 (2C, *ipso*-***C*** of -C_6F_5), 106.4 (2C, Ar***C***), 101.5 (1C, Ar***C***), 65.1 (1C, Ar***C***H_2OH) and 57.6 (2C, -O***C***$H_2C_6F_5$). ^{19}F NMR: δ (ppm) -143.11 (m, 4F, *ortho*-***F***), -153.3 (m, 2F, *para*-***F***), -162.3 (m, 4F, *meta*-***F***). IR: ν (cm^{-1}) 3500-3050, 3050-2870, 1659, 1597, 1497, 1458, 1427, 1056 and 1377 to 976. HRMS m/z calculated for $C_{23}H_{14}F_{10}O_4$ $[M + Cl]^+$ 535.50 Da, found 535.0206 Da.

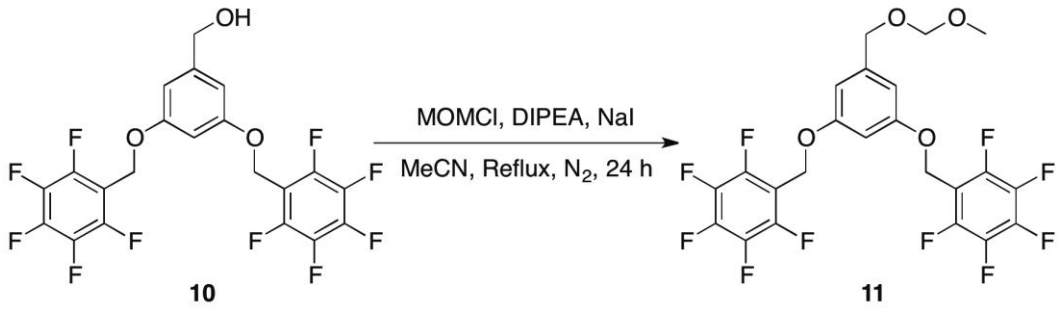

Scheme 4-5. Synthesis of 1,3-*bis*(2,3,4,5,6-pentafluorobenzyloxy)-5-((methoxymethoxy)methyl) benzene (**11**) as a precursor to the protected A_2 monomer in a model linear condensation copolymerization.

1,3-*bis*(2,3,4,5,6-pentafluorobenzyloxy)-5-((methoxymethoxy)methyl) benzene (11). To a 500 mL round bottom flask was added sodium iodide (11.98 g, 79.95 mmol) and acetonitrile (100 mL). Methoxymethyl chloride (MOMCl) (8.288 g, 102.9 mmol) was added and the solution was allowed to stir under nitrogen for 15 min. A separate solution was prepared from **10** (10.00 g, 19.99 mmol), diisopropylethylamine (DIPEA) (14.21 g, 109.9 mmol) and acetonitrile (20 mL), and was introduced *via* syringe into the stirring reaction mixture, which was left to proceed under nitrogen while being heated at reflux for 24 h. The reaction mixture was concentrated *in vacuo* and the crude product was extracted with hexanes. The product was obtained by silica gel flash chromatography using 30% hexanes in DCM as the eluent which afforded **11** in 75% yield (8.20 g). ^{1}H NMR: δ (ppm) 6.66 (d, 2H, J = 2 Hz, Ar***H***, *ortho* to CH_2OH), 6.51 (t,

1H, *J* = 2 Hz, Ar***H***, *para* to -CH_2OH), 5.11 (s, 4H, $C_6F_5C\boldsymbol{H}_2O$), 4.72 (s, 2H, $ArCH_2OC\boldsymbol{H}_2OCH_3$), 4.56 (s, 2H, $ArC\boldsymbol{H}_2OCH_2OCH_3$) and 3.43 (s, 3H, $OC\boldsymbol{H}_3$). ^{13}C NMR: δ (ppm) 159.3 (2C, *ipso*-***C*** of Ar-$OCH_2C_6F_5$), 147.5 (4C, *meta*-***C*** of -C_6F_5), 141.1 (1C, *ipso*-***C*** of Ar-CH_2OCH_2), 139.4 (2C, *para*-***C*** of -C_6F_5), 136.0 (4C, *ortho*-***C*** of -C_6F_5), 110.0 (2C, *ipso*-***C*** of -C_6F_5), 107.2 (2C, Ar***C***), 101.5 (1C, Ar***C***), 95.92 (1C, $ArCH_2O\boldsymbol{C}H_2OCH_3$), 68.8 (1C, $Ar\boldsymbol{C}H_2OCH_2OCH_3$), 57.5 (2C, -$O\boldsymbol{C}H_2C_6F_5$) and 55.6 (1C, $O\boldsymbol{C}H_3$). ^{19}F NMR: δ (ppm) -142.9 (m, 4F, *ortho*-***F***), -153.2 (m, 2F, *para*-***F***), -162.2 (m, 4F, *meta*-***F***). IR ν (cm^{-1}): 3060-2920, 2920-2850, 1659, 1597, 1504, 1450, 1435, 1377, 1350, 1312, 1288, 1150, 1057 and 1030. HRMS m/z calculated for $C_{23}H_{14}F_{10}O_4$ [M + Na]$^+$ 567.06 Da, found 567.0624 Da.

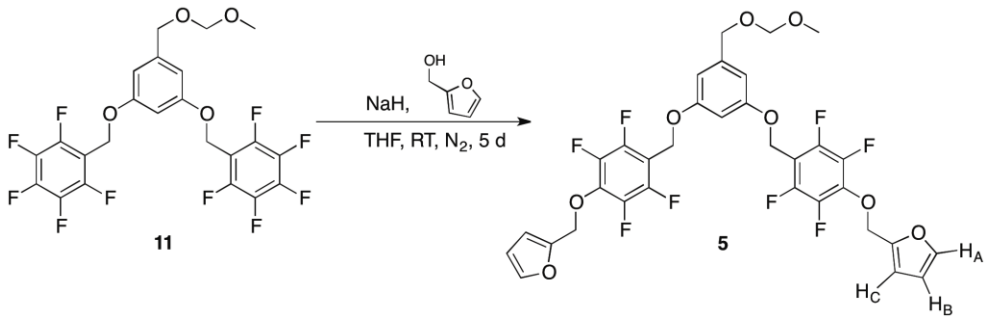

Scheme 4-6. Synthesis of *bis*(4-furfuryloxy-2,3,5,6-tetrafluorobenzyloxy)-5-((methoxymethoxy)methyl) benzene (**5**) as a protected A_2 monomer in a model linear condensation copolymerization.

Bis*(4-furfuryloxy-2,3,5,6-tetrafluorobenzyloxy)-5-((methoxymethoxy)methyl) benzene (5).** To a 100 mL round bottom flask suspended in an ice bath was added sodium hydride (0.2202 g, 9.168 mmol). A solution of furfuryl alcohol (0.7230 g, 8.083 mmol) in THF (50 mL) was added drop-wise to the flask. Then **11** (2.000 g, 3.674 mmol) was added and the solution was warmed to room temperature and allowed to stir under nitrogen for 5 d. The reaction mixture was concentrated *in vacuo* and the product was obtained by silica gel flash chromatography using DCM as the eluent which afforded **5** in 78% yield (2.00 g). T_m: 101.1 °C. ^{1}H NMR: δ (ppm) 7.45 (m, 2H, $\boldsymbol{H_A}$), 6.65 (m, 2H, ArH***, *ortho* to -CH_2OH), 6.52 (m, 1H, Ar***H*** *para* to -CH_2OH), 6.44 (m, 2H, $\boldsymbol{H_C}$), 6.35 (m, 2H, $\boldsymbol{H_B}$), 5.21 (s, 4H, $C_6F_4OC\boldsymbol{H}_2$), 5.07 (s, 4H, $C_6F_4C\boldsymbol{H}_2O$), 4.71 (s, 2H, $ArCH_2OC\boldsymbol{H}_2OCH_3$), 4.55 (s, 2H, $ArC\boldsymbol{H}_2OCH_2OCH_3$) and 3.42 (s, 3H, $OC\boldsymbol{H}_3$). ^{13}C NMR: δ (ppm) 159.4 (2C, *ipso*-***C*** of Ar-$OCH_2C_6F_4$), 149.0 (2C, $HC{=}\boldsymbol{C}(O)CH_2$), 147.4 (4C, *ortho*-***C*** of C_6F_4 to $C_6F_4OCH_2$), 144.1 (2C, $\boldsymbol{C_A}$), 142.9 (4C, *ortho*-***C'*** of C_6F_4 to $C_6F_4OCH_2$), 140.8 (1C, *ipso*-***C*** of Ar-CH_2OCH_2), 139.6 (4C, *meta*-***C*** of C_6F_4 to $C_6F_4OCH_2$), 137.1 (4C, *meta*-***C'*** of C_6F_4 to $C_6F_4OCH_2$), 111.8 (2C, $\boldsymbol{C_B}$), 110.6 (2C, $\boldsymbol{C_C}$), 108.9 (2C, *ipso*-***C*** of $OCH_2C_6F_4$), 107.1 (2C, Ar***C***), 105.0 (2C, *ipso*-***C*** of $C_6F_4OCH_2$), 101.4 (1C, Ar***C***), 95.8 (1C, $ArCH_2O\boldsymbol{C}H_2OCH_3$), 68.8 (1C, $Ar\boldsymbol{C}H_2OCH_2OCH_3$), 67.7 (2C, $C_6F_4O\boldsymbol{C}H_2$), 57.7 (2C, $O\boldsymbol{C}H_2C_6F_4$) and 55.5 (1C, $O\boldsymbol{C}H_3$). ^{19}F NMR: δ (ppm) -144.2 (m, 2F, *ortho*-***F*** to CH_2OAr), -155.9 (m, 2F, *meta*-***F*** to CH_2OAr). IR ν (cm^{-1}): 3085-2880, 2880-2800, 1655, 1589, 1493, 1466, 1423, 1373, 1319, 1296, 1261, 1231, 1138, 1111 and 1038. HRMS m/z calculated for $C_{33}H_{24}F_8O_8$ $[M + Li]^+$ 707.47 Da, found 707.1503 Da.

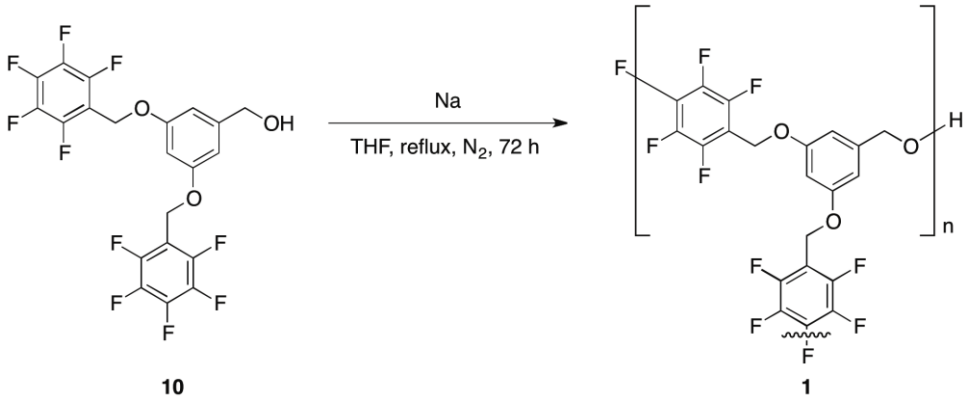

Scheme 4-7. Synthesis of hyperbranched fluoropolymer (**1**) as the low surface energy, crosslinkable component in anti-biofouling coatings.

Hyperbranched fluoropolymer (1). The polymer was synthesized using previously reported methods[40] to obtain **1**. M_w^{GPC} = 16500 Da, M_n^{GPC} = 8400 Da, M_w/M_n = 1.96.

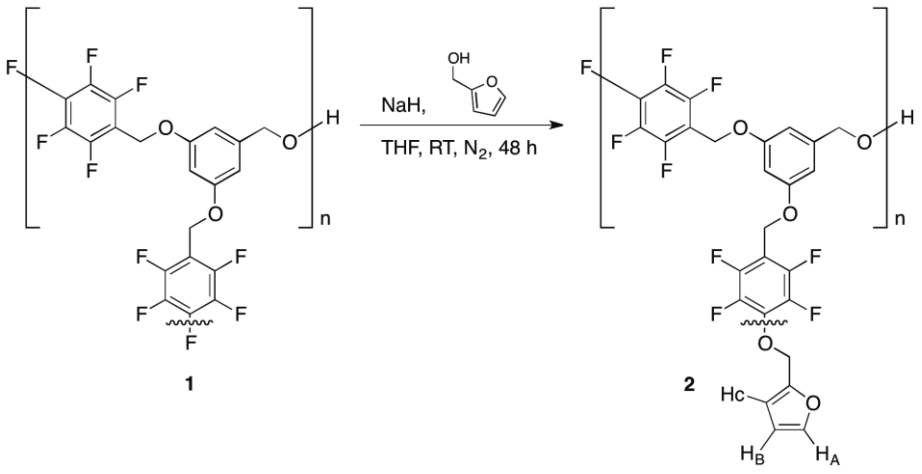

Scheme 4-8. Synthesis of hyperbranched fluoropolymer bearing pendant dienes (**2**) that act as reversibly-crosslinked moieties in a healable anti-biofouling coating.

Furfuryl-modified hyperbranched fluoropolymer (2). To a flame dried 25 mL round bottom flask was added **1** (400 mg, 0.05 mmol), sodium hydride (0.048 g, 2.0 mmol) and dry THF (10 mL). Furfuryl alcohol (0.196 mg, 2.00 mmol) was added to the flask and the solution was allowed to stir under nitrogen at room temperature. ^{19}F NMR revealed approx. 70% conversion of the *para*-fluorine sites after 24 h and nearly quantitative substitution after 48 h. The reaction mixture was filtered through a celite plug, concentrated and precipitated into cold hexanes. GPC analysis of **2** in comparison to **1** revealed similar molecular weight profiles (Figure 4-1), indicating that the free OH in **1** was not deprotonated and substituting another polymer *para*-F, demonstrating that there is no need for an intermediate protection step. M_w^{GPC} = 16500 Da, M_n^{GPC} = 8400

Da, M_w/M_n = 1.96. ^{1}H NMR: δ (ppm). ^{19}F NMR: δ (ppm). IR ν (cm^{-1}): 7.45 (br s, ***H*$_A$**), 7.25 (br s, ***H*$_A$**), 6.65 (br m, 2H, Ar***H***), 6.52 (br m, 1H, Ar***H***), 6.38 (br m, 1 H, ***H*$_C$**), 6.25 (br m, 1H, ***H*$_B$**), 5.25-4.85 (br m, 8H, OC***H***$_2$-backbone) and 1.72 (br s, 1H, ArCH$_2$O***H***). ^{19}F NMR: δ (ppm) -144.0 (br m, 2F, *ortho*-***F*** to $C_4F_4CH_2O$) and -156.0 (br m, 2F, *meta*-***F*** to $C_4F_4CH_2O$). IR ν (cm^{-1}): 3600-3100, 3100-3000, 3000-2840, 1589, 1480, 1320, 1291, 1226, 1144, 1057 and 989.

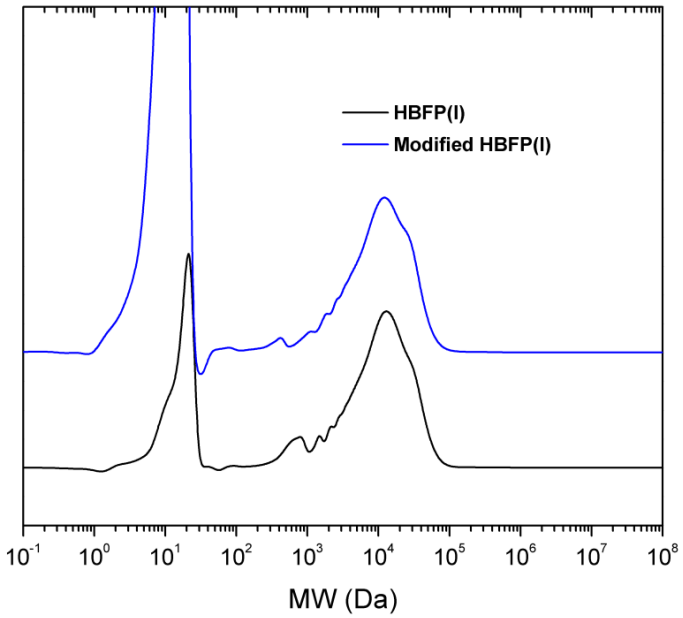

Figure 4-1. Molecular weight distributions of HBFP (**1**) before and after the substitution of *para*-Fs with furfuryloxy groups to afford **2**.

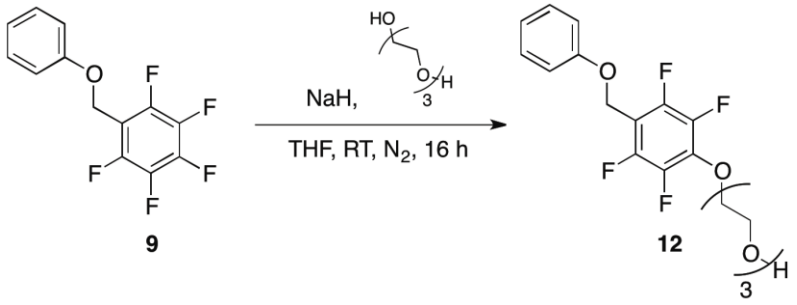

Scheme 4-9. Synthesis of 1-(phenyloxymethyl)-4[tri(ethylene glycol)yl]-2,3,5,6-tetrafluorobenzene (**12**) as a precursor to the small molecule model diene with a larger spacer.

1-(phenyloxymethyl)-4-[tri(ethylene glycol)yl]-2,3,5,6-tetrafluorobenzene (12). To a 500 mL two-neck round bottom flask was added sodium hydride (0.553 g, 13.8 mmol, 60% dispersion in mineral oil) and THF (200 mL) and the vessel lowered into an ice bath. Tri(ethylene glycol) (4.6 mL, 35 mmol) was introduced *via* syringe into the solution and stirring was continued for 20 min under nitrogen, at which point **9** (3.16 g, 11.5 mmol) was added. The reaction was left to proceed at room temperature while stirring under nitrogen for 16 h. The reaction mixture was then concentrated *in vacuo*, diluted in DCM, washed against water (4 x 100 mL) and dried over anhydrous $MgSO_4$. The crude product was obtained after being concentrated *in vacuo* and further purified by silica gel flash chromatography using 20% MeOH in DCM as the eluent to afford **12** in 84% yield (3.90 g). ^{1}H NMR: δ (ppm) 7.32 (m, 2H, *meta-**H***), 7.00 (m, 3H, *ortho-**H***

and *para*-***H***), 5.13 (s, 2H, ArOC***H***$_2$), 4.41 (t, 2H, *J* = 6 Hz, TFS-O-C***H***$_2$-R), 3.85 (m, 2H, TFS-O-CH$_2$-C***H***$_2$-R), 3.71 (m, 4H, R-C***H***$_2$-O-C***H***$_2$-C***H***$_2$-O) and 3.60 (m, 2H, R-C***H***$_2$-OH). ^{13}C NMR: δ (ppm) 158.2 (1C, *ipso*-***C*** of Ar-O), 147.6 (1C, *ipso*-***C*** of CH$_2$O-C$_6$F$_4$), 144.6 and 142.8 (2C, *ortho*-***C*** to OCH$_2$-C$_6$F$_4$), 139.5 and 139.3 (2C, *ortho*-***C*** to C$_6$F$_4$-OCH$_2$), 129.7 (2C, *meta*-***C*** of Ar-O), 121.9, (1C, *para*-***C*** of Ar-O), 114.9 (2C, *ortho*-***C*** of Ar-O), 108.7 (1C, *ipso*-**C** of OCH$_2$-C$_6$F$_4$), 74.2 (1C, C$_6$F$_4$-O***C***H$_2$-CH$_2$), 72.6 (1C, C$_6$F$_4$-OCH$_2$-***C***H$_2$), 70.9 to 70.2 (3C, O-***C***H$_2$-***C***H$_2$-O-***C***H$_2$-CH$_2$-OH), 61.8 (1C, ***C***H$_2$-OH) and 57.6 (1C, ArO-***C***H$_2$). ^{19}F NMR: δ (ppm) -144.2 (m, 2F, *ortho*-***F*** to CH$_2$OAr) and -156.8 (m, 2F, *meta*-***F*** to CH$_2$OAr). IR: ν (cm^{-1}) 3600-3200, 3200-3100, 3000-2865, 2056, 1496, 1381, 1289, 1227, 119, 1049, 941, 833, 756, 694, and 640. HRMS m/z calculated for C$_{19}$H$_{20}$F$_4$O$_5$ [M + Na]$^+$ 427.11 Da, found 427.1145 Da.

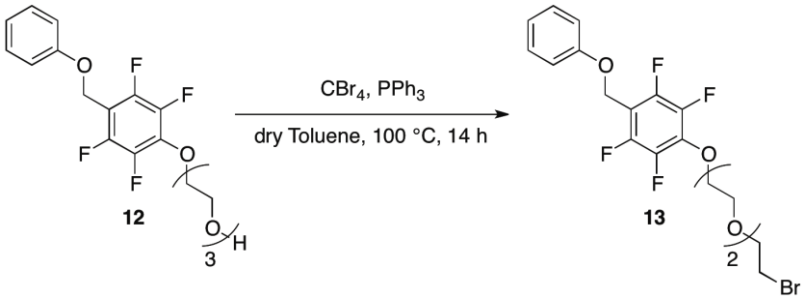

Scheme 4-10. Synthesis of 1-(phenyloxymethyl)-4-[di(ethylene glycol)-2‟-bromoethyl]-2,3,5,6-tetrafluorobenzene (**13**) as a precursor to the small molecule model diene with a larger spacer.

1-(phenyloxymethyl)-4-[di(ethylene glycol)-2'-bromoethyl]-2,3,5,6-tetrafluorobenzene (13). To a flame-dried, three-neck 100 mL round bottom flask was added **12** (2.49 g, 6.16 mmol) and dry toluene (50 mL). Triphenylphosphine was recrystallized from IPA (1.78 g, 6.79 mmol) and added as a solution in dry toluene *via* syringe, and the mixture was allowed to stir for an additional 10 min. Carbon tetrabromide (2.67 g, 8.05 mmol) was added as a dilute solution in dry toluene drop-wise to the reaction mixture, which was then allowed to proceed at 100 °C under nitrogen atmosphere. Following the completion of the transformation, the reaction mixture was concentrated, diluted in DCM and washed against water (4 x 100 mL) and then dried over anhydrous $MgSO_4$. The crude product was obtained after being concentrated *in vacuo* and further purified by silica gel flash chromatography using 50% ethyl acetate in hexanes as the eluent to afford **13** in 66% yield (1.72 g). ^{1}H NMR: δ (ppm) 7.32 (m, 2H, *meta*-***H***), 7.00 (m, 3H, *ortho*-***H*** and *para*-***H***), 5.11 (s, 2H, ArOC***H***$_2$), 4.41 (t, 2H, J = 6 Hz, TFS-O-C***H***$_2$-R), 3.85 (m, 2H, TFS-O-CH$_2$-C***H***$_2$-R), 3.80 (t, 2H, J = 6 Hz, O-C***H***$_2$-CH$_2$-Br), 3.69 (m, 4H, O-C***H***$_2$-C***H***$_2$-O) and 3.46 (t, 2H, J = 6 Hz, R-C***H***$_2$-Br). ^{13}C NMR: δ (ppm) 158.1 (1C, *ipso*-***C*** of Ar-O), 147.6 (1C, *ipso*-***C*** of CH$_2$O-C$_6$F$_4$), 144.2 (2C, *ortho*-***C*** to OCH$_2$-C$_6$F$_4$), 139.6 (2C, *ortho*-***C*** to C$_6$F$_4$-OCH$_2$), 129.8 (2C, *meta*-***C*** of Ar-O), 121.6, (1C, *para*-***C*** of Ar-O), 115.0 (2C, *ortho*-***C*** of Ar-O), 108.7 (1C, *ipso*-**C** of OCH$_2$-C$_6$F$_4$), 74.3 (1C, C$_6$F$_4$-O***C***H$_2$-CH$_2$), 71.3 (1C, C$_6$F$_4$-OCH$_2$-***C***H$_2$), 70.9 to 70.3 (3C, O-***C***H$_2$-***C***H$_2$-O-***C***H$_2$-CH$_2$-OH), 57.6 (1C, ArO-***C***H$_2$) and 30.5 (1C, ***C***H$_2$-Br). ^{19}F NMR: δ (ppm) -144.2 (m, 2F, *ortho*-***F*** to CH$_2$OAr) and 156.7 (m, 2F, *meta*-***F*** to CH$_2$OAr). IR ν

(cm^{-1}): 3100-3000, 3000-2850, 1496, 1381, 1288, 1227, 1118, 1034, 941, 833, 756 and 687. HRMS m/z calculated for $C_{19}H_{19}BrF_4O_4$ $[M + H]^+$ 467.04 Da, found 467.0481 Da.

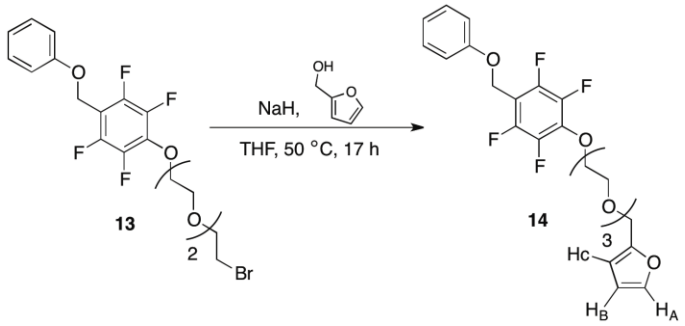

Scheme 4-11. Synthesis of 1-(phenyloxymethyl)-4-[di(ethylene glycol)-2‟-furfurylethyl]-2,3,5,6-tetrafluorobenzene (**14**) as a small molecule model diene with a larger spacer.

1-(phenyloxymethyl)-4-[di(ethylene glycol)-2'-furfurylethyl]-2,3,5,6-tetrafluorobenzene (14). To a flame-dried, three-neck 100 mL round bottom flask was added sodium hydride (58.9 mg, 1.47 mmol, 60% dispersion in mineral oil) and THF (30 mL) and the vessel lowered into an ice bath. Furfuryl alcohol (0.210 g, 2.14 mmol) was introduced *via* syringe into the solution and stirring was continued for 20 min under nitrogen, at which point **13** (0.502 g, 1.07 mmol) was added. The reaction was left to proceed at 50 °C while stirring under nitrogen for 17 h, while monitoring the reaction by ^{1}H NMR for the disappearance of the R‟-C***H***$_2$-Br resonance. The reaction mixture was

then concentrated *in vacuo*, diluted in DCM, washed against water (4 x 150 mL) and dried over anhydrous $MgSO_4$. The crude product was obtained after being concentrated *in vacuo* and further purified by silica gel flash chromatography using 50% ethyl acetate in hexanes as the eluent to afford **14** in 36% yield (187 mg). ^{1}H NMR: δ (ppm) 7.40 (m, 1H, $\boldsymbol{H_A}$), 7.30 (m, 2H, *meta*-***H***), 6.00 (m, 3H, *ortho*-***H*** and *para*-***H***), 6.35 to 6.32 (m, 2H, $\boldsymbol{H_B}$ and $\boldsymbol{H_C}$), 5.07 (br m, 4H, ArOC$\boldsymbol{H}_2$ and O-C$\boldsymbol{H}_2$-Furfuryl), 4.33 (m, 2H, TFS-O-C$\boldsymbol{H}_2$-R), and 3.82 to 3.62 (m, 10H, TrEG C$\boldsymbol{H}_2$). ^{13}C NMR: δ (ppm) 165.0, 158.2, 147.6, 144.6, 143.7, 142.8, 139.5 and 139.3, 129.6, 121.5, 115.0, 110.6, 110.4, 109.5 73.8, 70.9, 70.7, 70.3 69.4, 68.2, 67.5, and 65.2. ^{19}F NMR: δ (ppm) -144.2 (m, 2F, *ortho*-***F*** to CH_2OAr) and 156.7 (m, 2F, *meta*-***F*** to CH_2OAr). IR ν (cm^{-1}): 3100-3000, 3000-2865, 1600, 1481, 1358, 1288, 1226, 1119, 1049, 980, 833, 748, 694 and 602. HRMS m/z calculated for $C_{24}H_{24}F_4O_6$ $[M + H]^+$ 485.15 Da, found 485.1575 Da (ionizes poorly).

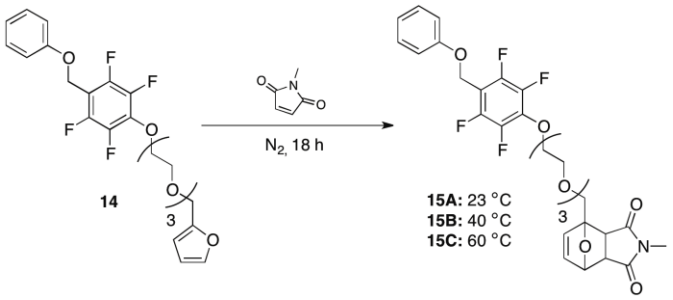

Scheme 4-12. Investigation into the ability of the small molecule model diene with a larger spacer (**14**) to perform a Diels-Alder reaction with N-methylmaleimide, as a function of temperature.

Diels-Alder reaction of the small molecule model diene with a larger spacer (15). To three separate conical round bottom flasks was added **14** (25 mg, 5.2 mmol) and *N*-methylmaleimide (5.7 mg, 5.2 mmol). The vessels were sealed under nitrogen atmosphere and allowed to react in bulk for 18 h at 23 °C (**15A**), 40 °C (**15B**) and 60 °C (**15C**), respectively. Each reaction mixture was diluted in $CDCl_3$ and analyzed by ^1H NMR spectroscopy, which revealed approximately 30% conversion to the Diels-Alder product for all three reactions, **15A**, **15B** and **15C**.

4.4.4 Dynamic Light Scattering

Procedure *i*: Preparation of nano-aggregates *via* direct solubilization in water. In a round bottom flask equipped with a magnetic stir bar, linear block copolymer (5.4 mg) was stirred in water (16.2051 g) for 2 h. Five drops of 0.01 M sodium hydroxide solution were added to complete solubilization and the solution was allowed to stir for an additional 2 h. The solution was then dialyzed against nanopure water (dialysis tubing MWCO 7000-8000 Da) for 3 d to a final concentration of 0.33 mg/mL. The resulting nano-aggregate solution was analyzed by DLS. Hydrodynamic diameter D_h (intensity) = 219 ± 173 nm; D_h (volume) = 58 ± 35 nm; D_h (number) = 40 ± 11 nm.

Procedure *ii*: Preparation of nano-aggregates *via* addition of water in THF/DMF. In a round bottom flask equipped with a magnetic stir bar, linear block copolymer (6.9 mg) was dissolved in THF/DMF (99.5:0.5 w/w). Water (4 mL) was

added drop-wise at a rate of 8 mL/h and the resulting solution was dialyzed against nanopure water for 3 d (dialysis tubing MWCO 7000-8000 Da) to a final concentration of 0.30 mg/mL. The resulting nano-aggregate solution was analyzed by DLS. Hydrodynamic diameter D_h (intensity) = 203 ± 118 nm; D_h (volume) = 96 ± 45 nm; D_h (number) = 70 ± 19 nm.

4.4.5 Adsorption of Biomacromolecules

Bovine serum albumin conjugated to AlexaFluor-488 (BSA) was dissolved in phosphate buffered saline (PBS) solution (pH 7.1) to a concentration of 0.1 mg/mL and stored in the dark. The surface of **4** was incubated in fresh PBS buffer for 10 min and dried *via* filtered nitrogen gas. Nine regions on the surface were imaged by wide field fluorescence microscopy to generate a baseline of auto-fluorescence detectable from the HBFP regions of the coating. Then, **4** was placed in a dark humid chamber and 200 μL of the BSA solution was deposited on the surface of **4** for 10 min. The BSA solution was removed and the sampled was dried again in the dark. The same nine regions were again imaged by wide field fluorescence microscopy. This was done with excitation and collection conditions identical to the post-PBS treated coating. All pixels from each image were converted into intensity histograms and compiled and this process was conducted for both the PBS-treated film and the film after BSA treatment. Change in emission intensity was then attributed to BSA uptake on the film surface. This experiment was also repeated for a known anti-biofouling material[35] with a similar

chemical composition. The film selected for comparison is a covalently cross-linked network of HBFP-PEG (55% by weight HBFP) and has been characterized in full elsewhere. [35] This comparison was done in order to show that the addition of reversible Diels-Alder chemistry to an HBFP-PEG matrix does not significantly reduce the resistance of the film surface to protein binding.

The histograms for the relative change in fluorescence of both samples, before and after BSA exposure, are presented (Figure 4-2). The change in the median value of the emission intensity can be seen to have approximately equal magnitudes (3.9 in **4** as compared to 3.5 in the HBFP-PEG standard). Representative fluorescence images before and after BSA exposure are also provided for **4** (Figure 4-3) and the standard (Figure 4-4). Note that the features with increased emission intensity after BSA exposure are also the surface features that initially showed the highest intensity of auto-fluorescence. This trend is indicative of a preferential BSA adsorption at regions extremely rich in HBFP, the auto-fluorescing species. Taken that **4** has ~20% more HBFP by weight than the standard, and given that the majority of observed BSA emission was from HBFP rich regions, it is reasonable that BSA binding is ~15% greater for **4**. Taken together, these results suggest no significant change in anti-biofouling character with the inclusion of the reversible Diels-Alder chemistry.

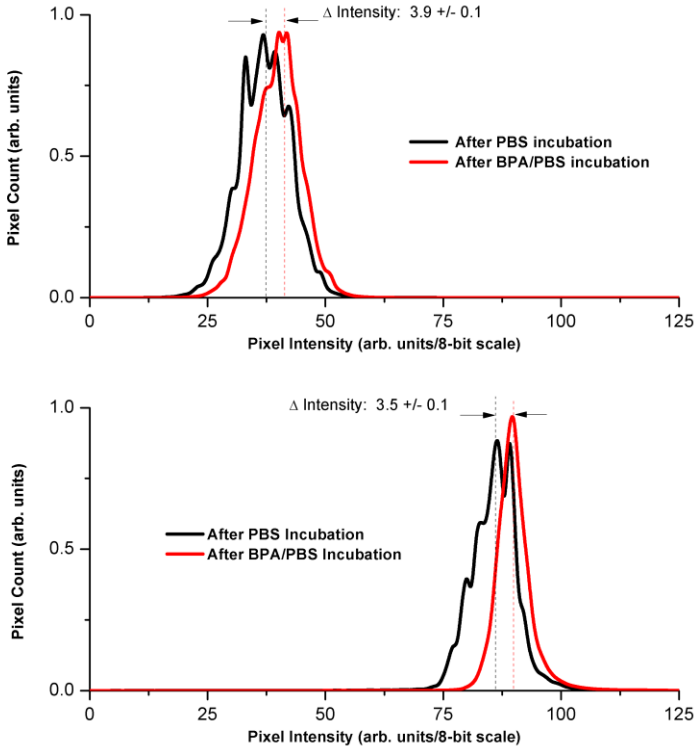

Figure 4-2. Change in fluorescence intensity profile for **4** (top) and for the HBFP-PEG anti-biofouling standard (bottom).

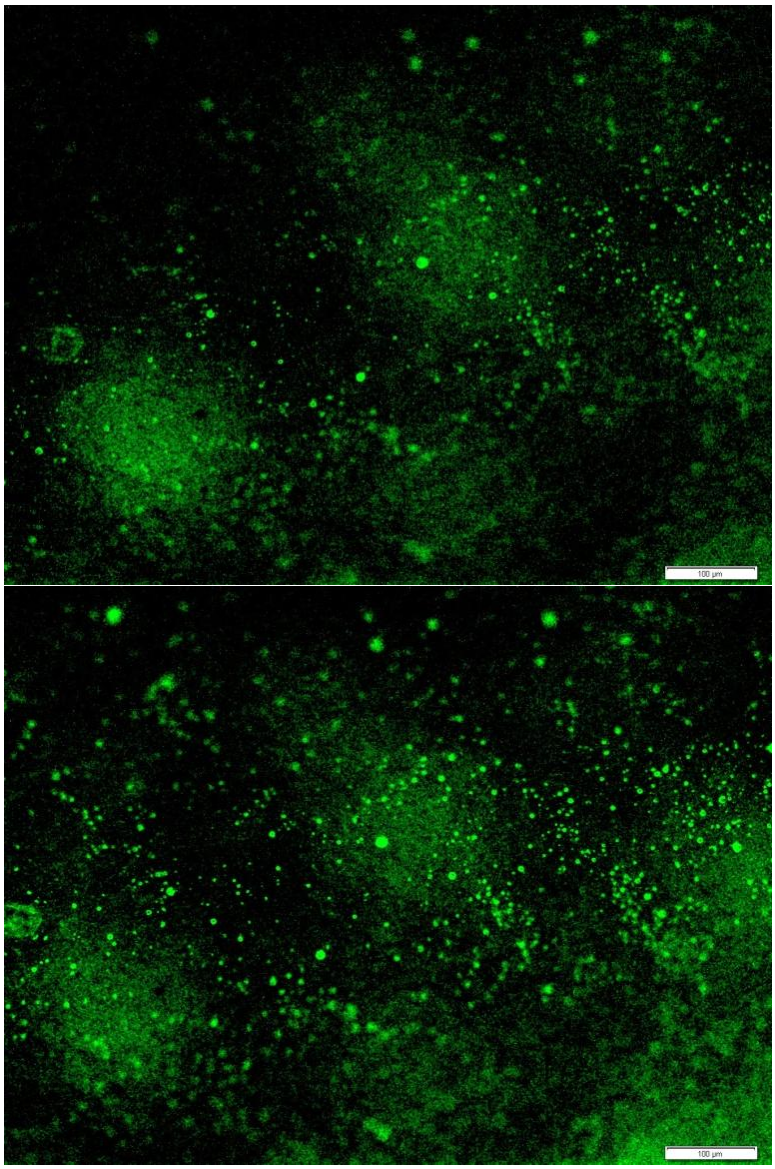

Figure 4-3. Representative images of **4** before (top) and after (bottom) BSA incubation. The scale bars are 100 μm.

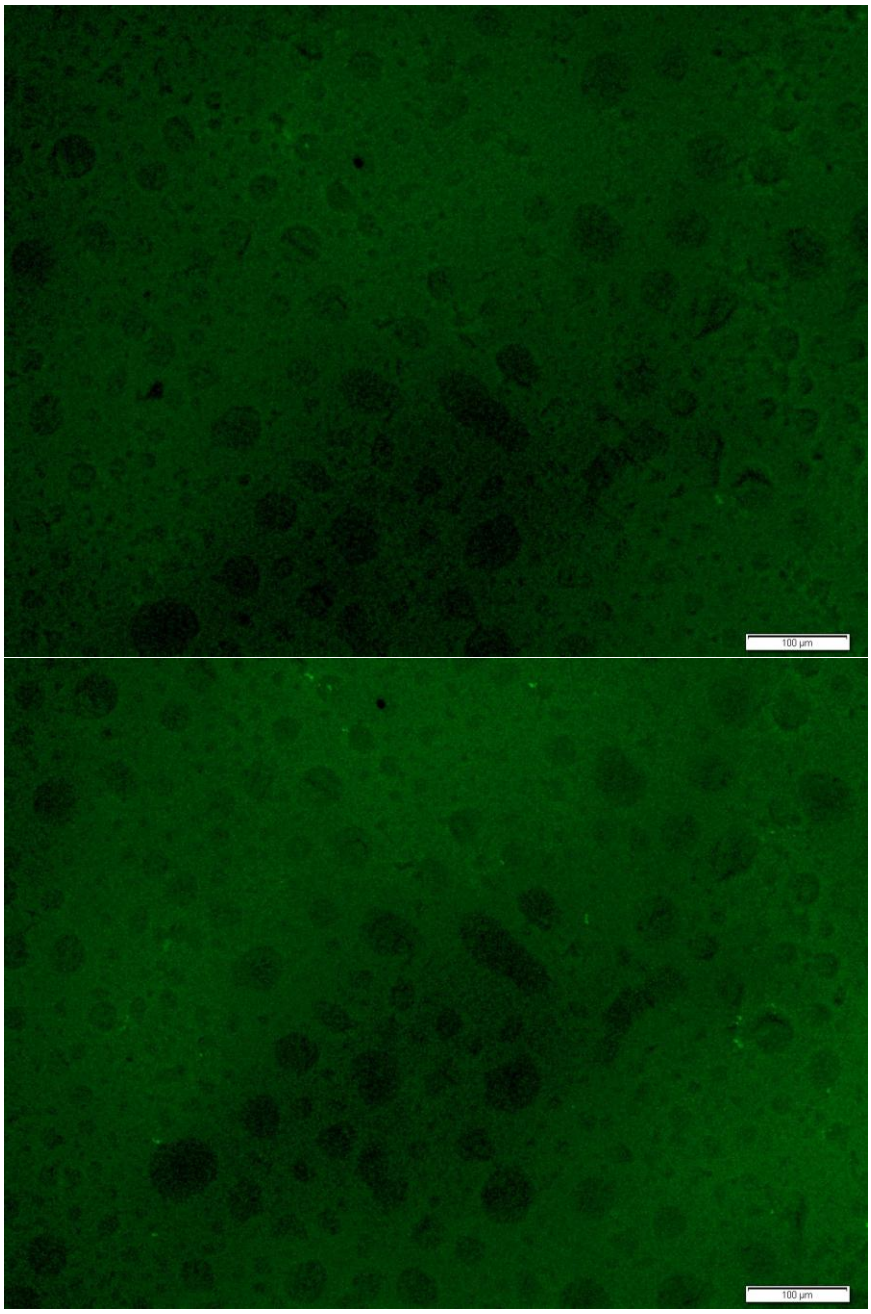

Figure 4-4. Representative images of the HBFP-PEG standard before (top) and after (bottom) BSA incubation. The scale bars are 100 µm.

4.4.5 Quantification of Healing from Bright-field Optical Microscopy

In order to observe the surface healing over time, an Olympus IX70 inverted microscope was employed in bright-field mode at 4× magnification. Intensity histograms were generated collecting images under the same exposure conditions of two different damaged regions on the surface of the coating. The damage inflicted was in the form of deep cuts and light abrasions. The initially damaged sites were observed to be much darker than the surrounding area of the surface. This can be readily understood as the damaged areas containing regions of inhomogeneity with domain sizes larger than the diffraction limit while the bulk film has nanoscale disorder far below the diffraction limit. The region of the surface inflicted with deep cuts was imaged after 0, 0.5, 1.5, 3.0 and 24 h incubation at 60 °C that promoted the regeneration of crosslinks. An overlay of histograms of count *vs.* pixel intensity was generated (Figure 4-5). The collection regime was selected such that the intensities of interest are far from the intensity of the background pixels. Figure 4-6 is a magnification of the intensities of interest from Figure 4-5 and showed that the counts associated with the damaged features decreased and became brighter over time, with no notable change after 3 h. Figure 4-6 also provides an inset of a masked bright field timeline where all pixels containing intensities of 50 or less are given in green and background is presented as red. Histograms for the region damaged by light abrasions was generated by the same method and reported (Figure 4-7). It can be seen that no meaningful change in intensity occurs after 30 min, which is reasonable given the difference in the relative amount of damage between a

deep cut and a scratch. While not implicitly providing the degree of healing after incubation, it is clear that transitions from a damaged state with microscale inhomogeneity to a state with disorder similar to the undamaged film was occurring. This process occurred within approximately 3 h of incubation for repair of deep film damage and only 30 min of incubation for repair of shallow film damage.

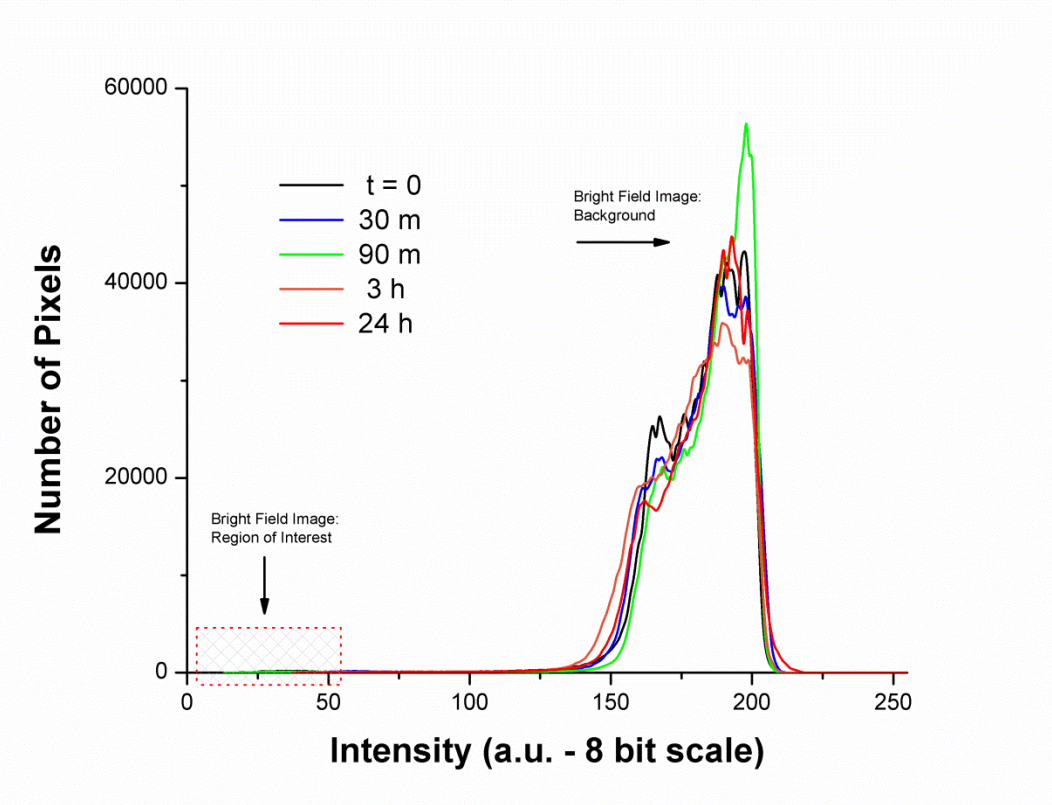

Figure 4-5. Time lapse histograms of the deep cut regions during heating at 60 °C.

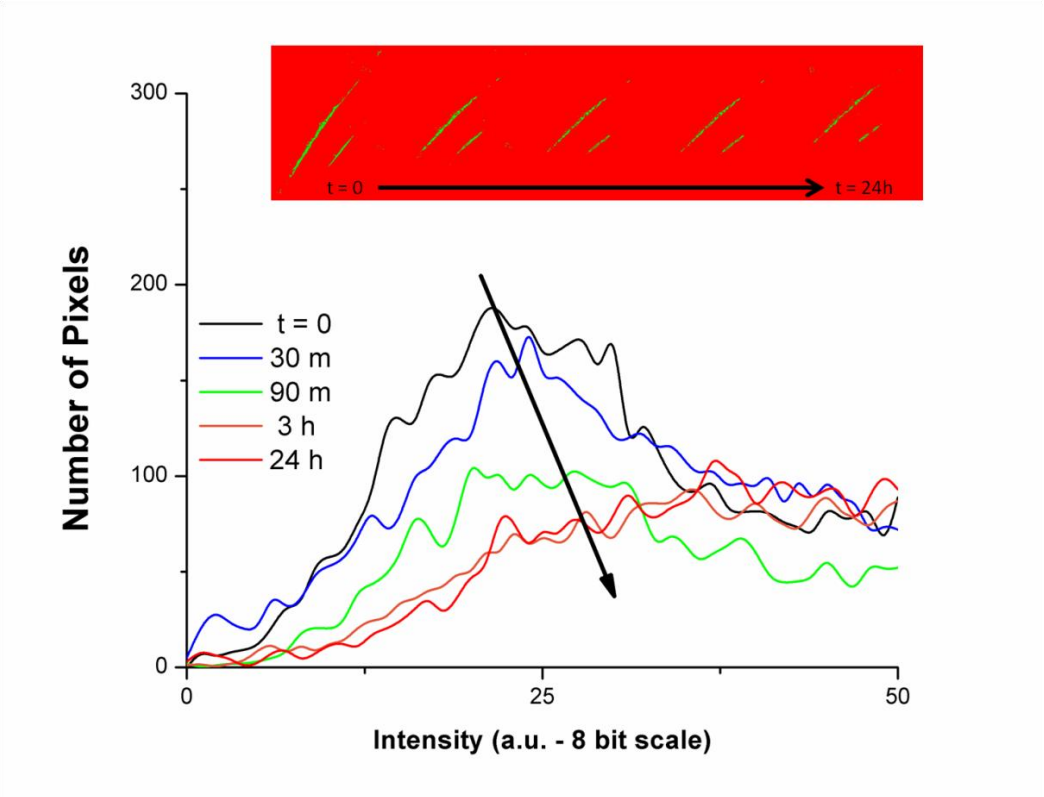

Figure 4-6. Magnified intensities of interest for the time lapse histograms of the deep cut regions during heating at 60 °C. Top inset: masked time lapse images of the damaged film.

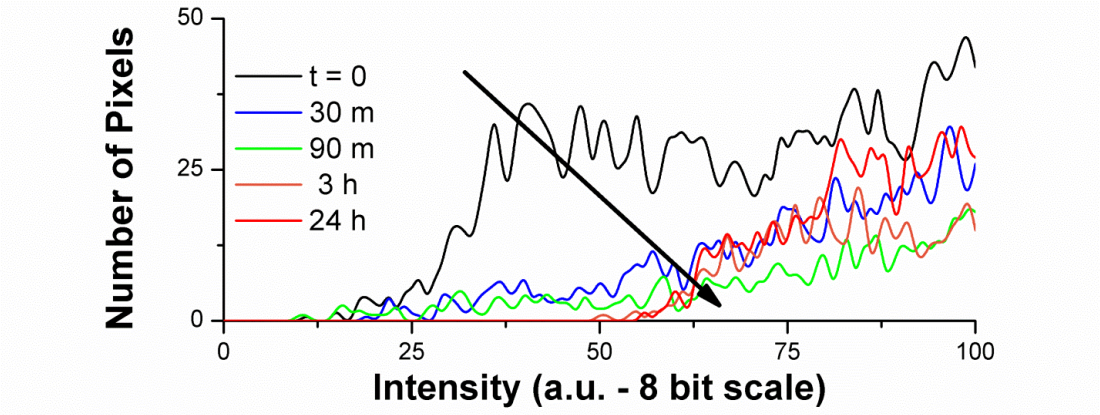

Figure 4-7. Intensities of interest for the time lapse histograms of the lightly scratched regions during heating at 60 °C.

4.5 Results and Discussion

The first study involved small molecule reactions of *N*-methylmaleimide with a diene, **7**, that was built to model structural elements of the furan-functionalized HBFP, **2** (Scheme 4-13, right, and Figure 4-8). The furan-based diene was connected to a tetrafluorobenzylphenyl ether to approximate the electron-withdrawing characteristics that would be present in **2**. Reaction of 2,3,4,5,6-pentafluorobenzyl bromide with phenol in the presence of potassium carbonate and 18-crown-6 yielded **9**,[40] followed by nucleophilic aromatic substitution of the *para*-fluorine by reaction with furfuryl alcohol and sodium hydride afforded 1-benzyloxy-4-furfuryloxy-2,3,5,6-tetrafluoro-benzene, **7**, in 35% yield over the two synthetic steps. Analysis showed that while *N*-

methylmaleimide would undergo reaction with unmodified furfuryl alcohol in DCM under ambient conditions, no reaction was observed for *N*-methylmaleimide and **7** under ambient conditions, with or without solvent. The rapid reaction of maleimide with furfuryl derivatives is well established, suggesting in this case that the substituent had contributed towards decreased diene reactivity. A tri(ethylene glycol) spacer was used to place the diene far from the fluoroaromatic group, therefore as a model study during peer-review of this manuscript, which restored the furfuryl unit‟s DA reactivity with N-methylmaleimide.

Despite the reduced activity of the DA moieties, reversible bond formation/cleavage was achievable through alteration of the experimental conditions. By heating the reaction mixture to 60 °C in bulk, it was found that the reaction could be driven to achieve 65% conversion of **7** to **8** in 24 h. The reaction temperature could not be raised any further, due to the possibility of triggering the retro-Diels-Alder reaction. In order to demonstrate reversibility, the crude product **8** was heated at 90 °C for 5 h to return to **7**, analyzed, and then subsequently heated at 60 °C for another 24 h to re-obtain **8**. The results were visualized by ^{1}H NMR spectroscopy, observing the appearance and disappearance of DA adduct signals in the 4.5 to 5.5 ppm range (Figure 4-8). Due to the non-quantitative reaction and generation of stereo-centers in the product, NMR spectra of the crude product were complex.[128,139]

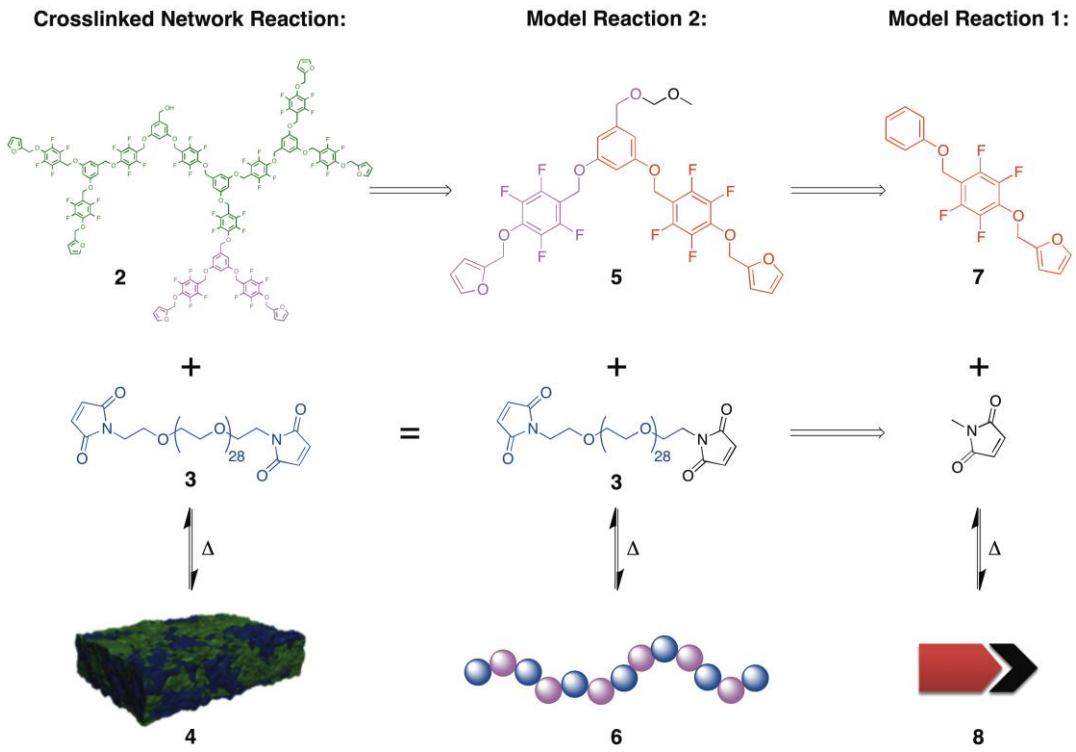

Scheme 4-13. Deconstruction of HBFP (**left, upper**) to an A_2 monomer (**middle, upper**) and a discrete molecule (**right, upper**), to understand the reversible nature of the Diels-Alder reaction in the substituted diene and dienophile sub-units of the crosslinked network system. Model reaction 2 involves a linear polymerization and the small molecule studies are model reaction 1.

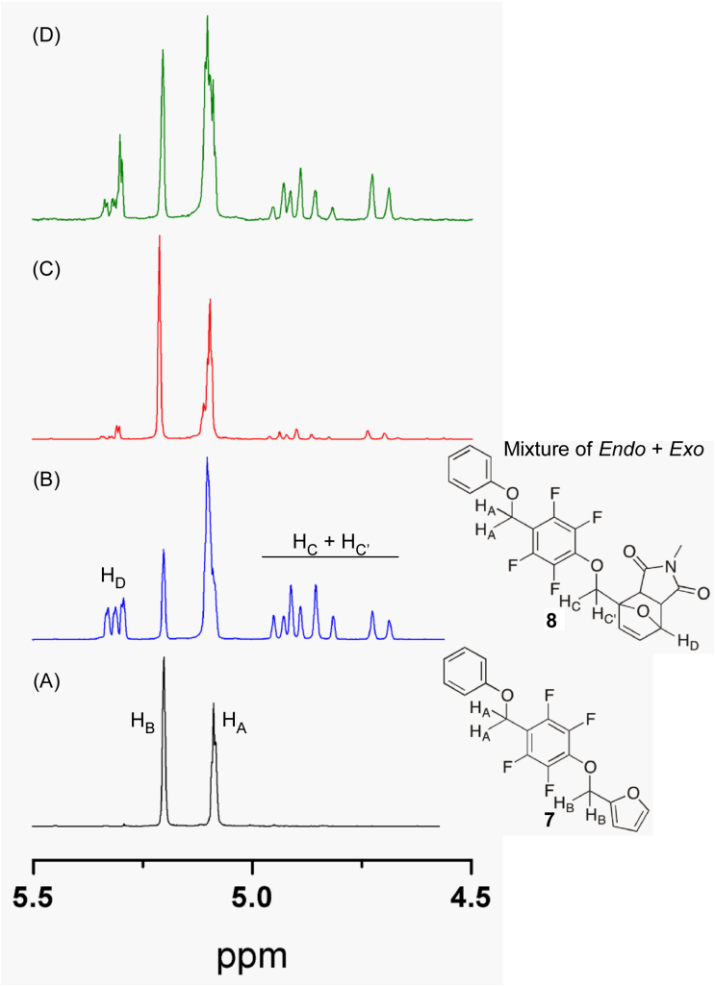

Figure 4-8. ^{1}H NMR spectra (300 MHz, $CDCl_3$) depicting model reaction 1 at various stages of the forward and reverse reaction conditions, performed in bulk: (A) starting materials (black); (B) DA adduct formation after heating at 60 °C for 24 h (blue); (C) retro-Diels-Alder after heating at 90 °C for 5 h (red); (D) reformation by heating at 60 °C for 24 h (green).

A second model system, that of a reversible, linear polymer (**6**) was studied, wherein a *bis*-furfuryl A_2 monomer, **5**, was copolymerized with **3** to resemble the eventual crosslinked networks, yet afford soluble products for analyses (Scheme 4-13, middle). The A_2 monomer, **5**, was synthesized in three steps, according to previously reported literature,[33] followed by protection of the benzylic alcohol of the intermediate **10** (which actually serves as the A_2B monomer for the preparation of HBFP **1**, the precursor to **2**) with methoxymethyl chloride to yield **11**, followed by substitution of the *para*-fluorines with furfuryl alcohol to give **5**, in an overall 43% yield.

Copolymerization of **5** and **3** was achieved by heating the bulk mixture of reagents at 60 °C for 24 h, the conditions that were identified from the small molecule model reaction 1. Accurate stoichiometry was attainted by first preparing stock solutions, mixing the components and allowing the solvent to evaporate before performing the polymerization. GPC was used to monitor the polymerization, showing formation of oligomers with a DP_n in the range 2 to 4 (Figure 4-9). Although slow, the growth of higher molecular weight oligomers was observed beyond 24 h, with a concurrent decrease in the amount of lower molecular weight components. While there are some examples of DA-mediated step-growth polymerizations that proceed much faster,[136] it is nonetheless comparable to others.[122]

Reversibility was once again demonstrated in model system 2. However, the reverse reaction, or depolymerization, was not accomplished following the protocol defined for the small molecule study and, rather, resulted in a gradual conversion to a brown, insoluble residue. Depolymerization instead was attainable by dissolving

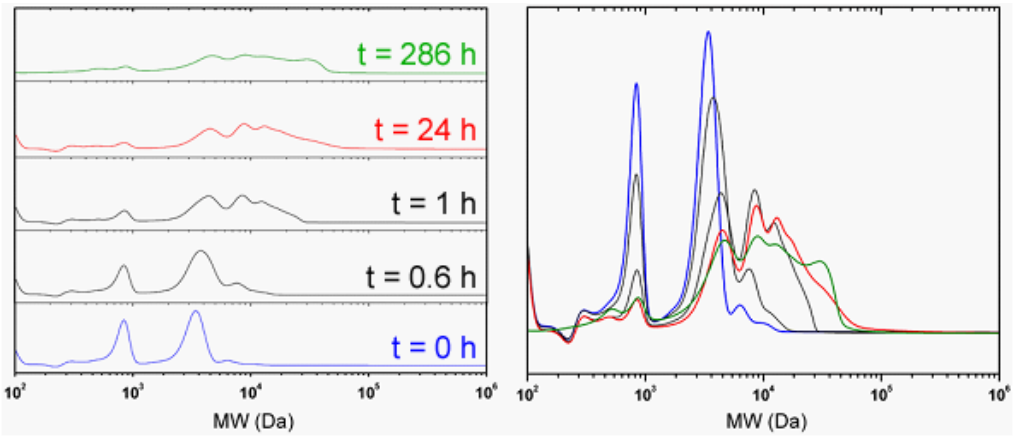

Figure 4-9. Stacked (**left**) and overlaid (**right**) GPC traces, depicting formation of oligomers of **6** from the copolymerization of **5** and **3**; t = 0 h (blue), t = 0.6 h (black), t = 1 h (black), t = 24 h (red), t = 286 h (green).

the crude mixture in toluene and heating at reflux for 24 h. Repolymerization was established by heating again in bulk at 60 ºC for 24 h. Each stage was confirmed by GPC (Figure 4-10).

Given the amphiphilic nature of **6**, it was postulated that under the appropriate conditions the oligomers/polymers could self assemble in aqueous solutions to form nano-aggregates. Two approaches were used to investigate the assembly behaviors of **6**:

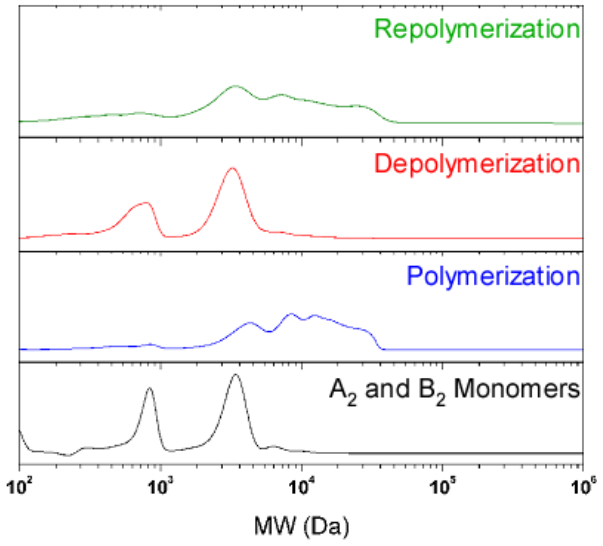

Figure 4-10. GPC spectra depicting forward and reverse reactions for a DA polymerization of the A_2 and B_2 monomers, **5** and **3**: polymerization in bulk at 60 °C for 24 h (blue); depolymerization in toluene heated at reflux for 24 h (red); repolymerization in bulk at 60 °C for 24 h (green).

(*i*) direct dissolution of the crude oligomeric mixture in water and (*ii*) dissolution in THF, followed by slow addition of water and dialysis to remove the organic solvent. Dynamic light scattering (DLS) analysis confirmed the presence of assemblies in both cases, with number-average hydrodynamic diameters of 37 ± 11 nm for method (*i*) (Figure 4-11) and 70 ± 19 nm for method (*ii*) (Figure 4-12), further demonstrating the versatility of these materials in potential applications.

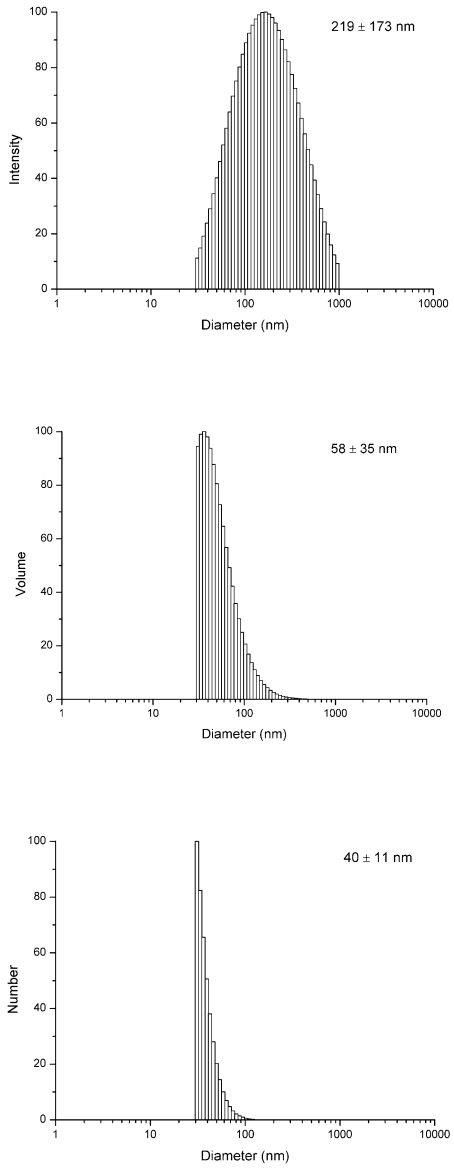

Figure 4-11. DLS histograms for nano-aggregates obtained *via* direct solubilization in water. Standard deviation over 10 runs: intensity ± 8 nm (4%), volume ± 5 nm (8%), number ± 3 nm (9%).

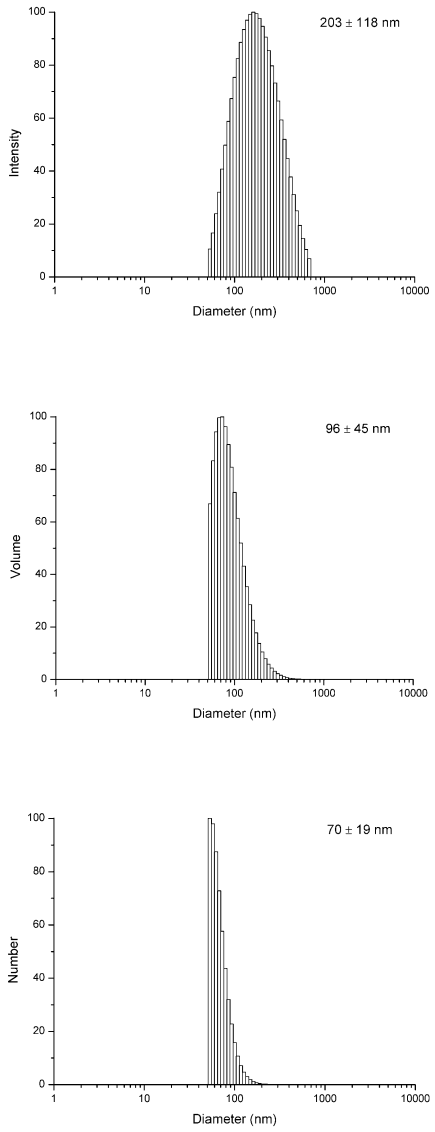

Figure 4-12. DLS histogram for nano-aggregates obtained *via* addition of water in THF. Standard deviation over 10 runs: intensity ± 8 nm (4%), volume ± 4 nm (4%), number ± 3 nm (4%).

Finally, DA-reversible amphiphilic crosslinked networks were studied. The first generation HBFP, **1**,[14,33] was modified to bear furfuryl moieties, **2**, and was co-deposited along with *bis*-maleimide PEG from dichloromethane, **3**, onto a glass slide to form a crosslinked network **4** (Scheme 4-13, left). After the solvent evaporated, the slides were cured at 60 ºC for 24 h. Successful crosslinking was determined by immersing the cured films in separate baths of THF and water. Whereas an uncured film dissolved, the cured coatings merely delaminated as flexible, optically-transparent films that remained intact. AFM analysis indicated a complex nanoscopically-resolved surface topography and comparison of dry cured films against water-immersed cured films revealed an increase in surface roughness, consistent with HBFP-PEG materials (Figure 4-13).[14]

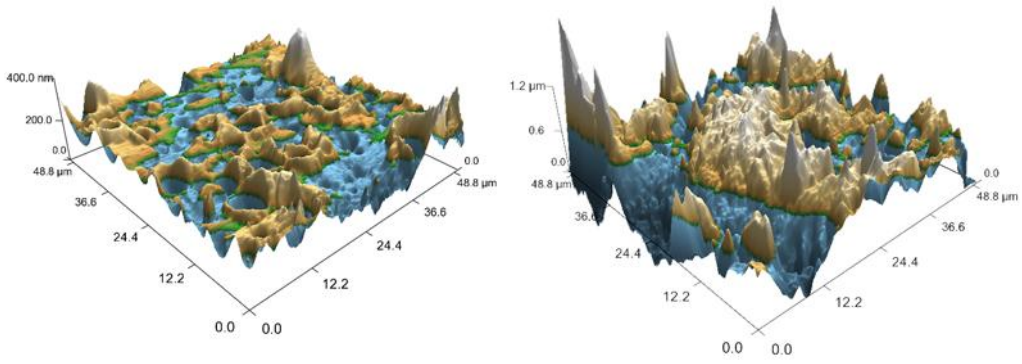

Figure 4-13. AFM images of DA-crosslinked HBFP-PEG film, **4**, dry (**left**) and after 24 h immersion in water (**right**).

Noting that **4** presented nanoscopic complexity and behaved in water similarly to the covalent counterpart obtained from crosslinking **1** and PEG, we believed that **4** would also resist protein adsorption and perform as an anti-biofouling coating.[35] Therefore, a PBS solution containing bovine serum albumin (BSA) conjugated to a fluorescent dye, AlexaFluor-488, was incubated on the surfaces of **4** and HBFP-PEG.[35] The fluorescence was collected before and after exposure to the protein solution to elucidate how well these surfaces resisted protein adsorption. We found that the increase in fluorescence after the introduction of BSA was low and similar to that of the covalently crosslinked HBFP-PEG (Figures 4-2, 4-3 and 4-4). This finding confirms that inclusion of the Diels-Alder crosslinking moieties did not significantly decrease the ability of these healable coatings to resist protein adsorption.

Initial investigations into the ability for the surface to be repaired following a damaging event provided promising preliminary data. Coatings were scratched by a file to induce light surface abrasions as well as cut with a sharp knife to inflict deeper gashes and then placed in an oven at 60 °C to stimulate the forward DA reaction and re-establish crosslinks.[109] After only 30 min, it was observed that the minor abrasions were healed. Deep cuts were partially healed after 3 h, but additional time at the elevated temperature did not appear to be of further benefit (Figure 4-14). A detailed analysis of the optical microscopy results can be found in the supporting information.

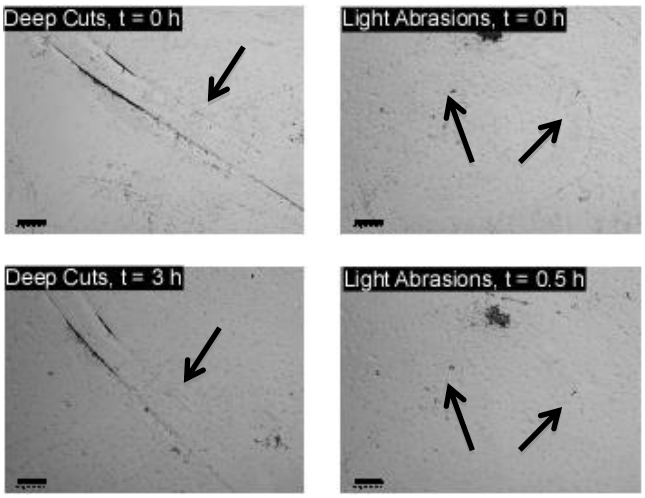

Figure 4-14. Images of Diels-Alder crosslinked HBFP-PEG films damaged with deep cuts (**upper left**) and light abrasions (**upper right**) and at 60 °C, the partial damage healing of cuts after 3 h (**lower left**) and complete healing of abrasions after 0.5 h (**lower right**). Scale bars = 200 μm.

4.6 Conclusions

Diels-Alder chemistry was used to produce a new generation of HBFP-PEG anti-biofouling coatings that are capable of repair. Small molecule and linear polymer model studies investigated the reactivity of the substituted diene and dienophile. The reversible nature of the DA cycloaddition was demonstrated in these model systems and proved to be a viable option for re-establishment of crosslinks in a damaged coating. HBFP-PEG coatings were produced through the curing of furan-modified HBFP and maleimide-

modified PEG. Testing of the scratch-healing ability of the coating surfaces revealed that small abrasions were healed in 30 minutes and large gashes were partially healed in 3 h. Without bulk flow, there is no mechanism to fill in large gaps and replace the material removed from serious damage. Future studies will consider localized heating above 100 °C to break all of the crosslinks surrounding a surface wound, promoting the flow of oligomers to smooth out the surface, followed by heating at 60 °C to re-establish the crosslinked network. AFM revealed a topographically-complex surface, which was shown to resist protein adsorption, as confirmed by a fluorescently-labeled protein assay. The similarities between this system and the conventional HBFP-PEG, in terms of both chemical composition and resistance to protein adsorption, suggest similar anti-biofouling behavior against marine microorganisms. This study provides a new strategy of combining materials of known anti-biofouling ability with reversible crosslinks to impart a healable trait into the material, and functions as a guide for future formulations that optimize the effective application of these materials.

4.7 Acknowledgements

The Office of Naval Research under N00014-10-1-0527 and the W. T. Doherty-Welch Chair in Chemistry under Grant No. A-0001 provided financial support and are gratefully acknowledged. We thank the Laboratory for Biological Mass Spectrometry at Texas A&M University for small molecule mass spectral analysis. We also thank the editors of ACS Macro Letters for selecting the original publication to be featured on the cover of their 4th issue (Figure 4-15).

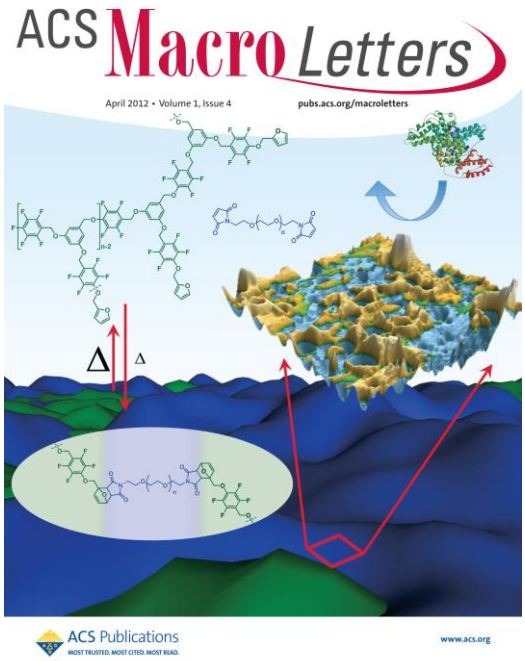

Figure 4-15. Article featured on the cover of *ACS Macro Letters*, Volume 1, Issue 4.

CHAPTER V

THIOL-ENE "CLICK" NETWORKS FROM AMPHIPHILIC FLUOROPOLYMERS: FULL SYNTHESIS AND CHARACTERIZATION OF A BENCHMARK ANTI-BIOFOULING SURFACE*

5.1 Original Publication Information

This chapter was originally submitted on March 30, 2012 as an article in the *Journal of Materials Chemistry*, an invited contribution to the **Themed Issue on Materials for Biosurfaces**:

Collaborative contributions: J. Raymond conducted spectroscopy experiments, atomic force microscopy experiments and IR analysis; B. Tucker helped synthesize monomers and polymers and **LP** surfaces.

Modifications to the original document are cosmetic and used only to conform the format of this document or provide uniformity of enumeration. Contents found in the supporting information, which was originally a separate document, has been included in the chapter, and schemes and figures have been renumbered to conform to the style of this document.

---

*Reprinted with permission from "Thiol-ene "Click" Networks from Amphiphilic Fluoropolymers: Full synthesis and characterization of a benchmark anti-biofouling surface", by Philip M. Imbesi, Jeffery E. Raymond, Bryan S. Tucker and Karen L. Wooley, **2012**, *Journal of Materials Chemistry*, Advance Article DOI: 10.1039/C2JM32005C, Copyright 2012 by The Royal Society of Chemistry. http://pubs.rsc.org/en/content/articlelanding/2012/jm/c2jm32005c

5.2 Overview

The synthesis of heterogeneous, amphiphilic crosslinked networks from photo-initiated thiol-ene chemistry and full characterization of the physicochemical, anti-biofouling, mechanical, and thermal properties of this system are reported. Although interest in coatings that present heterogeneous surface features is increasing, anti-biofouling performance is typically compared to homogeneous biocidal- or non-toxic polydimethylsiloxane-based paints, for the advancement of commercial and novel systems, which leaves a need for a benchmark to compare highly-complex, heterogeneous composites with similar complexities. This system has been generated and rigorously analyzed to understand how microscopic and nanoscopic disorder, resistance to protein adsorption and surface mechanical properties can be fine-tuned and optimized through oligomer selection, blend ratios and process conditions. Solution-state studies of individual and blended constituents probed the relative fluorescence intensities based on concentration and neighboring species that were used to identify microscopic disorder on the surface. Incubation of a fluorescently-labeled protein on the benchmark surface showed 42% and 72% less adsorption than on model surfaces that largely expressed a single component. The extent of reaction and the identification of unconsumed functionalities were found through infrared spectroscopy. The benchmark surface had a Young‟s modulus of approximately 0.5 GPa, 7 to 35 times higher than model surfaces, with 50 times the variation in modulus. Nanoscale surface energy variation and bulk wettability and bulk thermal stability are also reported. This study

provides an extensive list of metrics to be used for the development of complex, heterogeneous, anti-biofouling coatings, appropriate to both surface optimization and mechanical tunability, for implementation in real-world applications.

5.3 Introduction

An environmentally-benign ship hull coating has been desired to combat fouling since the maritime ban of tributyltin (TBT) paints in the 1970s.[1,2] Biofouling on ship hulls can account for up to 70% increased fuel and operational costs.[4,8] One approach to the prevention of marine organism settlement is presenting nanoscopically-complex surface features and chemistry variations, where it has been hypothesized that a variation in surface chemistry,[13] energy,[25] modulus,[26] and roughness[27-29] influences the ability for an organism to sense, settle and attach to a surface. As these polymeric coatings grow in complexity and are assessed for development, there is a need to analyze the bulk film as well as the response of individual micro- and nano-domains. Understanding the region-by-region complexity requires clear and accessible metrics to allow direct correlation of feature characteristics to performance. This is in contrast to the typical approach, where bulk comparisons to non-heterogeneous materials have been the standard, with few metrics tracking surface response.[12,18]

One type of highly-complex surface is that comprised of binary mixtures of hyperbranched fluoropolymers crosslinked with poly(ethylene glycol) (HBFP-PEG).[14] Formulating coatings with HBFP and PEG has demonstrated unique anti-fouling

properties[35,36] that are believed to be derived from the combination of complex surface topographies, morphologies, and compositions over nano- and microscopic dimensions. However, there are drawbacks to using previous iterations of the HBFP-PEG polymer systems that may prevent the transition of these formulations into a commercially-viable coating.[14] These include the long reaction times,[33] high coating deposition temperatures[35,36] and a limited overall mechanical strength.[37,38]

To address these issues, we synthesize here a new system that continues to take advantage of fluoropolymers and PEG chemistry to generate complex surface features. A more robust crosslinking chemistry that overcomes the mechanical and processing drawbacks of previous systems is utilized, while maintaining surface complexity. Thiol-ene "click" chemistry has been used industrially since the 1970s,[142,143] but recently has been incorporated into flame retardant coatings,[144] polymer systems[30,115,116] and lithographic films[145,146] due to the robust, rapid and efficient nature of the reaction. The incorporation of thiol-ene crosslinking in bulk films has shown these systems to possess insensitivity to oxygen,[147] low shrinkage,[148] high thermal stability while proceeding to relatively high conversion in short timeframes.[117,149,150] We briefly investigated thiol-ene crosslinked fluoropolymers for anti-biofouling surfaces, and we follow that up here with a systematic development study.[31]

This study will outline a detailed method to reduce amphiphilic, thiol-ene generated polymeric coatings to their core constituents, extensively characterizing the networks and the individual components from which they are comprised. A benchmark anti-biofouling coating (**LP**) was obtained from a linear, amphiphilic fluoropolymer with

pendant alkene functionality (LFPene) crosslinked into a polymeric network with commercially-available pentaerythritol tetrakis(3-mercaptopropionate) (PETMP) in order to understand the component contributions to surface morphology and performance. Two model surfaces obtained from crosslinking either LFPene or PETMP (**LH** and **PH**, respectively) with a short hydrocarbon of compatible thiol-ene functionality were used for comparative purposes to determine the polymer and crosslinker roles in surface performance. A series of experiments was performed on individual, blended, and crosslinked components in both the solution state and the solid state to determine:

1. Constituent interactions through multi-dimensional spectroscopic studies of serial dilutions and blends;
2. Resistance to protein binding with biomacromolecule adsorption on benchmark and model surfaces;
3. Extent of reaction *via* surface infrared spectroscopy;
4. Surface energy with bulk contact angle and nanoscale surface adhesion force spectroscopy;
5. Physical and chemical heterogeneity through micro- and nanoscale topography and force-volume spectroscopy;
6. Thermal response by degradation and phase transition analysis.

Herein, a robust method for the preparation and analysis of these benchmark coatings will be discussed. Specifically, correlation of the spectroscopic and microscopic data to the crosslinked surface character is used to define future considerations in formulation

requirements and cure conditions for optimized surfaces in anti-biofouling applications. This study provides fully for the generation of a complex benchmark surface where component response is related directly to the tunable properties and ultimate performance of a system.

5.4 Experimental

5.4.1 Materials

Reagents and starting materials were purchased from Sigma Aldrich and used as received unless otherwise noted. 2,3,4,5,6-Pentafluorostyrene (PFS) was purchased from Apollo Scientific (UK) and filtered through a plug of neutral alumina prior to use. Bovine serum albumin (BSA) conjugated to AlexaFluor-488 was purchased from Invitrogen.

5.4.2 Monomer and Polymer Characterization

Synthesized molecules were characterized by ^{1}H, ^{13}C and ^{19}F nuclear magnetic resonance (NMR) spectroscopies using a Varian Inova 300 MHz spectrometer. ^{1}H and ^{13}C NMR spectra were analyzed using the solvent signal as an internal reference and ^{19}F NMR spectra were analyzed with CF_3COOH as an external standard. IR spectra were obtained on a Shimadzu IR Prestige Attenuated Total Reflectance Fourier-transform

Infrared Spectrometer (ATR-FTIR). Spectra were analyzed using IRsolution software package (Shimadzu). High-resolution mass spectrometry (HRMS) was conducted on an Applied Biosystems PE SCIEX QSTAR. Gel permeation chromatography was performed on a Waters Chromatography, Inc. (Milford, MA), 1515 isocratic HPLC pump equipped with an inline degasser, a model PD2020 dual-angle (15° and 90°) light scattering detector (Precision Detectors, Inc.), a model 2414 differential refractometer (Waters, Inc.), and four PL_{gel} polystyrene-*co*-divinylbenzene gel columns (Polymer Laboratories, Inc.) connected in series: 5 μm Guard (50 × 7.5 mm), 5 μm Mixed C (300 × 7.5 mm), 5 μm 10^4 (300 × 7.5 mm), and 5 μm 500 Å (300 × 7.5 mm) using the Breeze (version 3.30, Waters, Inc.) software. The instrument was operated at 35 °C with THF as the eluent (flow rate set to 1.00 mL/min). Polymer solutions were prepared at a known concentration (*ca*. 3 mg/mL) and an injection volume of 200 μL was used. Data collection was performed with Precision Acquire 32 Acquisition program (Precision Detectors, Inc.) and analyses were carried out using Discovery32 software (Precision Detectors, Inc.) with a system calibration curve generated from plotting molecular weight as a function of retention time for a series of broad polydispersity poly(styrene) standards. Differential scanning calorimetric (DSC) studies were performed on a Mettler-Toledo DSC822^e (Mettler-Toledo, Inc., Columbus, OH), with a heating rate of 10 ºC/min. The T_g was taken as the midpoint of the inflection tangent, upon the third heating scan. Thermogravimetric analysis was performed under Ar atmosphere using a Mettler-Toledo model TGA/DSC 1 Star^e system, with a heating rate of 10 ºC/min. Measurements were analyzed using Mettler-Toledo Star software version 10.00c.

5.4.3 Synthesis

4-[Oxy(tri(ethylene glycol))]-2,3,5,6-tetrafluorostyrene (1). To a stirring solution of sodium hydride (60 wt% dispersion in mineral oil, 4.95 g, 124 mmol) in THF (400 mL) in a 1 L two-neck round-bottomed flask suspended in an ice bath, was added tri(ethylene glycol) (TrEG) (41.3 mL, 309 mmol), followed by the addition of PFS (14.2 mL, 20.0 g, 103 mmol). The solution was allowed to warm to room temperature with stirring under N_2 for 14 h. The reaction mixture was then concentrated *in vacuo*, dissolved in deionized water (300 mL) and extracted with ethyl acetate (4 x 300 mL). The organic fractions were combined, dried over anhydrous $MgSO_4$, filtered and concentrated *in vacuo* to afford a clear, pale yellow oil. Further purification by silica gel flash chromatography using 10% MeOH in CH_2Cl_2 as the eluent afforded **4** as a clear, colorless oil in 62% yield (20.6 g). T_{decomp}: 362 °C, 74% mass loss @ 500 °C. IR = 3600-3200, 3050-2800, 1643, 1489, 1358, 1288, 1250, 1080, 941 cm^{-1}. ^1H NMR (acetone-d_6, ppm): δ 6.60 (dd, *J* = 12 Hz and 18 Hz, 1H, H_2C=C***H***-R), 5.96 (d, *J* = 18 Hz, 1H, ***H***(H)C=CH-R (*trans*)), 5.65 (d, *J* = 12 Hz, 1H, H(***H***)C=CH-R (*cis*)), 4.38 (t, *J* = 5 Hz, 2H, TFS-O-C***H***$_2$-CH_2-OR), 3.78 (t, *J* = 5 Hz, 2H, TFS-O-CH_2-C***H***$_2$-OR‟) and 3.40-3.70 (m, 8H, R-O-(C***H***$_2$-C***H***$_2$-O-C***H***$_2$-C***H***$_2$-OH). ^{13}C-NMR (acetone-d_6, ppm): δ 147.2, 143.7, 143.0, 140.2, 137.3, 122.5, 122.4, 122.3, 122.2, 111.0, 74.8, 73.2, 71.1, 70.8, 70.5 and 61.6. ^{19}F NMR (acetone-d_6, ppm): δ -147 (m, 2F, *ortho*-***F*** to -CH=CH_2) and -159 (m, *meta*-***F*** to -CH=CH_2). HRMS m/z calculated for $C_{14}H_{16}F_4O_4$ $[M + H]^+$ 325.10 Da, found 325.1063 Da.

[2,3,5,6-tetrafluoro-4-vinylphenoxy-tri(ethylene glycol)]yl but-3-enoate (2). To a 1 L round bottom flask equipped with a magnetic stir bar was added **1** (14.3 g, 44.0 mmol), 3-butenoic acid (4.82 g, 52.3 mmol), *N,N'*-dicyclohexylcarbodiimide (DCC) (18.2 g, 88.0 mmol) and 4-dimethylaminopyridine (DMAP) (1.08 g, 8.84 mmol) and dissolved in CH_2Cl_2 (500 mL). The reaction was allowed to stir 48 h at room temperature under N_2. Following the completion of the reaction, the precipitate was removed by filtration, and the crude product was washed with $NaHCO_3$ (3 x 500 mL). The organic fraction was dried over $MgSO_4$, filtered, and concentrated. Further purification by silica gel flash chromatography using a gradient from 1:3 ethyl acetate:hexanes to 1:1 ethyl acetate:hexanes as the eluent afforded **2** as a clear, colorless oil in 60% yield (10.41 g). T_{decomp}: 363 °C, 72% mass loss @ 500 °C. IR = 3350-3150, 3150-3030, 3000-2850, 1728, 1635, 1581, 1489, 1427, 1257, 1118, 1026, 1026, 933, 794 and 578 cm^{-1}. ^1H NMR (300 MHz, $CDCl_3$, ppm): δ 6.7-6.5 (dd, *J* = 12 Hz and 18 Hz, 1H, H_2C=C***H***-R) 6.1-6.0 (d, *J* = 18 Hz, 1H, ***H***(H)C=CH-R (*trans*)), 6.0-5.8 (m, 1H, O-C(O)-CH_2-C***H***=CH_2), 5.6 (d, *J* = 12 Hz, 1H, H(***H***)C=CH-R (*cis*)), 5.2-5.1 (m, 2H, O-C(O)-CH_2-CH=C***H***$_2$), 4.4 (t, *J* = 5 Hz, 2H, TFS-O-C***H***$_2$-CH_2-), 4.2 (t, *J* = 5 Hz, 2H, -CH_2-C***H***$_2$-O-C(O)-), 3.8 (m, 2H, TFS-O-CH_2-C***H***$_2$-), 3.7-3.5 (br m, 6H, -C***H***$_2$-C***H***$_2$-O-C***H***$_2$-) and 3.2 (m, 2H, O-C(O)-C***H***$_2$-CH=CH_2). ^{13}C NMR (75 MHz, $CDCl_3$, ppm): 171.5, 146.7, 143.4, 142.9, 139.6, 136.5, 130.2, 122.4, 122.1, 118.6, 110.9, 74.2, 70.9, 70.6, 70.3, 69.1, 63.8 and 39.0. ^{19}F NMR (300 MHz, $CDCl_3$, ppm): δ -147 (m, 2F, *ortho*-***F*** to CH_2=CH-) and -159 (m, 2F, *meta*-***F*** to CH_2=CH-). HRMS m/z calculated for $C_{18}H_{20}F_4O_5$ $[M+Li]^+$ 399.061 Da, found 399.1407 Da.

Linear Fluoropolymer (LFPene) Synthesis (3). To a 500 mL Schlenk flask equipped with stir bar was added copper(I) bromide (0.175 g, 1.22 mmol), **2** (12.01 g, 30.6 mmol, 24 equiv.), PFS (23.8 g, 122 mmol, 96 equiv.), ethyl-2-bromopropionate (0.232 g, 1.28 mmol), pentamethyldiethylenetriamine (PMDETA) (0.497 g, 2.87 mmol), and anisole (70 mL). The solution was deoxygenated *via* three cycles of freeze-pump-thaw and was then lowered into an oil bath set to 85 °C for 6 h. The reaction was quenched in liquid nitrogen, diluted in CH_2Cl_2 (400 mL), and filtered through a plug of neutral alumina to remove the catalyst. The filtrate was concentrated *via* vacuum distillation and the polymer was isolated by three successive precipitations into cold hexanes from CH_2Cl_2 to yield a white powder of **3** in 55% yield at 50% conversion (10.27 g). M_w^{GPC} = 14600 Da, M_n^{GPC} = 12200 Da, M_w/M_n = 1.20. T_g = 39 °C. T_{decomp}: 414 °C, 72% mass loss @ 500 °C. IR = 2947, 2877, 1735, 1651, 1496, 1365, 1249, 1126, 1095, 956, 871, 740 cm^{-1}. ^1H NMR ($CDCl_3$, ppm): δ 6.0-5.8 (br m, R-CH_2-C***H***=CH_2), 4.4-4.2 (br m, TFS-O-C***H***$_2$-R and CH_2-C***H***$_2$-C(O)O-R‟‟), 3.8-3.5 (br m, R-O-C***H***$_2$-C***H***$_2$-O-R‟‟), 2.8-1.8 (3 br s, C***H***$_2$-C***H***(R), backbone) and 1.1 (br m, C-C***H***$_3$, initiator). ^{13}C-NMR ($CDCl_3$, ppm): 171.6, 165.0, 146.3, 143.2, 139.1, 135.7, 130.2, 118.5, 113.1, 74.4, 70.9, 70.7, 70.0, 69.2, 63.8, 39.0, 37.6 and 32.2. ^{19}F NMR ($CDCl_3$, ppm): δ -144 (br m, *ortho*-***F*** (PFS) and *ortho*-***F*** (TFS)), -154 (br m, *para*-***F*** (PFS)), -157 (br m, *meta*-***F*** (TFS)), -161 (br m, *meta*-***F*** (PFS)).

5.4.4 Casting Methods

General procedure for the preparation of LFPene-PETMP coatings (LP). To a scintillation vial was added **3** (80.0 mg, 1.0 equiv.), pentaerythritol tetrakis(3-mercaptopropionate) (PETMP) (40.0 mg, 33 wt%) and 1-hydroxycylcohexylphenyl ketone (6.0 mg, 5 w/wt%). The reagents were dissolved in 1,4-dioxane (2.0 mL) and vortexed until homogeneous. The solution was spin-cast (3000 RPM, 30 s) onto glass microscope cover slips and passed twice through a Fusion UV 300S conveyer system equipped with an H bulb (300 W/in) at a speed of 1 m/min (60 sec total UV exposure time) to crosslink coatings of **LP**.

General procedure for the preparation of LFPene / hexane dithiol crosslinked networks (LH). The procedure for **LP** was followed using **3** (79.8 mg), hexane dithiol (40.0 mg, 33 wt%), 1-hydroxycyclohexylphenyl ketone (6.0 mg, 5 w/wt%) and 1,4-dioxane (2 mL) to cast spin-coated replicates of **LH**.

General procedure for the preparation of PETMP / 1,5-hexadiene crosslinked networks (PH). The procedure for **LP** was followed using PETMP (80.0 mg), 1,5-hexadiene (40.3 mg, 33 wt%), 1-hydroxycyclohexylphenyl ketone (5.9 mg, 5 w/wt%) and 1,4-dioxane (2 mL) to cast spin-coated replicates of **PH**.

5.4.5 2D Steady State Spectroscopy

Multidimensional excitation-emission spectra were obtained for all solutions with a RF-5301 PC spectrofluorophotometer (Shimadzu). Data analysis and peak deconvolution was performed with Origin 8.5 software. UV-Vis maxima for all solutions were obtained with a UV-2550 UV-Vis spectrophotometer (Shimadzu). A quartz 0.7 mL cell was used in all solution measurements (Starna, Inc.).

5.4.6 Fluorescence Microscopy and Biofouling Characterization

Fluorescence microscopy was conducted on an Olympus IX70 inverted microscope equipped with a mercury arc lamp and an Olympus DP72 digital camera. Images were collected through a 20× objective (Olympus UPlanFl). Excitation and emission collection was achieved with the use of an Olympus U-MNIBA3 filter cube (excitation: 470-495 nm, emission: 510-550 nm). Wide field phase contrast imaging was performed in order to return to the same region of interest. All collection during fluorescence imaging was done with the same optics set and with the same collection time and CCD gain in order to maintain comparability from frame-to-frame.

The implicit method for quantitative bovine serum albumin (BSA) uptake analysis as a biofouling proxy is discussed elsewhere.[35,151] In brief, all surfaces were imaged to determine the autofluorescence levels and a collection regime was selected that removed the autofluorescence background through CCD and exposure time

adjustment. The surfaces were exposed to AlexaFluor-488 conjugate BSA in phosphate buffered saline (PBS) (pH=7.1) at 0.1 mg/mL for 5 min and dried *via* filtered nitrogen gas. Returning to the same regions observed initially, fluorescence images were taken of the BSA exposed surfaces and were discussed in terms of resultant intensity histograms.

5.4.7 Attenuated Total Reflectance Fourier-transform Infrared Spectroscopy (ATR-FTIR)

All FTIR spectra were collected in ambient conditions using a diamond ATR lens with a typical penetration depth <200 nm (IRPrestige, Shimadzu). Preparation for collection was performed with single drops of solution, pressed powder, or pressed films depending on sample form factor.

5.4.8 Atomic Force Microscopy and Surface Force Spectroscopy

A Bruker Multimode 8 atomic force microscope (AFM) with a ScanAsyst-Air probe (Bruker, Si_3N_4, k = 0.4 N/m) was used to collect topographic, surface mechanical and surface energy micrographs of the **LP**, **LH** and **PH** surfaces. A detailed description of the methods used is provided in the supporting information. In brief: Off-resonance cantilever oscillation was used to provide extremely gentle tip-sample interactions with average deformations of ~3 nm. In addition to topography, the DMT model[152,153] was applied to each pixel‟s force approach curve to directly calculate the Young‟s modulus.

Similarly, the adhesion force was generated by taking the differential of the approach energy and release energy for each pixel. These adhesion force spectra can be directly related to the nanoscopic surface energy and in turn the surface availability of functional groups capable of strongly interacting with the lone electron pairs of the Si_3N_4 probe. The modulus spectra can be directly related to the extent of crosslinking and the nature of the surfaces‟ chemical characteristics.

5.4.9 Static Water Contact Angle Measurements

Contact angles were measured as static contact angles using the sessile drop technique[53] with an Attension Theta optical tensiometer (Biolin Scientific). Drops were fitted with a Young-Laplace formula to calculate the static contact angle in the Theta software (Biolin Scientific). The reported values are averages of five such measurements on different regions of the same sample.

5.5 Results and Discussion

5.5.1 Synthesis

The synthetic approach towards a linear amphiphilic fluoropolymer that contained similar traits as HBFP predecessors,[14] while also bearing functionality for photo-initiated crosslinking, relied upon the incorporation of a comonomer with reactive terminal alkene functionality that would be available post-polymerization. Therefore, a substituted tetrafluorostyrene with a polymerizable styrenyl head group, a tri(ethylene glycol) spacer and an alkenyl pendant group, **2**, was copolymerized in the presence of PFS to generate a polymer with a hydrophobic backbone, hydrophilic side chains and pendant functionality available for crosslinking. The preparation of **2** began from the nucleophilic aromatic substitution of the *para*-fluorine of PFS with an excess of tri(ethylene glycol) (TrEG), to give **1**, followed by esterification of the alcohol group with 3-butenoic acid in the presence of DCC and DMAP to yield the amphiphilic, functional monomer, **2** (Scheme 5-1). The linear fluoropolymer with alkene functionality (LFPene), **3**, was synthesized *via* atom transfer radical polymerization (ATRP) to control the molecular weight of the polymer and yield the reactive chain ends. Copolymerization of **2** with three molar equivalents of PFS achieved **3**, bearing TrEG with pendant functionality extending from the backbone. Monitoring the reaction by ^{1}H NMR spectroscopy revealed a transformation of the styrenyl protons of the

monomer into the aliphatic backbone of the polymer without the consumption of the alkenyl group (Scheme 5-1).

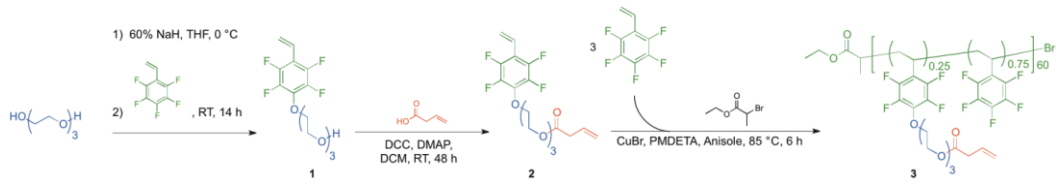

Scheme 5-1. Synthesis of amphiphilic, linear fluoropolymer with pendant alkene functionality (LFPene), **3**, *via* atom transfer radical polymerization (ATRP).

The heterogeneous benchmark surface, **LP**, was designed to combine chemical, morphological and topographical complexities from the crosslinking of the LFPene and PETMP components. Crosslinked coatings of **LP** were obtained from deposition of the LFPene polymer, **3**, with a tetrathiol crosslinker, PETMP, in the presence of a photo-initiator, 1-hydroxycyclohexylphenyl ketone, through spin casting followed by curing upon brief exposure to UV light. The ratios used (67 wt% polymer, 33 wt% crosslinker) was a formulation consistent with HBFP-PEG systems.[48] In order to identify contributions from both the polymer and crosslinker, model films of LFPene crosslinked with hexane dithiol (**LH**) and PETMP crosslinked with 1,5-hexadiene (**PH**) were prepared in a similar manner, to isolate the effects of LFPene and PETMP from interactions between LFPene and PETMP (Scheme 5-2).

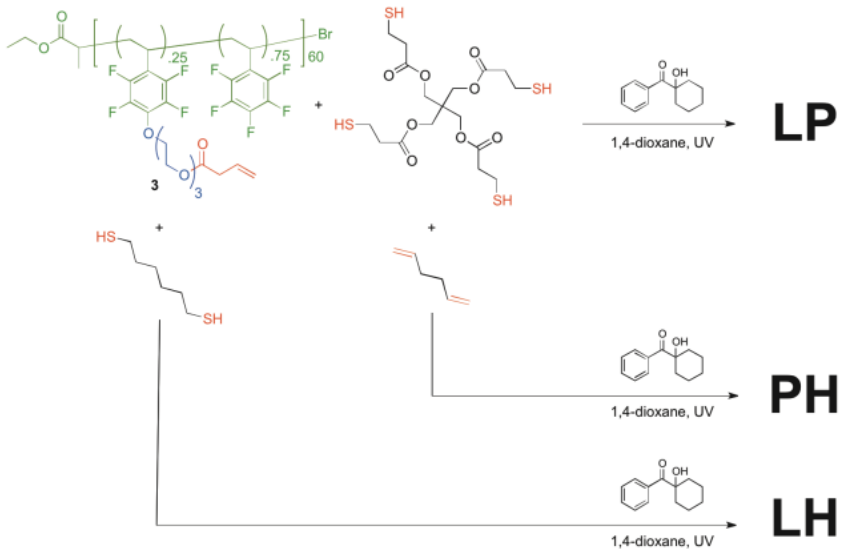

Scheme 5-2. Synthesis of a benchmark crosslinked network from **3** and PETMP (**LP**) as well as LFPene and PETMP test surfaces (**LH** and **PH**, respectively) *via* photo-initiated, thiol-ene click chemistry.

5.5.2 2D Steady State Spectroscopy

Three series of LFPene dilutions in 1,4-dioxane were investigated by excitation-emission spectroscopy in order to probe the effect of concentration on LFPene-PETMP interactions (Figure 5-1). The PFS monomer, monomer **2** and a pure sample of 1,4-dioxane (**S**) were also observed. In brief, the L-series is a dilution of LFPene, the B-series is a dilution of blended LFPene and PETMP in a 2:1 ratio, and the P-series holds LFPene concentration constant with PETMP concentration varied. The multi-

dimensional excitation-emission spectra are presented in Figure 5-1. UV absorption spectroscopy displayed strong dioxane absorption at <200 nm and an LFPene absorption which scaled linearly and blue shifted from 223 to 218 nm with dilution. The solutions with high (1 wt%) LFPene concentration also displayed a small amount of absorption at 360 nm. A summary of all series dilutions can be found in Table 5-1.

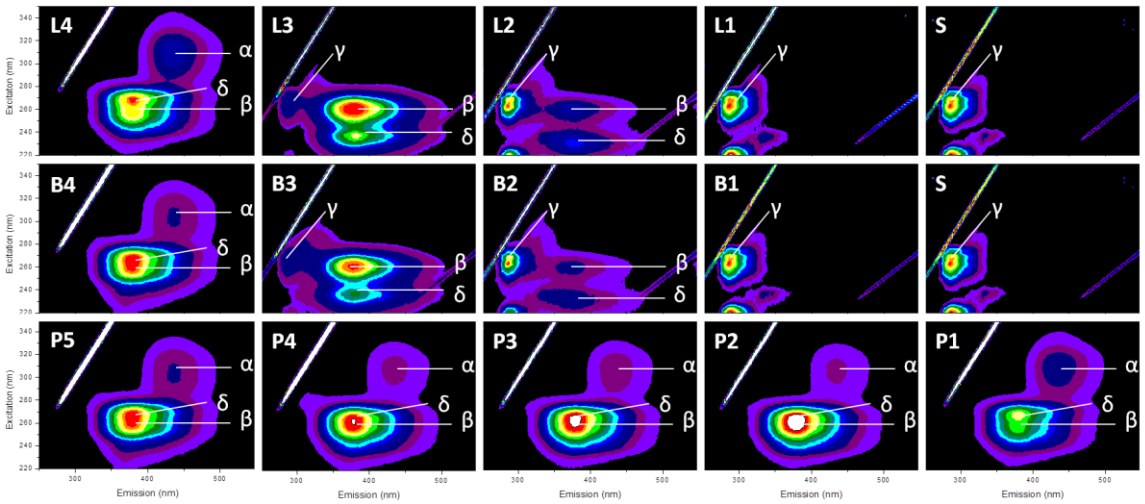

Figure 5-1. 2D Excitation-Emission Spectra for L-, B- and P-Series Solutions. Excitation (left axis) ranges from 220 nm to 350 nm; emission (bottom axis) ranges from 250 nm to 550 nm; 2 nm step size (both).

Table 5-1. Composition and Relative Emissivity of L-, B- and P-Series. Emission is relative to **L4**/**P1** and includes the integrated sum of β and δ emission at 380 nm.

Solution	**Fluoropolymer (wt%)**	**PETMP (wt%)**	**Relative Emission (au)**	**Observable α-Peak Emission?**
L4/P1	1	0	1	Y
L3	0.1	0	10	N
L2	0.01	0	15	N
L1	0.001	0	34	N
B4/P5	1	0.5	1.24	Y
B3	0.1	0.05	8.4	N
B2	0.01	0.005	12	N
B1	0.001	0.0005	17	N
P4	1	0.05	1.29	Y
P3	1	0.005	1.33	Y
P2	1	0.0005	1.40	Y
PFS	1	0	<0.01	N
2	1	0	0.4	N
PETMP	0	0	0	N
Dioxane	0	0	0	N

L-Series:

The L-Series of dilutions are LFPene in 1,4-dioxane (**L4**-**L1**). Four peaks can be readily observed in the L-series and labeled α, β, δ, and γ.

α-Peak. The first peak of interest is emission (440 nm) from an excitation band of significantly lower energy (310 nm) than the other observed emissions. As this peak is only observable at the highest LFPene concentrations, it is interpreted to occur as a result of extensive interactions between a fraction of the pentafluorophenyl units. This interaction appears to generate an electronically coherent ensemble which displays characteristics of a pi-conjugated system larger than an individual substituent. This peak was, therefore, assigned to be a $\pi \rightarrow \pi^*$ transition in coherently interacting LFP subunits. Overall, this is interpreted to imply a high degree of chain collapse and a likelihood of intermolecular interactions contributing to additional pi character in aggregate.

β-Peak. The second peak of interest is an emission peak (380 nm) energy-matched to the higher energy solvent emission maximum (290 nm) at an excitation wavelength of ~265 nm. This peak could readily be attributed to LFPene emission after either energy transfer (ET) from the solvent or reabsorption of solvent emission after solvent excitation. Given the extremely well matched excitation regimes of both the β-peak emission and the solvent emission peak (γ-peak), as well as the total lack of solvent signal in **L4**, the spectra suggest a highly efficient and energy selective process. This peak is, therefore, interpreted to be indicative of a short range ET process from ζ^*_{solvent} resulting in $\pi_{\text{LFPene}} \rightarrow \pi^*_{\text{LFPene}}$ and subsequent emission. With decreasing concentration, this peak is replaced by γ-peak emission as ET events become less likely. The fact that

ET is not observed to the α-peak further supports the claim of a collapsed, self-interacting system at high concentration.

δ-Peak. Before loss of the majority of LFPene signal at low concentration (**L1**), a higher energy excitation peak can be observed at the same emission wavelength as the β-peak. This peak (δ) can be seen to require greater excitation energy as concentration decreases. This trend again strongly suggests an increased amount of coherent interaction between LFP subunits with increased concentration. Given that the δ-peak excitation changes with concentration, unlike the β-peak where solvent ET drives LFPene excitation, a direct $\pi_{LFPene} \rightarrow \pi^*_{LFPene}$ excitation can be assumed.

γ-Peak. The γ-peak has been assigned to the $n_{solvent} \rightarrow \zeta^*_{solvent}$ transition and resulting solvent emission. This assignment is reasonable, as the onset of the $\zeta_{solvent} \rightarrow \zeta^*_{solvent}$ transition can be observed at the fringe of the highest energy limit of the excitation detection. Increased emission intensity with decreasing concentration should be taken as an indicator of a decreased ET rate to LFPene after solvent excitation, most likely due to an overall decrease in the likelihood of solvent excitation occurring in proximity to a LFPene molecule.

The emission from 260 nm excitation clearly showed the transition from pure LFPene emission (β) in **L4** to a solvent-like emission for **L1** (γ). Both the solvent and the LFPene show a vibronic shoulder to the right of the primary emission, typical for emission spectra of room temperature solutions. The excitation trend for 380 nm emission displays a blue-shift of the δ-peak with decreased LFPene concentration. The

additional excitation energy required for similar emission energies supports a decreased interaction between LFP units at lower concentrations.

The L-series dilution study makes clear that ET from the solvent plays a large role in the primary emission peaks of this material. It has also been shown that the LFP-LFP interactions increase with increasing concentration, culminating in electronically coherent LFP regions in **L4**. These regions are capable of emission independent of solvent excitation and should be taken as the major signaling agent in fluorescence microscopy applications where 400 – 500 nm emission is monitored from >300 nm excitation.

P-Series:

Holding LFPene concentration constant at 1 wt%, a series of solutions with decreasing PETMP concentration was generated (**P5**-**P1**). This was performed in order to observe the photophysical response of increased LFPene interaction with increasing PETMP.

Two trends are revealed immediately from direct observation of the P-series spectra. First, PETMP clearly enhances the δ/β emission of LFPene, while suppressing α-peak emission. This implies that PETMP is disrupting the formation of regions of coherent electronic interaction in LFPene while simultaneously providing better ET from dioxane to LFPene. The second trend is one in which lower concentrations of PETMP change the LFPene emission more significantly than do higher. This may suggest that at higher PETMP concentrations PETMP interacts to a lesser degree with both solvent and

LFPene. One possibility is that of PETMP migration to PETMP-rich regions of the solution where suppression of α and enhancement of δ/β is not possible.

B-Series:

In order to isolate ratiometric effects from the effect of PETMP addition in the P-series, and to compare with trends observed in the L-series, a series of LFPene-PETMP blends with a constant ratio of 2:1 were investigated as a dilution series (**B4**-**B1**) in 1,4-dioxane.

Spectra of the B-series have similar features to the L-series spectra with the same LFPene concentration. However, two subtle differences between **B3** and **L3** can be seen with the onset of solvent emission. First, in the emission spectra from 260 nm excitation, it can be observed that the **B3** γ-peak has a greater intensity than the corresponding emission in **L3**. This stands in contrast to the observation of increased ET at high LFPene concentrations and low PETMP concentrations. This finding confirms that the ratiometrics of the LFPene-PETMP blend are more significant to ET from solvent to LFPene than are moderate changes in concentration. The second difference that is notable when comparing **B3** and **L3** is the larger blue-shift in δ seen in **B3**. This displays that lowering the concentration of the B-series at a constant LFPene-PETMP ratio more greatly disrupts LFP-LFP interactions than does dilution alone.

Implications of Emission Trends for Synthesis and Microscopy:

In order to understand and assign domain composition of crosslinked film microstructures, LFPene emission was quantified by peak deconvolution from extracted excitation spectra at 380 nm emission and emission spectra at 260 nm excitation (Figures 5-2, 5-3 and 5-4). Fitting was performed with Origin 8 Pro software using multipeak Gaussian curves (LRS 0.9993 +/- 0.0001, Chi Sq. 12 +/- 1). The integrated values were adjusted for concentration and compared to **L4** emission (I=1). The relative emissivity/mole LFPene for each sample is provided in Table 5-1. Raw and deconvoluted spectra for the three dilution series are presented in the supporting information.

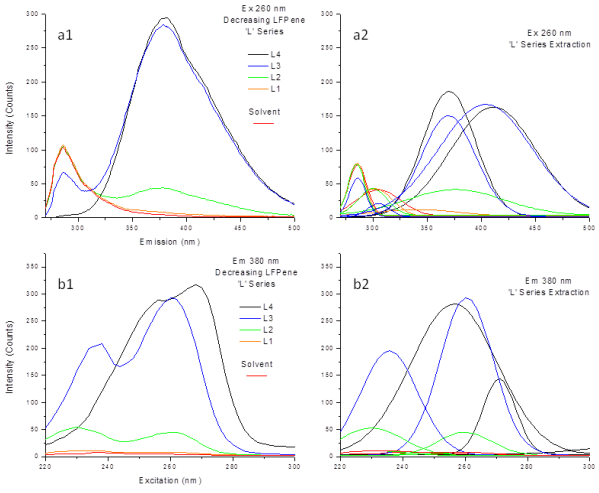

Figure 5-2. 260 nm Emission (a1) and 380 nm Excitation (b1) Spectra of **L4-L1** and **S**. Peak extractions for both the emission (a2) and excitation (b2) are provided.

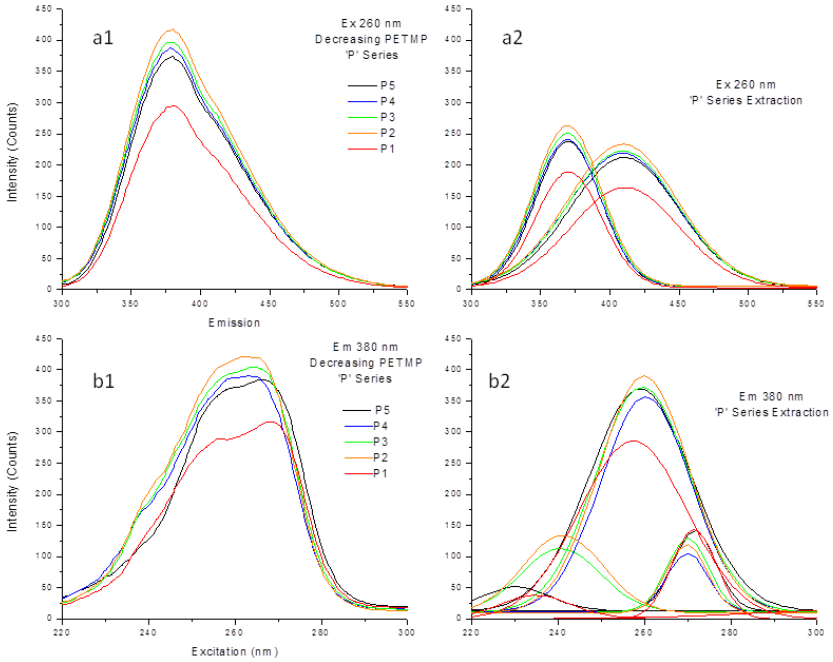

Figure 5-3. 260 nm Emission (a1) and 380 nm Excitation (b1) Spectra of **P5-P1**. Peak extractions for both emission (a2) and excitation (b2) are provided.

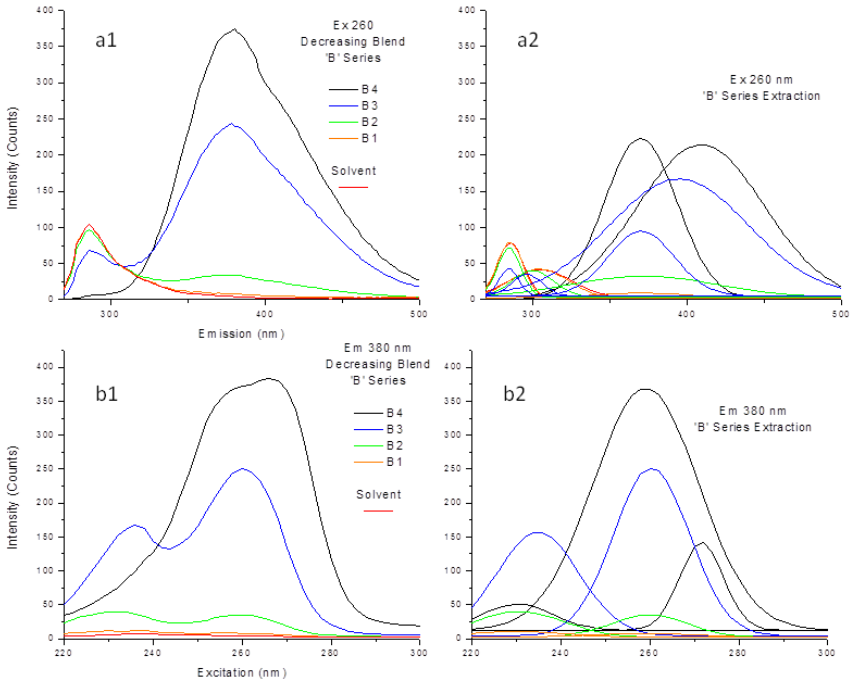

Figure 5-4. 260 nm Emission (a1) and 380 nm Excitation (b1) Spectra of **B4-B1** and **S**. Peak extractions for both the emission (a2) and excitation (b2) are provided.

The emission spectra of both the PFS and co-monomer **2** at 1 wt% in dioxane showed both β- and δ- peak emission with no visible α-peak emission. This further supports the claim that α-peak emission is the direct result of LFPene conformational changes and not simple aggregation. PFS emission was 20 times greater than that observed for the co-monomer, indicating that all fluorescence studies probed largely the PFS component of the LFPene system. The relative emission profiles of PFS and co-monomer **2** provide us with a method for assessing the degree of reaction *in situ* for the

generation of the intermediate pre-monomer, **1**. While a calibration curve would be needed, the sensitivity and availability of fluorescence measurements when compared to IR or Raman techniques makes the decrease in β-peak/δ-peak emission a viable tool for monitoring larger production scale processes.

It should also be noted that monitoring the amount of α-peak emission can provide information regarding the degree or aggregation/ordering in pre-gels. These emission profile changes also provide kinetic information on cure processes that are too fast to observe by solid-state NMR or chromatographic techniques.

In order to predict microdomain fluorescence signals at 380 nm in LFPene-PETMP coatings from deep UV excitation, emission of the L-series (no PETMP) was compared to the B-series to extrapolate the anticipated solid state behavior of the two systems. This was accomplished by log-log data fitting of the two series and extrapolating to 100% LFPene in the L-series and 67% LFPene in the B-series. Calculated intensities for the two systems in the solid state predict the 2:1 blend polymer to have an intensity of 2.4 +/- 0.4 relative to the normalized pure LFPene (I = 1 +/- 0.3).

This finding heavily informs assessment of microstructure on the film surface *via* fluorescence microscopy. B-series-like regions where the 2:1 ratio is maintained will be roughly 2.4 times brighter than pure LFPene regions. The emission trends from P-series also give information regarding concentration gradients and should allow for well informed microscale assignment of chemical composition based on emission. These results provide the following trend based on the LFPene:PETMP ratio:

PETMP << low ratio < pure LFPene < moderate ratio < high ratio

Ultimately, this provides an understanding of the microscale disorder on the anti-biofouling surface. It reasonably allows for identification of the relative concentrations of LFPene and PETMP across the surface from fluorescence microscopy where 380 nm emission is selected. While this may be useful in terms of assessing the degree of heterogeneity observed for a given formulation/processing regime, it also allows for the identification of which regions tend to have higher fouling or lower degrees of fouling-release directly *via* fluorescence microscopy. These assessments can then be used to make informed decisions regarding ratiometrics, cure chemistry and cure conditions. In a similar fashion, relative α-peak emission with excitation at ~400 nm and emission collection at ~475 nm can be used to determine relative amounts of LFPene subunit ordering.

5.5.3 Fluorescence Microscopy and Biofouling Characterization

Micrographs of the **LP**, **LH** and **PH** surfaces after BSA exposure are presented in Figure 5-5, along with an intensity profile for the three systems under identical excitation and collection conditions. The **LP** surface displayed the lowest amount of BSA uptake (avg. intensity 38 a.u.). The **LH** surface was 42% less resistant to BSA adsorption (avg. intensity 54 a.u.) while the **PH** surface was 74% less resistant (avg. intensity 68 a.u.). Qualitatively, it can be seen that **LP** and **PH** surfaces possess a

greater variation in surface binding to BSA than **LH** through uneven BSA biding distribution at the microscale.

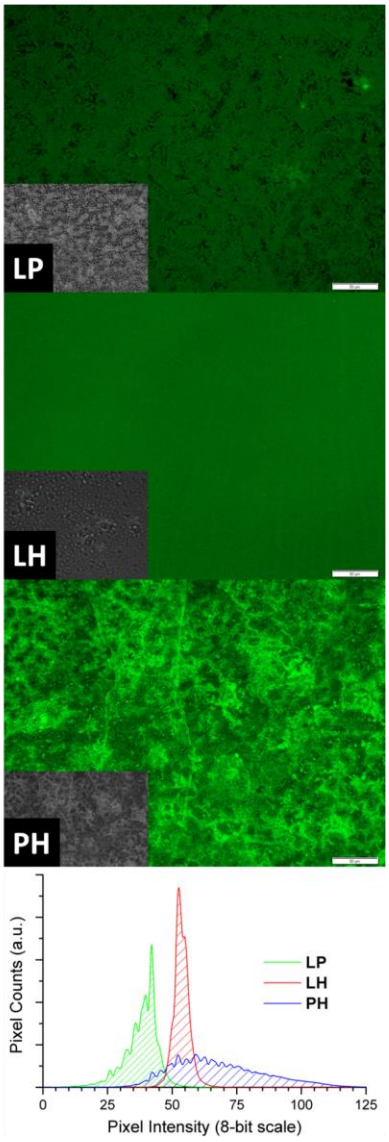

Figure 5-5. Fluorescence Micrographs of BSA Adsorption. Phase contrast images (as insets); intensity histograms (bottom); scale bar is 50 μm.

5.5.4 Infrared Spectroscopy

Spectra for the L-, B- and P-series show only nominal changes in IR absorption when compared to the dioxane spectra (Figure 5-6). The **LP**, **LH**, **PH**, LFPene and PETMP spectra show a marked difference, specifically in the region of S-H stretching (~2570 cm^{-1}) and the C=R sp^2 region (1450-1750 cm^{-1}) (Figure 5-7). Specifically, it can be observed that the **PH** sample does not contain fully reacted thiol groups while the S-H signal is missing in both the **LP** and **LH** system. Additionally, the C=C stretch at ~1650 cm^{-1} can be observed for both the **LP** and **LH** systems and not at all for the **PH** surface. This provides two insights into the thiol-ene chemistry of the **LP** system and how blend ratios may play a role in physical character and anti-biofouling character. First, the 2:1 ratio of LFPene to PETMP in the LP surface is not stoichiometrically ideal in terms of thiol consumption. This implies that a more durable film (higher extent of crosslinking) is possible with decreased PETMP perhaps more subtle, repercussion is that the fouling of the **PH** surface was significantly higher than either the **LH** or **LP** surface, indicating that consumption of the thiol functional groups may be critical to enhanced anti-biofouling properties.

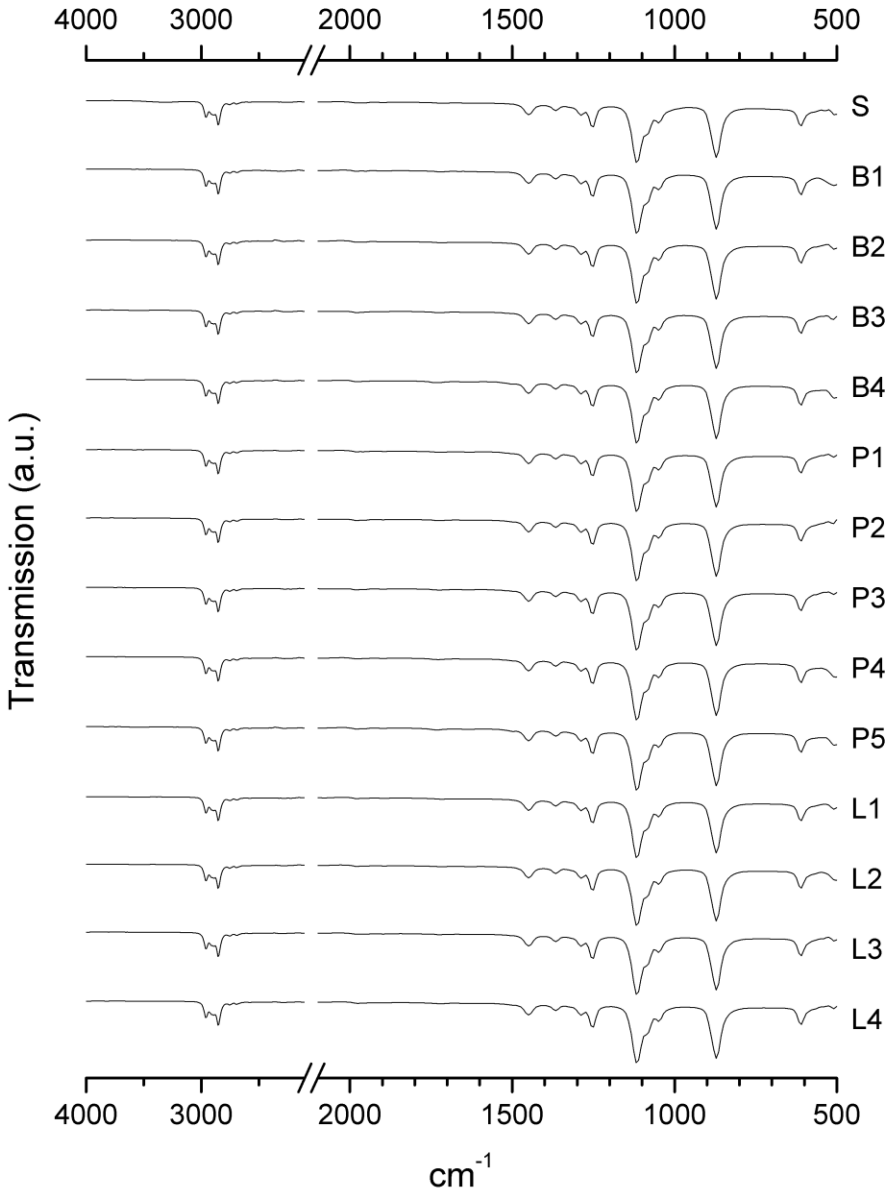

Figure 5-6. FTIR Spectra for L-, B-, and P-Series.

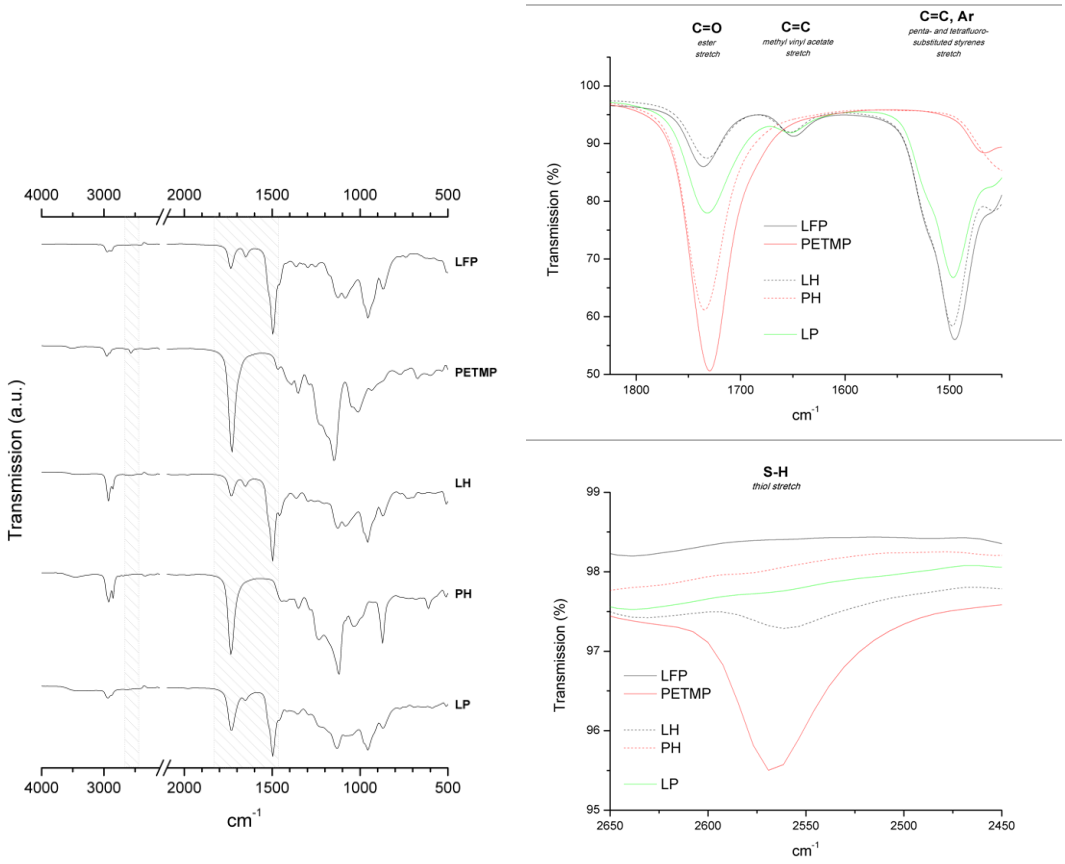

Figure 5-7. FTIR spectra for **LP**, **LH** and **PH** surfaces and LFPene and PETMP components. Full spectra (left); sp^2 C fingerprint region (upper right); S-H fingerprint region (lower right).

5.5.5 Atomic Force Microscopy and Surface Force Spectroscopy

In order to fully understand how the LFPene and PETMP interact, atomic force microscopy (AFM) was performed on the **LP**, **LH** and **PH** surfaces in conjunction with two forms of force spectroscopy, modulus mapping and adhesion force mapping. A summary of these findings is presented in Table 5-2.

The **LP** surface was investigated at 100 μm^2, 25 μm^2 and 1 μm^2 in order to observe any contrast of surface response with change in topography at the micro-, meso- and nanoscale. The **LH** and **PH** surfaces were also investigated at the 25 μm^2 scale for comparison to the **LP** system. Force curves of the AFM tip-to-surface approach and release were fitted to provide mapping of surface modulus and the force of adhesion. Topographic micrographs as well as the force spectra 3D overlays on the topography can be found in Figures 5-8 and 5-9, respectively.

The surface roughness is a full order of magnitude greater in the **LP** system than that of the **LH** or **PH** systems. **LP** exhibits both micro- and nanoscale features, whereas **LH** possesses largely nanoscale disorder and **PH** displays some very shallow (<70 nm) microscale features. From this, it can be taken that neither the PETMP nor the LFPene components of the system alone are capable of high levels of surface complexity when crosslinked with a small linear molecule. However, these observations alone do not inform us about the chemical or physical properties of these surfaces.

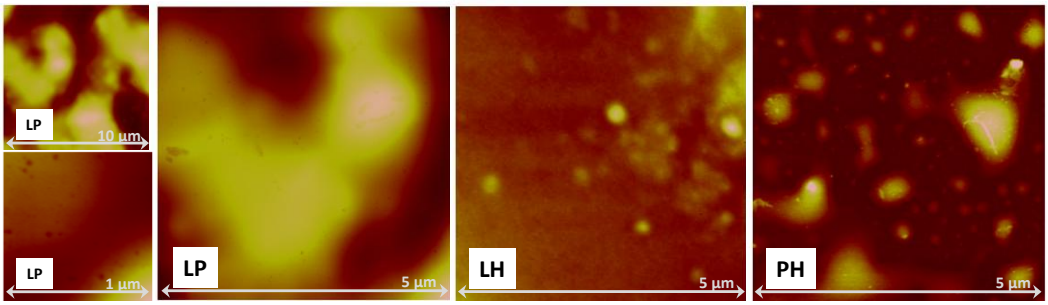

Figure 5-8. Topographic AFM micrographs of **LP**, **LH** and **PH** surfaces.

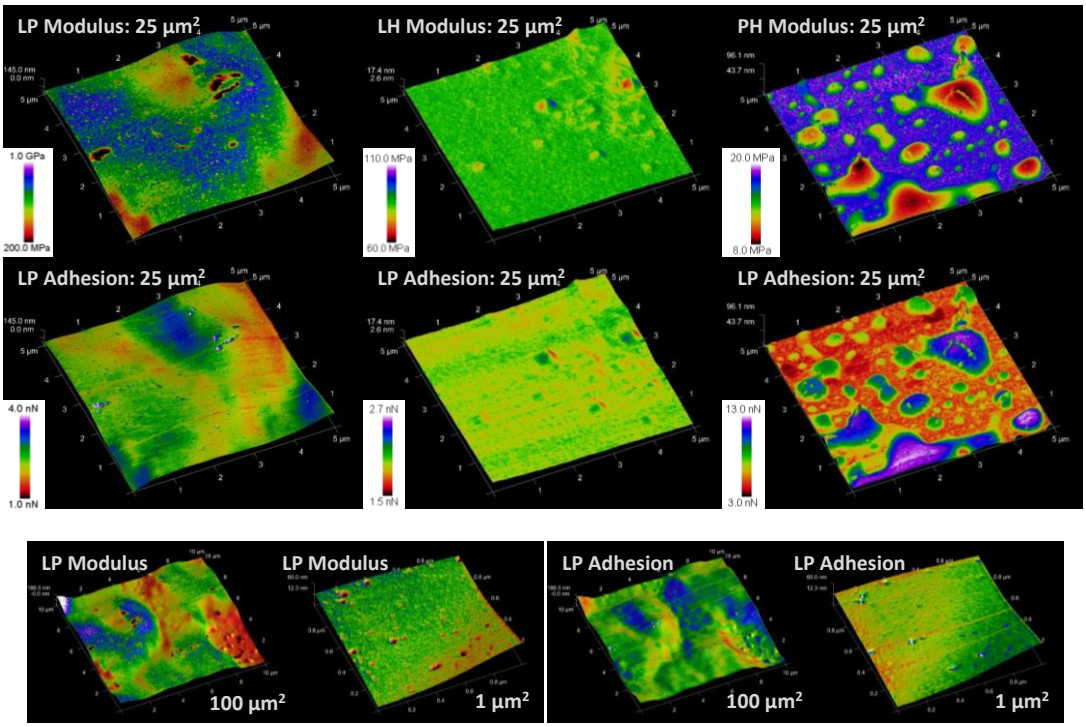

Figure 5-9. Force spectrographs mapped on to surface topography for **LP**, **LH** and **PH**.

Force spectroscopy maps of these surfaces reveal significant differences in the mechanical properties and the surface energy (*e.g.* adhesion forces). Specifically, the **LP** surface has a Young‟s Modulus that is 7 times greater than the **LH** and 35times greater than the **PH** surfaces, with about 50 times greater variation in surface modulus. These results inform us to the nature of the surface networks and provide several insights into the contribution of each component to surface ruggedness. First, comparison of the **LH** and **PH** films show that the LFPene contribution to surface modulus is significantly greater than is the PETMP contribution. Second, the complexity (modulus RMS) of the **LH** and **PH** surface networks is severely limited compared to the **LP** surface. Finally, this allows us to predict that in systems where thiol-ene "click" chemistries are used to crosslink a fluoropolymer composite, the use of molecules with more than two reactive sites generates a greatly increased modulus over blends with constituents that are bi-functional. In turn, this provides a degree of control over mechanical character where incorporation of linear components in the matrix may provide a full spectrum of surface moduli tailored to the form factor needs for a given application.

The force of surface adhesion also provides insight into the structure- function character of these surfaces. Specifically, it can be observed that the **LP** and **LH** have similar surface energies with **LH** being slightly lower energy. The **PH**, having a preponderance of ester functionality in its matrix, displays surface energy three times higher than the LFPene-rich samples. In total, this indicates that the primary surface chemistry of the **LP** is LFPene with virtually no contribution from PETMP. A linear

combination of **LH** and **PH** adhesion energies provides a 98% LFPene-like surface character in the **LP** system.

Observing the **LP** surface at various scales also reveals that the surface contains microdomains which mimic the PETMP microstructures but which express LFPene-rich surface chemistries and higher moduli (**LP** 100 μm^2 micro/spectrographs). This suggests that the microdomains possess both highly crosslinked surfaces and sub-dermal PETMP rich regions. At small scales (**LP** 1 μm^2 micro/spectrographs), it can be observed that this is in no way a discrete transition but is rather a gradient of the network‟s blended character.

In total, the use of roughness analysis and nanoscale force spectroscopies showed that these systems are readily characterized physically and chemically at the nano- and microscales. This form of characterization also provides a rapid assessment of the tunablility and component contribution to the surface character.

Table 5-2. Atomic Force Microscopy and Force Spectroscopy of **LP**, **LH** and **LP** Surfaces. Γz: total height range. E: Young‟s modulus. Adhesion force: tip sample interaction strength, corrected for penetration and tip geometry. RMS: root mean-squared variation of a given property over the area measured. Reported for a 25 um^2 region.

Surface	**Δz (nm)**	**RMS_z (nm)**	**E (MPa)**	**RMS_E (MPa)**	**Adhesion (nN)**	**RMS_{adh} (nN)**
LP	294	56	552	152	2.31	0.4
LH	30	3	84	3	2.0	0.8
PH	71	7	16	3	6.6	2.3

5.5.6 PeakForce™ Quantitative Nanomechanical Mapping (QNM™) Atomic Force Microscopy

Atomic force microscopy (AFM) measurements were taken using a Bruker Multimode 8 system in PeakForce™ tapping mode. This imaging method also provides direct surface maps of modulus, dispersion, deformation and adhesion. In brief, the PeakForce™ QNM™ imaging mode that uses a modified Hertzian model, the DMT model (Equation 5-1), to directly extract a reduced Young‟s modulus (E_r). The DMT model takes into account surface-tip interactions neglected in the Hertz model.

$$E_r = \frac{3(F_t - F_a)}{4\sqrt{Rd^3}}$$

Equation 5-1. DMT Model.

In Equation 5-1 for the DMT reduced Young‟s Modulus: F_t is the force on the probe tip, F_a is the adhesive force between the probe tip and the sample, R is the working tip radius, and d is the depth of surface deformation below the zero-force contact point. The reduced Young‟s modulus is related to the sample modulus by Equation 5-2 and reduces to Equation 5-3 where the modulus of the probe tip is much greater than the sample being measured.

$$\frac{1}{E_r} = \frac{(1-v^2)}{E} - \frac{(1-v_t^2)}{E_t}$$

Equation 5-2. Relationship between Young‟s modulus and sample modulus.

$$\frac{1}{E_r} \cong \frac{(1-v^2)}{E}$$

Equation 5-3. Reduction of Equation 5-2.

This is where v is the sample Poisson‟s ratio, v_t is the probe tip Poisson‟s ratio, E_t is the probe tip modulus and E is the sample modulus. Force curve fitting after tip contact provides a reduced modulus value which can then be converted to a Young‟s modulus using a sample surface Poisson‟s ratio of 0.3 for samples with moduli of 1 MPa or below, 0.4 for samples with moduli of 1 GPa or above and scaling linearly between 1 MPa and 1 GPa. The difference in force curve minima during approach and retraction provides adhesion force. The absolute minimum in tip Z position after contact dictates deformation. Finally, the hysteresis in the approach and retraction force curves provides dispersion values.

In these measurements a Scanasyst-air probe with nominal manufacturer mechanical specifications of k = 0.4 N/m, F = 70 kHz and tip radius = 2 nm was used. Calibration of the system was first done using two reference samples, a homogeneous PDMS film with a known modulus of 3.5 MPa and homogeneous spin-cast polystyrene film of a known modulus of 2.7 GPa in order to confirm calibration over moduli spanning ~3 orders of magnitude. Calibration was performed on each independently and the modulus values were found to be within 5% of the known value for both samples for the calibration. Calibration was further confirmed through independent determination of the probe cantilever spring constant, deflection sensitivity and tip geometry. Tip geometry/radius was determined with the use of a known surface of titanium crystals. After independent calibration, the two standards were measured again and confirmed to have Young‟s moduli within 5% of the known value.

5.5.7 Contact Angle

To identify the benchmark and model surface interactions with water, static water contact angle measurements were conducted. The benchmark surface, **LP**, had a static water contact angle of *ca.* 87°. The model surface **LH**, which crosslinked the LFPene polymer with a short hexane, was more hydrophobic, which can be attributed to the swapping of the ester linkages from the PETMP to short aliphatic chains. Reacting PETMP with a short hydrocarbon crosslinker to produce model surface **PH** revealed a more hydrophilic surface. Because **PH** is a network of two small molecules, there is a

higher density of PETMP per unit area on the surface, which interacts more favorably with water than do poly(pentafluorostyrene) units. A summary of the average contact angles and representative images are displayed in Figure 5-10. Ultimately, this supports the nanoscale adhesion force mapping results for a surface energy trend of **LH** < **LP** << **PH**.

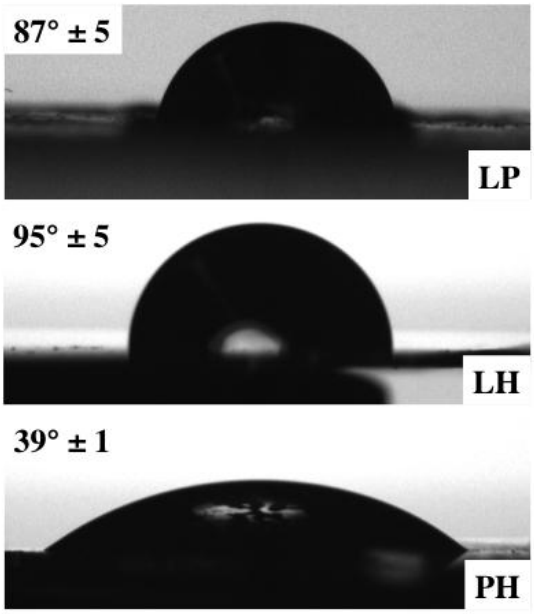

Figure 5-10. Static water contact angles for **LP**, **LH** and **PH** in the dry state.

5.5.8 Thermal Analysis

The polymer (LFPene), benchmark surface (**LP**) and two model surfaces (**LH** and **PH**) were investigated by thermogravimetric analysis to elucidate how crosslinking the components affects the bulk thermal stability (Table 5-3 and Figure 5-11). The LFPene had the highest onset of degradation temperature with a single degradation curve, *ca.* 100 °C higher than any of the three crosslinked networks, given that the polymer is partially-substituted poly(pentafluorostyrene). All three of the crosslinked networks exhibited two degradation transitions. While it is not reasonable for any of the crosslinked networks to fully emulate the pure LFPene in terms of initial onset degradation temperature, it does appear that the incorporation of PETMP allows for a crosslinked network with higher thermal stability relative to the non-PETMP containing network. This could possibly be attributed to the higher crosslink density per unit volume. However, given the residual thiol functional groups in the **LP** and **PH** networks, there is a strong possibility of vulcanization during thermal ramping. Depending on an application-driven need, this provides a potential route to bypassing concerns regarding residual SH-character with a post-cure vulcanization baking process.

The polymer (LFPene), benchmark surface (**LP**) and two model surfaces (**LH** and **PH**) were investigated by differential scanning calorimetry to identify phase transition temperatures. The pristine polymer, LFPene, has a glass transition temperature of 39 °C, lower than that of poly(pentafluorostyrene), likely due to the ethylene glycol side chains extending from the backbone allowing for increased chain

mobility at lower temperatures. Discrete glass transitions were unobservable for all crosslinked networks, further supporting the results of the force spectroscopy studies where composition gradients were observed without true, discrete microdomains. No melting transitions were observed for **LP**, **LH** or **PH** networks, indicating that amorphous, bulk films were generated. As a final note, careful inspection of the first heating cycle of the DSC traces of **LP** and **PH** revealed an enthalpy change *ca.* 130 °C, which is not observable in the subsequent cycles. This proximity to typical vulcanization temperatures (*ca*. 80-150 °C) further supports the viability of post-cure thermal treatment in order to tune the degree of thiol character, degree of crosslinking and mechanical strength, based on application needs (Figure 5-12).

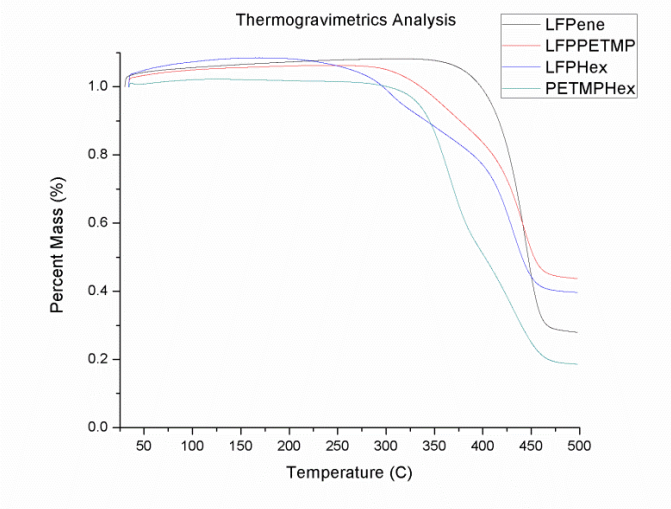

Figure 5-11. Combined thermal decomposition curves for LFPene, LFP-PETMP (**LP**), LFP-Hex (**LH**) and PETMP-Hex (**PH**).

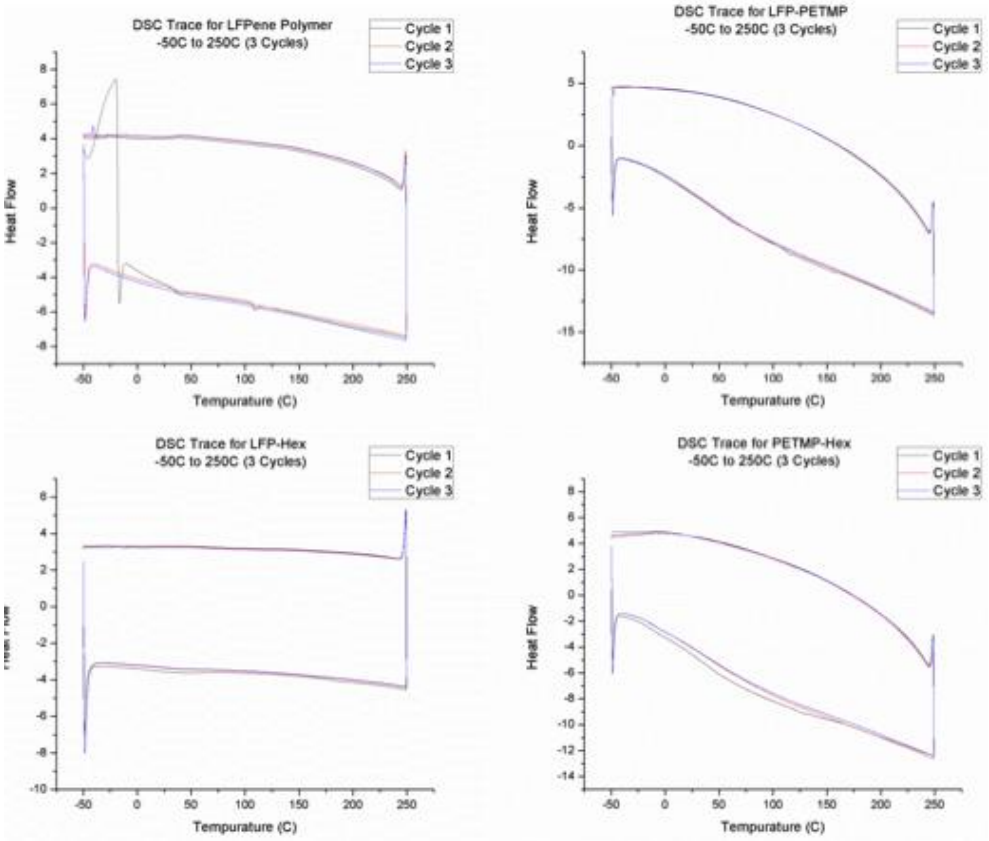

Figure 5-12. DSC traces for LFPene (upper left), LFP-PETMP (**LP**) (upper right), LFP-Hex (**LH**) (bottom left) and PETMP-Hex (**PH**) (bottom right).

Table 5-3. Summary of the thermal degradation temperatures and %mass losses for the LFPene polymer (**L**) and three crosslinked networks (**LP**, **LH** and **PH**).

	$T_{d,onset}$ (°C)	$T_{d,\ 50\%A}$ (°C)	$T_{d,\ 50\%B}$ (°C)	Mass $Loss_A$ (%)	Mass $Loss_B$ (%)	$Mass_{,Residual}$ (%)
L	412	445	-	74	-	26
LP	311	358	442	29	30	41
LH	241	305	434	27	36	37
PH	335	367	435	49	32	19

5.6 Conclusions

A linear, amphiphilic fluoropolymer with pendant alkene functionality was synthesized and crosslinked into a polymeric network through photo-initiated thiol-ene chemistry to generate a benchmark, anti-biofouling surface. This benchmark surface was studied with careful attention to spectroscopic and physicochemical changes with regard to blend ratios and response of the core constituents. Coatings were established by brief exposure to UV light in the presence of a photo-initiator to rapidly establish the networks under extremely mild conditions. The synthetic methods and materials utilized were intentionally selected to be viable and accessible for a large array of synthetic venues. Microscopic disorder observed by fluorescence microscopy correlated

biomacromolecule adsorption studies to synthetic decisions, such as individual constituent contribution and composition ratios. This will inform future compositional considerations for the enhancement of biofouling inhibition. Several metrics for identification and solutions for the elimination of excess thiol content have been presented, as well as extensive discussion on residual thiol effects on surface energy, protein binding and mechanical strength. This benchmark surface presents an exceptional surface modulus (0.5 GPa) in conjunction with microscopic and nanoscopic topographical, morphological and topological features that are beneficial to the inhibition of protein binding. Future investigations of complex, heterogeneous surfaces where hydrophobic (PFS), hydrophilic (PEG, PETMP) and amphiphilic (LFPene, HBFP) chemistries are employed can take advantage of this benchmark system as both a model and a reference in terms of composition, extent of reaction physical and anti-biofouling response. This study relates component behavior at the surface to the performance and viability of the coating, with a focus towards the fine-tuning of formulation for a variety of application needs.

5.7 Acknowledgements

Financial support was provided by the Office of Naval Research under Grant Number N00014-10-1-0527, the National Science Foundation Research Experiences for Undergraduates (NSF REU) Grant No. CHE-1062840 and the W. T. Doherty-Welch Chair in Chemistry, Grant No. A-0001. We also thank the Texas A&M University Laboratory for Biological Mass Spectrometry for small molecule mass spectral analysis.

CHAPTER VI

CONCLUSIONS

This body of work has expanded on the synthesis of hyperbranched fluoropolymers (HBFPs) studied in the Wooley Lab and has produced a matrix of crosslinked networks with poly(ethylene glycols) (PEGs) that have shown promising anti-biofouling responses with improved mechanical properties. An additional mode of biofouling prevention was incorporated onto HBFPs crosslinked with PEG (HBFP-PEG) as a unique strategy demonstrating synergy between two modes of action. Installation of reversible crosslinks to prevent against mechanical failure was studied and is a strategy that can be translated to other systems. Network production efficiency has been realized through the use of thiol-ene chemistry and a set of metrics for analyzing and comparing complex, heterogeneous surfaces has been produced.

HBFP$^{(III)}$-PEG was advanced through variation in the chemical composition of the HBFP component and in the amount of PEG present in the formulation with a focus on optimization as anti-biofouling marine coatings. Bulk properties, including glass transition temperature, thermal degradation temperature, and Young‟s modulus was varied through comonomer stoichiometry during the polymerization and during formulation of the crosslinked network, offering insight to the versatility of these materials. Unexpectedly, these surfaces presented a more hydrophobic surface after swelling in water. A dynamic reorganization event was shown to be responsible, where

the PEG-rich domains reordered to sequester water and the HBFP was forced to the surface. This migration was verified by secondary ion mass spectrometry (SIMS) by observing a larger amount of fluorinated species post-water swelling. Surfaces replicated for biological assays had varied performance against marine microorganisms based on polymer composition and blend ratios. The HBFP$^{(III)}$-PEG surfaces tested almost entirely resisted the settlement of barnacle cyprids, easily cleaned of diatom proliferation *versus* a known fouling-release standard, and, unfortunately, were easily colonized by green algae spores which resisted removal. These results speak to the degree of difficulty in producing a single surface that entirely resists a large spectrum of biological life.

A dual-mode, passive and active anti-biofouling surface was generated by the decoration of highly-complex surfaces with a settlement deterrent moiety. Extensive characterization studies were performed to identify surface features that would inhibit fouling, confirm the covalent grafting of noradrenaline (NA) on the substrate, and verify the activity of the NA working in parallel with the HBFP$^{(III)}$-PEG surface. AFM and contact angle experiments revealed a treacherous, low surface energy terrain. SIMS was a useful tool to quantify the substitution reaction, offering two signals to monitor: the relative increase in nitrogen containing species and the relative decrease in bromine containing species. Oyster hemocytes incubated on the modified surfaces were found to deteriorate from apoptosis, a sign that the NA maintained its biological activity after grafting. In all, barnacle cyprids were found to interact with the modified surfaces less when compared to the unmodified HBFP$^{(III)}$-PEG, and neither surface suffered from

cyprid settlement and attachment, corroborating that each mode of anti-biofouling was working in tandem.

The covalent crosslinks in HBFP$^{(I)}$-PEG were substituted for Diels-Alder (DA) moieties to install healable crosslinks throughout the network that are capable of repair prior to mechanical failure. In order to optimize the reaction conditions necessary to catalyze the healing, small molecule and linear polymer model studies were performed and analyzed. In solution, the controlled reversibility of the DA bonds was demonstrated. Coatings of DA-HBFP-PEG were cast and analyzed by AFM and contact angle and found to have similar surface properties as the covalent counterpart, HBFP$^{(I)}$-PEG. Protein adsorption resistance was confirmed by behavior similar to HBFP$^{(I)}$-PEG and future studies will investigate the interaction of marine microorganisms with the surface with the anticipation of similar results. Damage from light abrasions was easily rectified from the surface in *ca*. 30 min but deeper gashes only partially healed after 3 h. Future healing experiments will look into localized heating to promote DA bond breaking, bulk flow to fill in the gaps, and localized heating for bond reformation.

A linear fluoropolymer analog of HBFP$^{(III)}$ was synthesized that expressed pendant alkene functionality (LFPene) to be crosslinked with pentaerythritol *tetrakis*(3-mercaptopropionate) (PETMP) into benchmark anti-biofouling networks *via* thiol-ene chemistry. Spectroscopic changes due to constituents mixing was analyzed and extrapolated to trends in the autofluorescence of materials in the solid state obtained from those constituents. Importantly, this will lead to the identification of microdomain blend ratios that inhibit fouling best (to be replicated throughout a surface) or foul easily

(to be avoided). The benchmark was compared to two test surfaces which largely expressed either LFPene or PETMP, and it was found that mixing of LFPene and PETMP led to the best protein adsorption resistance and the highest overall (with the greatest variance of) surface modulus. Residual thiol functionality was identified on the surface by using attenuated total reflectance Fourier-Transform infrared (ATR-FTIR) spectroscopy, and evidence of free thiols in the bulk was discovered by observation of vulcanization during DSC experiments. This will lead to improvements in processing in future batches, using a post-cure heating to vulcanize, enhance bulk mechanical properties, and potentially reduce the surface free thiols on which proteins would prefer to adsorb.

This body of work would not have been completed in its current form without the extensive collaborative efforts that facilitated the breadth of experiments conducted. This dissertation spanned synthetic, analytical and physical chemistry, surface science, materials science and biology. The work conducted in Chapter III was a shared vision with the Mount lab. The unusual increase in surface hydrophobicity upon swelling in water was an affect that could only be analyzed with equipment outside of the Wooley Lab, and the Schweikert lab was able to confirm both hypotheses. The biology experts from the Callows and Clare labs were able to closely assess the settlement behavior of marine microorganisms during their interactions with the surfaces and provide feedback that advanced the overall design. Overall, this dissertation came to fruition from the gracious effort of collaborators.

In all, this dissertation will aid in the future optimization of the anti-biofouling ability of HBFP-PEG, and its derivatives, to produce coatings that are environmentally-benign and mechanically viable for translation towards commercial implementation. The full optimization of these systems has yet to be achieved; fine-tuning of properties is still desired. For instance, shelf stability of HBFP has been a concern and elemental analysis of HBFP samples that were 1+ years old revealed actual bromine levels that were as much as half of the expected theoretical values. This could be attributed to eliminated benzyl bromides and bromoacetyls and translates to less chain-end functionality, potentially resulting in weaker crosslinked networks. Also, the formulation of HBFP-PEG in its current form is not a cost-effective material to coat large areas (*e.g.* destroyer or battleship hulls) but does provide the basis for a strategy to prevent biological fouling. Future HBFP-PEG derivatives will explore low-cost HBFP and PEG substitutes that can still achieve complex, heterogeneous surfaces upon crosslinking. Additionally, these experiments were conducted on glass microscope slides. Although this protocol was appropriate for laboratory assays, glass is not an accurate representation of the types of substrates that require anti-biofouling coatings in the marine environment. Current experiments are evaluating the use of base coats, for example Intergard 264 (International Paint), as a tie-coat to affix HBFP-PEG to a steel substrate. In all, this body of work will impact how next-generation materials are formulated, characterized and modified to generate enhanced marine anti-biofouling coatings.

REFERENCES

(1) McElvany, S.; http://www.onr.navy.mil/media-center/fact-sheets/biofouling-prevention.aspx, hull coatings fouling facts viewed, accessed in August, 2011.

(2) Yebra, D. M.; Kiil, S.; Dam-Johansen, K. Antifouiling Technology - Past, Present and Future Steps Towards Efficient and Environmentally Friendly Antifouling Coatings. *Prog. Org. Coat.* **2004**, *50*, 75-104.

(3) Zhou, J.; Zhu, X.-S.; Cai, Z.-H. Tributyltin Toxicity in Abalone (Haliotis Diversicolor Supertexta) Assessed by Antioxidant Enzyme Activity, Metabolic Response, and Histopathology. *J. Hazard. Mater.* **2010**, *183*, 428-433.

(4) Schultz, M. P.; Bendick, J. A.; Holm, E. R.; Hertel, W. M. Economic Impact of Biofouling on a Naval Surface Ship. *Biofouling* **2011**, *27*, 87-98.

(5) Srinivasan, M.; Swain, G. W. Managing the Use of Copper-Based Antifouling Paints. *Environ. Mange.* **2007**, *39*, 423-441.

(6) Ytreberg, E.; Karlsson, J.; Eklund, B. Comparison of Toxicity and Release Rates of Cu and Zn from Anti-Fouling Paints Leached in Natural and Artificial Brackish Seawater. *Sci. Total. Environ.* **2010**, *408*, 2459-2466.

(7) Thomas, K. V.; Brooks, S. The Environmental Fate and Effects of Antifouling Paint Biocides. *Biofouling* **2010**, *26*, 73-88.

(8) Schultz, M. P. Effects of Coating Roughness and Biofouling on Ship Resistance and Powering. *Biofouling* **2007**, *23*, 331-341.

(9) Krishnan, S.; Wang, N.; Ober, C. K.; Finlay, J. A.; Callow, M. E.; Callow, J. A.; Hexemer, A.; Sohn, K. E.; Kramer, E. J.; Fischer, D. A. Comparison of the Fouling Release Properties of Hydrophobic Fluorinated and Hydrophilic Pegylated Block Copolymer Surfaces: Attachment Strength of the Diatom Navicula and the Green Alga Ulva. *Biomacromolecules* **2006**, *7*, 1449-1462.

(10) Yarbrough, J. C.; Rolland, J. P.; DeSimone, J. M.; Callow, M. E.; Finlay, J. A.; Callow, J. A. Contact Angle Analysis, Surface Dynamics, and Biofouling Characteristics of Cross-Linkable, Random Perfluoropolyether-Based Graft Terpolymers. *Macromolecules* **2006**, *39*, 2521-2528.

(11) Youngblood, J. P.; Andruzzi, L.; Ober, C. K.; Hexemer, A.; Kramer, E. J.; Callow, J. A.; Finlay, J. A.; Callow, M. E. Coatings Bbased on Side-Chain Ether-Linked Poly(Ethylene Glycol) and Fluorocarbon Polymers for the Control of Marine Biofouling. *Biofouling* **2003**, *19*, 91-98.

(12) Dimitriou, M. D.; Zhou, Z.; Yoo, H.-S.; Killops, K. L.; Finlay, J. A.; Cone, G.; Sundaram, H. S.; Lynd, N. A.; Barteau, K. P.; Campos, L. M.; Fischer, D. A.; Callow, M. E.; Callow, J. A.; Ober, C. K.; Hawker, C. J.; Kramer, E. J. A General Approach to Controlling the Surface Composition of Poly(Ethylene Oxide)-Based Block Copolymers for Antifouling Coatings. *Langmuir* **2011**, *27*, 13762-13772.

(13) Wang, Y.; Pitet, L. M.; Finlay, J.; Brewer, L. H.; Cone, G.; Betts, D. E.; Callow, M. E.; Callow, J. A.; Wendt, D. E.; Hillmeyer, M. A.; DeSimone, J. M. Investigation of the Role of Hydrophilic Chain Length in Amphiphilic

Perfluoropolyether/Poly(Ethylene Glycol) Networks: Towards High-Performance Antifouling Coatings. *Biofouling* **2011**, *27*, 1139-1150.

(14) Bartels, J. W.; Cheng, C.; Powell, K. T.; Xu, J. Q.; Wooley, K. L. Hyperbranched Fluoropolymers and Their Hybridization into Complex Amphiphilic Crosslinked Copolymer Networks. *Macromol. Chem. Phys.* **2007**, *208*, 1676-1687.

(15) Rydholm, A. E.; Bowman, C. N.; Anseth, K. S. Degradable Thiol-Acrylate Photopolymers: Polymerization and Degradation Behavior of an in Situ Forming Biomaterial. *Biomaterials* **2005**, *26*, 4495-4506.

(16) Unsworth, L. D.; Sheardown, H.; Brash, J. L. Protein Resistance of Surfaces Prepared by Sorption of End-Thiolated Poly(Ethylene Glycol) to Gold: Effect of Surface Chain Density. *Langmuir* **2005**, *21*, 1036-1041.

(17) Ostuni, E.; Chapman, R. G.; Liang, M. N.; Meluleni, G.; Pier, G.; Ingber, D. E.; Whitesides, G. M. Self-Assembled Monolayers That Resist the Adsorption of Proteins and the Adhesion of Bacterial and Mammalian Cells. *Langmuir* **2001**, *17*, 6336-6343.

(18) Zhang, Z.; Finlay, J. A.; Wang, L.; Gao, Y.; Callow, J. A.; Callow, M. E.; Jiang, S. Polysulfobetaine-Grafted Surfaces as Environmentally Benign Ultralow Fouling Marine Coatings. *Langmuir* **2009**, *25*, 13516-13521.

(19) Aldred, N.; Clare, A. S. The Adhesive Strategies of Cyprids and Development of Barnacle-Resistant Marine Coatings. *Biofouling* **2008**, *24*, 351-363.

(20) Finlay, J. A.; Bennett, S. M.; Brewer, L. H.; Sokolova, A.; Clay, G.; Gunari, N.; Meyer, A. E.; Walker, G. C.; Wendt, D. E.; Callow, M. E.; Callow, J. A.;

Detty, M. R. Barnacle Settlement and the Adhesion of Protein and Diatom Microfouling to Xerogel Films with Varying Surface Energy and Water Wettability. *Biofouling* **2010**, *26*, 657-666.

(21) Gunari, N.; Brewer, L. H.; Bennett, S. M.; Sokolova, A.; Kraut, N. D.; Finlay, J. A.; Meyer, A. E.; Walker, G. C.; Wendt, D. E.; Callow, M. E.; Callow, J. A.; Bright, F. V.; Detty, M. R. The Control of Marine Biofouling on Xerogel Surfaces with Nanometer-Scale Topography. *Biofouling* **2011**, *27*, 137-149.

(22) Majumdar, P.; Crowley, E.; Htet, M.; Stafslien, S. J.; Daniels, J.; VanderWal, L.; Chisholm, B. J. Combinatorial Materials Research Applied to the Development of New Surface Coatings Xv: An Investigation of Polysiloxane Anti-Fouling/Fouling-Release Coatings Containing Tethered Quaternary Ammonium Salt Groups. *ACS Comb. Sci.* **2011**, *13*, 298-309.

(23) Martinelli, E.; Sarvothaman, M. K.; Alderighi, M.; Galli, G.; Mielczarski, E.; Mielczarski, J. A. Pdms Network Blends of Amphiphilic Acrylic Copolymers with Poly(Ethylene Glycol)-Fluoroalkyl Side Chains for Fouling-Release Coatings. I. Chemistry and Stability of the Film Surface. *J. Polym. Sci., Part A: Polym. Chem.* **2012**, *In Press*.

(24) Martinelli, E.; Suffredini, M.; Galli, G.; Glisenti, A.; Pettitt, M. E.; Callow, M. E.; Callow, J. A.; Williams, D.; Lyall, G. Amphiphilic Block Copolymer/Poly(Dimethylsiloxane) (Pdms) Blends and Nanocomposites for Improved Fouling-Release. *Biofouling* **2011**, *27*, 529-541.

(25) Feng, S. J.; Wang, Q.; Gao, Y.; Huang, Y. G.; Qing, F. L. Synthesis and Characterization of a Novel Amphiphilic Copolymer Capable as Anti-Biofouling Coating Material. *J. Appl. Polym. Sci.* **2009**, *114*, 2071-2078.

(26) Brady, R. F.; Singer, I. L. Mechanical Factors Favoring Release from Fouling Release Coatings. *Biofouling* **2000**, *15*, 73-81.

(27) Genzer, J.; Efimenko, K. Recent Developments in Superhydrophobic Surfaces and Their Relevance to Marine Fouling: A Review. *Biofouling* **2006**, *22*, 339-360.

(28) Hoipkemeier-Wilson, L.; Schumacher, J. F.; Carman, M. L.; Gibson, A. L.; Feinberg, A. W.; Callow, M. E.; Finlay, J. A.; Callow, J. A.; Brennan, A. B. Antifouling Potential of Lubricious, Micro-Engineered, Pdms Elastomers against Zoospores of the Green Fouling Alga Ulva (Enteromorpha). *Biofouling* **2004**, *20*, 53-63.

(29) Scardino, A. J.; Zhang, H.; Cookson, D. J.; Lamb, R. N.; de Nys, R. The Role of Nano-Roughness in Antifouling. *Biofouling* **2009**, *25*, 757-767.

(30) Bartels, J. W.; Imbesi, P. M.; Finlay, J.; Fidge, C.; Ma, J.; Seppala, J. E.; Nystrom, A. M.; Mackay, M. E.; Callow, J. A.; Callow, M. E.; Wooley, K. L. Antibiofouling Hybrid Dendritic Boltorn/Star Peg Thiol-Ene Cross-Linked Networks. *ACS Appl. Mater. Interfaces* **2011**, *3*, 2118-2129.

(31) Ma, J.; Bartels, J. W.; Li, Z.; Zhang, K.; Cheng, C.; Wooley, K. L. Synthesis and Solution-State Assembly or Bulk State Thiol-Ene Crosslinking of Pyrrolidinone- and Alkene-Functionalized Amphiphilic Block Fluorocopolymers: From Functional Nanoparticles to Anti-Fouling Coatings. *Aust. J. Chem.* **2010**, *63*, 1159-1163.

(32) Bartels, J. W.; Billings, P. L.; Ghosh, B.; Urban, M. W.; Greenlief, C. M.; Wooley, K. L. Amphiphilic Cross-Linked Networks Produced from the Vulcanization of Nanodomains within Thin Films of Poly(N-Vinylpyrrolidinone)-B-Poly(Isoprene). *Langmuir* **2009**, *26*, 9535-9544.

(33) Mueller, A.; Kowalewski, T.; Wooley, K. L. Synthesis, Characterization, and Derivatization of Hyperbranched Polyfluorinated Polymers. *Macromolecules* **1998**, *31*, 776-786.

(34) Gan, D.; Mueller, A.; Wooley, K. L. Amphiphilic and Hydrophobic Surface Patterns Generated from Hyperbranched Fluoropolymer/Linear Polymer Networks: Minimally Adhesive Coatings Via the Crosslinking of Hyperbranched Fluoropolymers. *J. Polym. Sci., Part A: Polym. Chem.* **2003**, *41*, 3531-3540.

(35) Gudipati, C. S.; Finlay, J. A.; Callow, J. A.; Callow, M. E.; Wooley, K. L. The Antifouling and Fouling-Release Perfomance of Hyperbranched Fluoropolymer (Hbfp)-Poly(Ethylene Glycol) (Peg) Composite Coatings Evaluated by Adsorption of Biomacromolecules and the Green Fouling Alga Ulva. *Langmuir* **2005**, *21*, 3044-3053.

(36) Gudipati, C. S.; Greenlief, C. M.; Johnson, J. A.; Prayongpan, P.; Wooley, K. L. Hyperbranched Fluoropolymer and Linear Poly(Ethylene Glycol) Based Amphiphilic Crosslinked Networks as Efficient Antifouling Coatings: An Insight into the Surface Compositions, Topographies, and Morphologies. *J. Polym. Sci., Part A: Polym. Chem.* **2004**, *42*, 6193-6208.

(37) Xu, J.; Bartels, J. W.; Bohnsack, D. A.; Tseng, T.-C.; Mackay, M. E.; Wooley, K. L. Hierarchical Inorganic-Organic Nanocomposites Possessing Amphiphilic

and Morphological Complexities: Influence of Nanofiller Dispersion on Mechanical Performance. *Adv. Funct. Mater.* **2008**, *18*, 2733-2744.

(38) Xu, J. Q.; Bohnsack, D. A.; Mackay, M. E.; Wooley, K. L. Unusual Mechanical Performance of Amphiphilic Crosslinked Polymer Networks. *J. Am. Chem. Soc.* **2007**, *129*, 506-507.

(39) Cheng, C.; Wooley, K. L.; Khoshdel, E. Hyperbranched Fluorocopolymers by Atom Transfer Radical Self-Condensing Vinyl Copolymerization. *J. Polym. Sci., Part A: Polym. Chem.* **2005**, *43*, 4754–4770.

(40) Powell, K. T.; Cheng, C.; Wooley, K. L.; Singh, A.; Urban, M. W. Complex Amphiphilic Networks Derived from Diamine-Terminated Poly(Ethylene Glycol) and Benzylic Chloride-Functionalized Hyperbranched Fluoropolymers. *J. Polym. Sci., Part A: Polym. Chem.* **2006**, *44*, 4782-4794.

(41) Berglin, M.; Wynne, K. J.; Gatenholm, P. Fouling-Release Coatings Prepared from A, Ω-Dihydroxypoly(Dimethylsiloxane) Cross-Linked with (Heptadecafluoro-1,1,2,2-Tetrahydrodecyl)Triethoxysilane. *J. Colloid Interface Sci.* **2003**, *257*, 383-391.

(42) Stafslien, S. J.; Bahr, J.; Daniels, J.; Christianson, D. A.; Chisolm, B. J. High-Throughput Screening of Fouling-Release Properties: An Overview. *J. Adhesion Sci. Technol.* **2011**, *25*, 2239-2253.

(43) Bodkhe, R. B.; Stafslien, S. J.; Cilz, N.; Daniels, J.; Thompson, S. E. M.; Callow, M. E.; Callow, J. A.; Webster, D. C. Polyurethanes with Amphiphilic Surfaces

Made Using Telechelic Functional Pdms Having Orthogonal Acid Functional Groups. *Prog. Org. Coat.* **2012**, *In Press*.

(44) Dobretsov, S.; Thomason, J. C. The Development of Marine Biofilms on Two Commercial Non-Biocidal Coatings: A Comparison between Silicone and Fluoropolymer Technologies. *Biofouling* **2011**, *27*, 869-880.

(45) Sundaram, H. S.; Cho, Y.; Dimitriou, M. D.; Finlay, J. A.; Cone, G.; WIlliams, S.; Handlin, D.; Gatto, J.; Callow, M. E.; Callow, J. A.; Kramer, E. J.; Ober, C. K. Fluorinated Amphiphilic Polymers and Their Blends for Fouling-Release Applications: The Benefits of a Triblock Copolymer Surface. *ACS Appl. Mater. Interfaces* **2011**, *3*, 3366-3374.

(46) Krishnan, S.; Weinman, C. J.; Ober, C. K. Advances in Polymers for Anti-Biofouling Surfaces. *J. Mater. Chem.* **2008**, *18*, 3405-3413.

(47) Chen, Y.; Liu, D.; He, X.; Wang, X. Atom Transfer Radical Polymerization Directly from Poly(Vinylidene Fluoride): Surface and Antifouling Properties. *J. Polym. Sci., Part A: Polym. Chem.* **2006**, *44*, 3434-3443.

(48) Imbesi, P. M.; Gohad, N. V.; Eller, M. J.; Orihuela, B.; Rittschof, D.; Schweikert, E. A.; Mount, A. S.; Wooley, K. L. Noradrenaline-Functionalized Hyperbranched Fluoropolymer Poly(Ethylene Glycol) Cross-Linked Networks as Dual-Mode, Anti-Biofouling Coatings. *ACS Nano* **2012**, *6*, 1503-1512.

(49) Benninghoven, A. Surface-Analysis by Secondary-Ion Mass-Spectrometry (Sims). *Surface Science* **1994**, *300*, 246-260.

(50) Mahoney, C. M. Cluster Secondary Ion Mass Spectrometry of Polymers and Related Materials. *Mass Spectrometry Reviews* **2010**, *29*, 247-293.

(51) Touboul, D.; Brunelle, A.; Halgand, F.; De La Porte, S.; Laprevote, O. Lipid Imaging by Gold Cluster Time-of-Flight Secondary Ion Mass Spectrometry: Application to Duchenne Muscular Dystrophy. *Journal of Lipid Research* **2005**, *46*, 1388-1395.

(52) Pinnick, V. T.; Verkhoturov, S. V.; Kaledin, L.; Bisrat, Y.; Schweikert, E. A. Molecular Identification of Individual Nano-Objects. *Analytical Chemistry* **2009**, *81*, 7527-7531.

(53) Neumann, A. W.; Good, R. J. Techniques of Measuring Contact Angles [in Surface Studies] *Journal of Surface and Colloid Science* **1979**, *11*, 31-91.

(54) Fernandez-Lima, F. A.; Eller, M. J.; Verkhoturov, S. V.; Della-Negra, S.; Schweikert, E. A. Photon, Electron, and Secondary Ion Emission from Single C-60 Kev Impacts. *Journal of Physical Chemistry Letters* **2010**, *1*, 3510-3513.

(55) Eller, M. J.; Verkhoturov, S. V.; Della-Negra, S.; Rickman, R. D.; Schweikert, E. A. Real-Time Localization of Single C-60 Impacts with Correlated Secondary Ion Detection. *Surf Interface Anal* **2010**, *43*, 484-487.

(56) Verkhoturov, S. V.; Eller, M. J.; Rickman, R. D.; Della-Negra, S.; Schweikert, E. A. Single Impacts of C60 on Solids: Emission of Electrons, Ions and Prospects for Surface Mapping. *Journal of Physical Chemistry C* **2010**, *114*, 5637-5644.

(57) Winograd, N.; Garrison, B. J. Biological Cluster Mass Spectrometry. *Annu. Rev. Phys. Chem.* **2010**, *61*, 305-322.

(58) Elbourne, P. D.; Veater, R. A.; Clare, A. S. Interaction of Conspecific Cues in Balanus Amphitrite Darwin (Cirripedia) Settlement Assays: Continued Argument for the Single-Larva Assay. *Biofouling* **2008**, *24*, 87-96.

(59) Aldred, N.; Scardino, A.; Cavaco, A.; De Nys, R.; Clare, A. S. Attachment Strength Is a Key Factor in the Selection of Surfaces by Barnacle Cyprids (Balanus Amphitrite) During Settlement. *Biofouling* **2010**, *26*, 287-299.

(60) Clare, A. S.; Thomas, R. F.; Rittschof, D. Evidence for the Involvement of Cyclic Amp in the Pheromonal Modulation of Barnacle Settlement. *J. Exp. Biol.* **1995**, *198*, 655-664.

(61) Callow, M. E.; Callow, J. A.; Pickett-Heaps, J. D.; Wetherbee, R. Primary Adhesion of Enteromorpha (Chlorophyta, Ulvales) Propagules: Quantitative Settlement Studies and Video Microscopy. *J. Phycol.* **1997**, *33*, 938-947.

(62) Cooper, S. P.; Finlay, J. A.; Cone, G.; Callow, M. E.; Callow, J. A.; Brennan, A. B. Engineered Antifouling Microtopographies: Kinetic Analysis of the Attachment of Zoospores of the Green Alga Ulva to Silicone Elastomers. *Biofouling* **2011**, *27*, 881-891.

(63) Finlay, J. A.; Fletcher, B. R.; Callow, M. E.; Callow, J. A. Effect of Background Colour on Growth and Adhesion Strength of Ulva Sporelings. *Biofouling* **2008**, *24*, 219-225.

(64) Finlay, J. A.; Callow, M. E.; Ista, L. K.; Lopez, G. P.; Callow, J. A. The Influence of Surface Wettability on the Adhesion Strength of Settled Spores of the Green Alga Enteromorpha and the Diatom Amphora. *Integr. Comp. Biol.* **2002**, *42*, 1116-1122.

(65) Makal, U.; Wynne, K. J. Water Induced Hydrophobic Surface. *Langmuir* **2005**, *21*, 3742-3745.

(66) Makal, U.; Uslu, N.; Wynne, K. J. Water Makes It Hydrophobic: Contraphilic Wetting for Polyurethanes with Soft Blocks Having Semifluorinated and 5,5-Dimethylhydanoin Side Chains. *Langmuir* **2007**, *23*, 209-216.

(67) Chen, L.-J.; Seo, J. H.; Eller, M. J.; Verkhoturov, S. V.; Shah, S. S.; Revzin, A.; Schweikert, E. A. Quantitative Label-Free Characterization of Avidin Biotin Assemblies on Silanized Glass. *Anal. Chem.* **2011**, *83*, 7173-7178.

(68) Long, C. J.; Schumacher, J. F.; Robinson II, P. A. C.; Finlay, J. A.; Callow, M. E.; Callow, J. A.; Brennan, A. B. A Model That Predicts the Attachment Behavior of Ulva Linza Zoospores on Surface Topography. *Biofouling* **2010**, *26*, 411-419.

(69) Copper Antifouling Environmental Programme, http://www.copperantifouling.com, copper accumulation facts viewed, accessed in August, 2011.

(70) Walters, L. J.; Miron, G.; Bourget, E. Endoscopic Observations of Invertebrate Larval Substratum Exploration and Settlement. *Mar. Ecol. Prog. Ser.* **1999**, *182*, 95-108.

(71) Gohad, N. V.; Shah, N. M.; Metters, A. T.; Mount, A. S. Noradrenaline Deters Marine Invertebrate Biofouling When Covalently Bound in Polymeric Coatings. *J. Exp. Mar. Biol. Ecol.* **2010**, *394*, 63-73.

(72) Woodward, I.; Schofield, C. E.; Roucoules, V.; Badyal, J. P. S. Super-Hydrophobic Surfaces Produced by Plasma Fluorination of Polybutadiene Films. *Langmuir* **2003**, *19*, 3432-3438.

(73) Sundaram, H. S.; Cho, Y.; Dimitriou, M. D.; Weinman, C. J.; Finlay, J. A.; Cone, G.; Callow, M. E.; Callow, J. A.; Kramer, E. J.; Ober, C. K. Fluorine-Free Mixed Amphiphilic Polymers Based on Pdms and Peg Side Chains for Fouling Release Applications. *Biofouling* **2011**, *27*, 589-601.

(74) Coon, S. L.; Bonar, D. B. Induction of Settlement and Metamorphosis of the Pacific Oyster, Crassostrea Gigas (Thungberg), by L-Dopa and Catecholamines. *J. Exp. Mar. Biol. Ecol.* **1985**, *94*, 211-221.

(75) Coon, S. L.; Bonar, D. B. Pharmacological Evidence That Alpha1-Adrenoceptors Mediate Metamorphosis of the Pacific Oyster, Crassostrea Gigas. *Neuroscience* **1987**, *23*, 1169-1174.

(76) Coon, S. L.; Bonar, D. B.; Weiner, R. M. Chemical Production of Cultchless Oyster Spat Using Epinephrine and Norepinephrine. *Aquaculture* **1986**, *58*, 255-262.

(77) Dahlström, M.; Lindgren, F.; Berntsson, K.; Sjögren, M.; Mårtensson, L. G. E.; Jonsson, P. R.; Elwing, H. Evidence for Different Pharmacological Targets for Imidazoline Compounds Inhibiting Settlement of the Barnacle Balanus Improvisus. *J. Exp. Zool.* **2005**, *303A*, 551-562.

(78) Gohad, N. V.; Dickinson, G. H.; Orihuela, B.; Rittschof, D.; Mount, A. S. Visualization of Putative Ion-Transporting Epithelia in Amphibalanus Amphitrite Using

Correlative Microscopy: Potential Function in Osmoregulation and Biomineralization. *J. Exp. Mar. Biol. Ecol.* **2009**, *380*, 88-98.

(79) Dahlström, M.; Mårtensson, L. G. E.; Jonsson, P. R.; Arnebrant, T.; Elwing, H. Surface Active Adrenoreceptor Compounds Prevent the Settlement of Cyrpid Larvae of Balanus Improvisus. *Biofouling* **2000**, *16*, 191-203.

(80) Powell, K. T.; Cheng, C.; Wooley, K. L. Complex Amphiphilic Hyperbranched Fluoropolymers by Atom Transfer Radical Self-Condensing Vinyl (Co)Polymerization. *Macromolecules* **2007**, *40*, 4509-4515.

(81) Eller, M. J.; Verkhoturov, S. V.; Della-Negra, S.; Rickman, R. D.; Schweikert, E. A. Real-Time Localization of Single C-60 Impacts with Correlated Secondary Ion Detection. *Surf Interface Anal* **2011**, *43*, 484-487.

(82) Mount, A. S.; Wheeler, A. P.; Paradkar, R. P.; Snider, D. Hemocyte-Mediated Shell Mineralization in the Eastern Oyster. *Science* **2004**, *304*, 297-300.

(83) Weibel, D.; Wong, S.; Lockyer, N.; Blenkinsopp, P.; Hill, R.; Vickerman, J. C. A C-60 Primary Ion Beam System for Time of Flight Secondary Ion Mass Spectrometry: Its Development and Secondary Ion Yield Characteristics. *Anal. Chem.* **2003**, *75*, 1754-1764.

(84) Fletcher, J. S.; Conlan, X. A.; Jones, E. A.; Biddulph, G.; Lockyer, N. P.; Vickerman, J. C. Tof-Sims Analysis Using C-60- Effect of Impact Energy on Yield and Damage. *Anal. Chem.* **2006**, *78*, 1827-1831.

(85) Li, Z.; Verkhoturov, S. V.; Schweikert, E. A. Nanovolume Analysis with Secondary Ion Mass Spectrometry Using Massive Projectiles. *Anal. Chem.* **2006**, *78*, 7410-7416.

(86) Chen, L. J.; Shah, S. S.; Silangcruz, J.; Eller, M. J.; Verkhoturov, S. V.; Revzin, A.; Schweikert, E. A. Characterization and Quantification of Nanoparticle-Antibody Conjugates on Cells Using C-60 Tof Sims in the Event-by-Event Bombardment/Detection Mode. *Int. J. Mass Spectrom.* **2011**, *303*, 97-102.

(87) Gohad, N. V.; 2008, Development of a novel fouling deterrence strategy by understanding the effect of noradrenaline on the cells of Eastern Oyster, Crassostrea virginica and cypris larvae of the Striped Barnacle Balanus amphitrite (Doctoral Dissertation), retrieved from ProQuest Dissertations and Theses. (Accession Order No. 3304071).

(88) Lacoste, A.; De Cian, M.-C.; Cueff, A.; Poulet, S. A. Noradrenaline and A-Adrenergic Signaling Induce the Hsp70 Gene Promoter in Mollusc Immune Cells. *J. Cell Sci.* **2001**, *114*, 3557-3564.

(89) Lacoste, A.; Malham, S. K.; Cueff, A.; Jalabert, F.; Gelebart, F.; Poulet, S. A. Evidence for a Form of Adrenergic Response to Stress in the Mollusc Crassostrea Gigas. *J. Exp. Biol.* **2001**, *204*, 1247-1255.

(90) Lacoste, A.; Malham, S. K.; Cueff, A.; Poulet, S. A. Noradrenaline Modulates Oyster Hemocyte Phagocytosis Via a Beta-Adrenergic Receptor– Camp Signaling Pathway. *Gen. Comp. Endocrinol.* **2001**, *122*, 252-259.

(91) Lohse, M. J.; Engelhardt, S.; Eschenhagen, T. What Is the Role of B-Adrenergic Signaling in Heart Failure? *Circ. Res.* **2003**, *93*, 896-906.

(92) Xiao, R.-P. B-Adrenergic Signaling in the Heart: Dual Coupling of the B2-Adrenergic Receptor to Gs and Gi Proteins. *Sci. STKE* **2001**, *104*, re15.

(93) Zhong, J.; Hume, J. R.; Keef, K. D. B-Adrenergic Receptor Stimulation of L-Type Ca2+ Channels in Rabbit Portal Vein Myocytes Involves Both as and by G Protein Subunits. *J. Physiol.* **2001**, *531*, 105-115.

(94) Hori, M.; Sato, H.; Kitakaze, M.; Iwai, K.; Takeda, H.; Inoue, M.; Kamada, T. B-Adrenergic Stimulation Disassembles Microtubules in Neonatal Rat Cultured Cardiomyocytes through Intracellular Ca2' Overload. *Circ. Res.* **1994**, *75*, 324-334.

(95) Pitcher, J. A.; Hall, R. A.; Daaka, Y.; Zhang, J.; Ferguson, S. S. G.; Hester, S.; Miller, S.; Caron, M. G.; Lefkowitz, R. J.; Barak, L. S. The G Protein-Coupled Receptor Kinase 2 Is a Microtubule- Associated Protein Kinase That Phosphorylates Tubulin. *J. Biol. Chem.* **1998**, *273*, 12316-12324.

(96) Gourlay, C. W.; Ayscough, K. R. The Actin Cytoskeleton: A Key Regulator of Apoptosis and Ageing? *Nature Rev. Molecular Cell Biol.* **2005**, *6*, 583-589.

(97) Isoai, A.; Kawahara, H.; Okazaki, Y.-I.; Shizuri, Y. Molecular Cloning of a New Member of the Putative G Protein-Coupled Receptor Gene from Barnacle Balanusamphitrite. *Gene* **1996**, *175*, 95-100.

(98) Dahlström, M.; 2004, Pharmacological agents targeted against barnacles as lead molecules in new antifouling technologies (Doctoral Dissertation), Göteborg University.

(99) Dahms, H.-U.; Qian, P.-E. Adrenoceptor Compounds Prevent the Settlement of Marine Invertebrate Larvae: Balanus Amphitrite (Cirripedia), Bugula Neritina (Bryozoa) and Hydroides Elegans (Polychaeta). *Biofouling* **2004**, *20*, 313-321.

(100) Bielecki, J.; Chan, B. K. K.; Hoeg, J. T.; Sari, A. Antennular Sensory Organs in Cyprids of Balanomorphan Cirripedes: Standardizing Terminology Using Megabalanus Rosa. *Biofouling* **2009**, *25*, 203-214.

(101) Lagersson, N. C.; Garm, A.; Hoeg, J. T. Notes on the Ultrastructure of the Setae on the Fourth Antennulary Segment of the Balanus Amphitrite Cyprid (Crustacea: Cirripedia: Thoracica). *J. Mar. Biol. Ass. U.K.* **2003**, *83*, 361-365.

(102) Maruzzo, D.; Conlan, S.; Aldred, N.; Clare, A. S.; Hoeg, J. T. Video Observation of Surface Exploration in Cyprids of Balanus Amphitrite: The Movements of Antennular Sensory Setae. *Biofouling* **2011**, *27*, 225-239.

(103) Crisp, D. J. Surface Chemistry, a Factor in the Settlement of Marine Invertebrate Larvae. *Botanica Gothburgensia* **1965**, *3*, 51-65.

(104) Crisp, D. J.; Meadows, P. S. Adsorbed Layers: The Stimulus to Settlement in Barnacles. *Proc. R. Soc. Lond. B* **1963**, *158*, 364-387.

(105) Kim, T. D.; Luo, J. D.; Tian, Y. Q.; Ka, J. W.; Tucker, N. M.; Haller, M.; Kang, J. W.; Jen, A. K. Y. Diels-Alder "Click Chemistry" for Highly Efficient Electrooptic Polymers. *Macromolecules* **2006**, *39*, 1676-1680.

(106) Cordier, P.; Tournilhac, F.; Soulie-Ziakovic, C.; Leibler, L. Self-Healing and Thermoreversible Rubber from Supramolecular Assembly. *Nature* **2008**, *451*, 977-980.

(107) White, S. R.; Sottos, N. R.; Geubelle, P. H.; Moore, J. S.; Kessler, M. R.; Sriram, S. R.; Brown, E. N.; Viswanathan, S. Autonomic Healing of Polymer Composites. *Nature* **2001**, *409*, 794-797.

(108) Toohey, K. S.; Hansen, C. J.; Lewis, J. A.; White, S. R.; Sottos, N. R. Delivery of Two-Part Self-Healing Chemistry Via Microvascular Networks. *Adv. Funct. Mater.* **2009**, *19*, 1399-1405.

(109) Chen, X. X.; Dam, M. A.; Ono, K.; Mal, A.; Shen, H. B.; Nutt, S. R.; Sheran, K.; Wudl, F. A Thermally Re-Mendable Cross-Linked Polymeric Material. *Science* **2002**, *295*, 1698-1702.

(110) Kolb, H. C.; Finn, M. G.; Sharpless, K. B. Click Chemistry: Diverse Chemical Function from a Few Good Reactions. *Angew. Chem., Int. Ed.* **2001**, *40*, 2004-2021.

(111) Becer, C. R.; Hoogenboom, R.; Schubert, Ulrich S. Click Chemistry Beyond Metal-Catalyzed Cycloaddition. *Angew. Chem., Int. Ed.* **2009**, *48*, 4900-4908.

(112) Iha, R. K.; Wooley, K. L.; Nystr m , A. M.; Burke, D. J.; Kade, M. J.; Hawker, C. J. Applications of Orthogonal “Click” Chemistries in the Synthesis of Functional Soft Materials. *Chem. Rev.* **2009**, *109*, 5620-5686.

(113) Lutz, J.-F. 1,3-Dipolar Cycloadditions of Azides and Alkynes: A Universal Ligation Tool in Polymer and Materials Science. *Angew. Chem., Int. Ed.* **2007**, *46*, 1018-1025.

(114) Binder, W. H.; Sachsenhofer, R. „Click" Chemistry in Polymer and Materials Science. *Macromol. Rapic. Commun.* **2007**, *28*, 15-54.

(115) Killops, K. L.; Campos, L. M.; Hawker, C. J. Robust, Efficient, and Orthogonal Synthesis of Dendrimers Via Thiol-Ene "Click" Chemistry. *J. Am. Chem. Soc.* **2008**, *130*, 5062-5064.

(116) Kade, M. J.; Burke, D. J.; Hawker, C. J. The Power of Thiol-Ene Chemistry. *J. Polym. Sci., Part A: Polym. Chem.* **2010**, *48*, 743-750.

(117) Hoyle, C. E.; Lee, T. Y.; Roper, T. Thiol-Enes: Chemistry of the Past with Promise for the Future. *J. Polym. Sci., Part A: Polym. Chem.* **2004**, *42*, 5301-5338.

(118) Mather, B. D.; Viswanathan, K.; Miller, K. M.; Long, T. E. Michael Addition Reactions in Macromolecular Design for Emerging Technologies. *Prog. Polym. Sci.* **2006**, *31*, 487-531.

(119) Becer, C. R.; Babiuch, K.; Pilz, D.; Hornig, S.; Heinze, T.; Gottschaldt, M.; Schubert, U. S. Clicking Pentafluorostyrene Copolymers: Synthesis, Nanoprecipitation, and Glycosylation. *Macromolecules* **2009**, *42*, 2387-2394.

(120) Joralemon, M. J.; O'Reilly, R. K.; Matson, J. B.; Nugent, A. K.; Hawker, C. J.; Wooley, K. L. Dendrimers Clicked Together Divergently. *Macromolecules* **2005**, *38*, 5436-5443.

(121) McElhanon, J. R.; Wheeler, D. R. Thermally Responsive Dendrons and Dendrimers Based on Reversible Furan-Maleimide Diels−Alder Adducts. *Org. Lett.* **2001**, *3*, 2681-2683.

(122) Polaske, N. W.; McGrath, D. V.; McElhanon, J. R. Thermally Reversible Dendronized Step-Polymers Based on Sequential Huisgen 1,3-Dipolar Cycloaddition and Diels−Alder "Click" Reactions. *Macromolecules* **2010**, *43*, 1270-1276.

(123) Kose, M. M.; Yesilbag, G.; Sanyal, A. Segment Block Dendrimers Via Diels−Alder Cycloaddition. *Org. Lett.* **2008**, *10*, 2353-2356.

(124) Syrett, J. A.; Mantovani, G.; Barton, W. R. S.; Price, D.; Haddleton, D. M. Self-Healing Polymers Prepared Via Living Radical Polymerization. *Polym. Chem.* **2010**, *1*, 102-106.

(125) Li, M.; De, P.; Gondi, S. R.; Sumerlin, B. S. End Group Transformations of Raft-Generated Polymers with Bismaleimides: Functional Telechelics and Modular Block Copolymers. *J. Polym. Sci., Part A: Polym. Chem.* **2008**, *46*, 5093-5100.

(126) Durmaz, H.; Colakoglu, B.; Tunca, U.; Hizal, G. Preparation of Block Copolymers Via Diels Alder Reaction of Maleimide- and Anthracene-End Functionalized Polymers. *J. Polym. Sci., Part A: Polym. Chem.* **2006**, *44*, 1667-1675.

(127) Kuramoto, N.; Hayashi, K.; Nagai, K. *J. Polym. Sci., Part A: Polym. Chem.* **1994**, *32*, 2501-2504.

(128) Gandini, A.; Coelho, D.; Silvestre, A. J. D. Reversible Click Chemistry at the Service of Macromolecular Materials. Part 1: Kinetics of the Diels-Alder Reaction

Applied to Furan-Maleimide Model Compounds and Linear Polymerizations. *Eur. Polym. J.* **2008**, *44*, 4029-4036.

(129) Gousse, C.; Gandini, A. *Polym. Inter.* **1999**, *48*, 723-731.

(130) Durmaz, H.; Dag, A.; Altintas, O.; Erdogan, T.; Hizal, G.; Tunca, U. One-Pot Synthesis of Abc Type Triblock Copolymers Via in Situ Click [3 + 2] and Diels−Alder [4 + 2] Reactions. *Macromolecules* **2006**, *40*, 191-198.

(131) Gacal, B.; Durmaz, H.; Tasdelen, M. A.; Hizal, G.; Tunca, U.; Yagci, Y.; Demirel, A. L. Anthracene−Maleimide-Based Diels−Alder "Click Chemistry" as a Novel Route to Graft Copolymers. *Macromolecules* **2006**, *39*, 5330-5336.

(132) Bousquet, A.; Barner-Kowollik, C.; Stenzel, M. H. Synthesis of Comb Polymers Via Grafting-onto Macromolecules Bearing Pendant Diene Groups Via the Hetero-Diels-Alder-Raft Click Concept. *J. Polym. Sci., Part A: Polym. Chem.* **2010**, *48*, 1773-1781.

(133) Vieyres, A.; Lam, T.; Gillet, R.; Franc, G.; Castonguay, A.; Kakkar, A. Combined Cui-Catalysed Alkyne-Azide Cycloaddition and Furan-Maleimide Diels-Alder "Click" Chemistry Approach to Thermoresponsive Dendrimers. *Chem. Commun.* **2010**, *46*, 1875-1877.

(134) Durmaz, H.; Karatas, F.; Tunca, U.; Hizal, G. Preparation of Abc Miktoarm Star Terpolymer Containing Poly(Ethylene Glycol), Polystyrene, and Poly(<I>Tert</I>-Butylacrylate) Arms by Combining Diels-Alder Reaction, Atom Transfer Radical, and Stable Free Radical Polymerization Routes. *J. Polym. Sci., Part A: Polym. Chem.* **2006**, *44*, 499-509.

(135) Shi, Z.; Hau, S.; Luo, J.; Kim, T.-D.; Tucker, N. M.; Ka, J.-W.; Sun, H.; Pyajt, A.; Dalton, L.; Chen, A.; Jen, A. K.-Y. Highly Efficient Diels–Alder Crosslinkable Electro-Optic Dendrimers for Electric-Field Sensors. *Adv. Funct. Mater.* **2007**, *17*, 2557-2563.

(136) Inglis, A. J.; Nebhani, L.; Altintas, O.; Schmidt, F. G.; Barner-Kowollik, C. Rapid Bonding/Debonding on Demand: Reversibly Cross-Linked Functional Polymers Via Diels−Alder Chemistry. *Macromolecules* **2010**, *43*, 5515-5520.

(137) Swanson, J. P.; Rozvadovsky, S.; Seppala, J. E.; Mackay, M. E.; Jensen, R. E.; Costanzo, P. J. Development of Polymeric Phase Change Materials on the Basis of Diels−Alder Chemistry. *Macromolecules* **2010**, *43*, 6135-6141.

(138) Gandini, A.; Silvestre, A. J. D.; Coelho, D. Reversible Click Chemistry at the Service of Macromolecular Materials. 2. Thermoreversible Polymers Based on the Diels-Alder Reaction of an a-B Furan/Maleimide Monomer. *J. Polym. Sci., Part A: Polym. Chem.* **2010**, *48*, 2053-2056.

(139) Canadell, J.; Fischer, H.; De With, G.; van Benthem, R. A. T. M. Stereoisomeric Effects in Thermo-Remendable Polymer Networks Based on Diels–Alder Crosslink Reactions. *J. Polym. Sci., Part A: Polym. Chem.* **2010**, *48*, 3456-3467.

(140) Adzima, B. J.; Aguirre, H. A.; Kloxin, C. J.; Scott, T. F.; Bowman, C. N. Rheological and Chemical Analysis of Reverse Gelation in a Covalently Cross-Linked Diels−Alder Polymer Network. *Macromolecules* **2008**, *41*, 9112-9117.

(141) Hizal, G.; Tunca, U.; Sanyal, A. Discrete Macromolecular Constructs Via the Diels–Alder "Click" Reaction. *J. Polym. Sci., Part A: Polym. Chem.* **2011**, *49*, 4103-4120.

(142) Morgan, C. R.; Ketley, A. D. The Effect of Phosphines on Thiol/Ene Curing Systems. *J. Polym. Sci., Polym. Lett. Ed.* **1978**, *16*, 75-79.

(143) Morgan, C. R.; Magnotta, F.; Ketley, A. D. Thiol/Ene Photocurable Polymers. *Polym. Chem.* **1977**, *15*, 627-645.

(144) Cakmakci, E.; Mulazim, Y.; Kahraman, M. V.; Apohan, N. K. Flame Retardant Thiol–Ene Photocured Coatings. *React. Funct. Polym.* **2011**, *71*, 36-41.

(145) Campos, L. M.; Meinel, I.; Guino, R. G.; Schierhorn, M.; Gupta, N.; Stucky, G. D.; Hawker, C. J. Highly Versatile and Robust Materials for Soft Imprint Lithography Based on Thiol-Ene Click Chemistry. *Adv. Mater.* **2008**, *20*, 3728-3733.

(146) Hagberg, E. C.; Malkoch, M.; Ling, Y. B.; Hawker, C. J.; Carter, K. R. Effects of Modulus and Surface Chemistry of Thiol-Ene Photopolymers in Nanoimprinting. *Nano Lett.* **2007**, *7*, 233-237.

(147) O'Brien, A. K.; Cramer, N. B.; Bowman, C. N. Oxygen Inhibition in Thiol-Acrylate Photopolymerizations. *J. Polym. Sci., Part A: Polym. Chem.* **2006**, *44*, 2007-2014.

(148) Cramer, N. B.; Scott, J. P.; Bowman, C. N. Photopolymerizations of Thiol-Ene Polymers without Photoinitiators. *Macromolecules* **2002**, *35*, 5361-5365.

(149) Ihre, H.; Johansson, M.; Malström, E.; Hult, A. *Dendrimers and Hyperbranched Aliphatic Polyesters Based on 2,2-Bis(Hydroxymethyl)Propionic Acid (Bis-Mpa)*; JAI Press Inc., 1996; Vol. 3.

(150) Mespouille, L.; Hedrick, J. L.; Dubois, P. Expanding the Role of Chemistry to Produce New Amphiphilic Polymer (Co)Networks. *Soft Matter* **2009**, *5*, 4878-4892.

(151) Imbesi, P. M.; Fidge, C.; Raymond, J. E.; Cauet, S. I.; Wooley, K. L. Model Diels-Alder Studies for the Creation of Amphiphilic Cross-Linked Networks as Healable, Antibiofouling Coatings. *ACS Macro Lett.* **2012**, *1*, 473-477.

(152) Tan, J.-C.; Saines, P. J.; Bithell, E. G.; Cheetham, A. K. Hybrid Nanosheets of an Inorganic Organic Framework Material: Facile Synthesis, Structure, and Elastic Properties. *ACS Nano* **2012**, *6*, 615-621.

(153) Young, T. J.; Monclus, M. A.; Burnett, T. L.; Broughton, W. R.; Ogin, S. L. The Use of the Peakforce™ Quantitative Nanomechanical Mapping Afm-Based Method for High-Resolution Young's Modulus Measurement of Polymers. *Meas. Sci. Technol.* **2011**, *22*, 125703-125708.

VITA

Name: Philip Matthew Imbesi

Address: Department of Chemistry
Texas A&M University
Mailstop 3255
Ross St. @ Spence St.
College Station, TX 77842

Email Address: pimbesi84@gmail.com

Education: B.S., Biomedical Engineering – Polymer Biomaterials, Case Western Reserve University, 2007

B.A., Chemistry, Minor, Mathematics, Case Western Reserve University, 2007

M.A., Chemistry, Washington University in St. Louis, 2009